Short-term Structural Performance of Self-monitoring Composite Marine Propellers

Zhang, X.

Citation (APA)
Zhang, X. (2021). *Short-term Structural Performance of Self-monitoring Composite Marine Propellers*. [Dissertation (TU Delft), Delft University of Technology]. https://doi.org/10.4233/uuid:479b71c1-a006-4d9a-abda-b000a7711899

Important note
To cite this publication, please use the final published version (if applicable).
Please check the document version above.

Short-term Structural Performance of
Self-monitoring Composite Marine Propellers

Dissertation

for the purpose of obtaining the degree of doctor
at Delft University of Technology
by the authority of the Rector Magnificus prof.dr.ir. T.H.J.J. van der Hagen
chair of the Board for Doctorates
to be defended publicly on
Wednesday 17 November 2021 at 10:00 o'clock

by

Xiaobo ZHANG

Master of Science in Mechanical Engineering
Kungliga Tekniska högskolan, Sweden
born in Hejin, Shanxi, China

This dissertation has been approved by the promotors.

Composition of the doctoral committee:

Rector Magnificus	chairperson
Prof.em.dr.ir. M.L. Kaminski	Delft University of Technology, promotor
Dr. L. Pahlavan	Delft University of Technology, copromotor

Independent members:

Prof.ir. J.J. Hopman	Delft University of Technology
Prof.dr.ir. T. van Terwisga	Delft University of Technology
Prof.dr.ir. W. De Waele	Ghent University, Belgium
Dr. C.M. Rizzo	University of Genoa, Italy

Other member:

Prof.dr. C. Kassapoglou	Delft University of Technology

士不可以不弘毅，任重而道远。

An educated gentleman cannot but be resolute and broad-minded,

for he has taken up a heavy responsibility and a long course.

Contents

SUMMARY

As a primary component of the marine propulsion systems, ship propellers have been traditionally made of nickel-aluminium-bronze (NAB) or manganese bronze (MB). With the development of fibre reinforced composite materials, the advanced plastic materials are considered to be applied in the manufacturing of marine propellers. Compared to conventional rigid propellers, the composite marine propellers are expected to possess advantages of lighter weight, lower maintenance costs, higher cavitation inception speed, declined acoustic signature, and improved efficiency at off-design conditions. These potential benefits have promoted numerical and (fewer) experimental investigations of composite marine propellers. This supports the promising future of their applications, however, a more profound understanding of the underlying mechanical properties of composite marine propellers is essential before they find a wider use in practical applications in engineering.

Part 1:

One crucial topic concerns the fatigue performance of composite marine propellers operating in harsh seawater environments. As a case study, the Nautilus diving support vessel is considered in this research. It sails in a straight path in the calm water at the constant speed of 10.4 knots, with a four-blade composite propeller rotating at the constant speed of 600 rpm. The propeller experiences a non-uniform wakefield. In the first part of this research, the fatigue characteristics of such a composite propeller have been investigated. The propeller blade has a sandwich structure, where the blade faces at both the pressure and suction sides are made of carbon fibre reinforced composite laminates. The blade core is made of polymat/resin rich material. In view of symmetry, a 3D solid finite element (FE) model of one blade was created. A full revolution of the propeller was evenly divided into 60 time steps. Corresponding to each time step, the fluid pressure at the specific position has been computed and transformed to nodal forces, which were applied to the surfaces of the blade model. Regarding each load case, the output of FE analysis provided the distribution of Tsai-Wu failure index at each ply of the carbon fibre reinforced plastic (CFRP) laminates. According to the statistical analysis of the attributes, i.e., belonging to an element, of the four largest maximum failure indices at each load case, the hot-spot elements were identified. Moreover, one most critical hot-spot element was then recognised by comparing the critical stress and moments resultants of all hot-spots.

The experimental investigation has focused on the short-term fatigue performance of the one most critical hot-spot. The composite specimens and fatigue cyclic loading were designed according to the lay-up configuration and loading conditions of the most critical hot-spot element. A CFRP laminate was made by hand lay-up method, and cut into 36 specimens. The specimens quality was studied experimentally before performing the tests, based on which, the stiffness properties of the UD CFRP

lamina were updated. A half of the total 36 (dry) specimens were exposed to fatigue tests, using the specified fatigue cyclic loading. The other 18 (wet) specimens were submerged in 5% salt water, and the mass of each specimen was recorded at certain intervals. The specimens reached the saturation state after 60 days. The (residual) tensile stiffness and strength properties of all specimens (both dry and wet, intact and undergoing 10^4 and 10^6 cycles of fatigue loads) were acquired from the tests. The ultimate tensile strength of dry specimens did not show an apparent decreasing trend with increasing number of fatigue load cycles. Because the tensile strength is mainly determined by fibres, it suggests that the designed fatigue loads had marginal damaging effect on the carbon fibres. The observed tensile failure modes included fibre rupture, matrix cracking and fibre-matrix-adhesion. Furthermore, the mean tensile stiffness of dry specimens decreased by 17% after applying 10^4 cycles of fatigue loads, and maintained at that level until the fatigue load cycles reached 10^6. As for the wet specimens, the ultimate tensile strength was also not affected by the fatigue loads, and the same failure modes were observed as in the failed dry specimens. Because of the small difference between the (residual) strength of dry and wet specimens, it was concluded that the aging procedure had little effect on the carbon fibres. The mean stiffness of wet specimens did not decline after applying 10^4 cycles of fatigue loads, but decreased by 7% when the fatigue load cycles increased to 10^6. In the experiment, the maximum number of fatigue load cycles is much lower than the number of fatigue load cycles in a propeller during its lifetime. Nevertheless, this research has attempted to provide initial insights into the degradation of mechanical properties of composite marine propeller.

Part 2:

The intrinsic layered structure of the composite laminate has inspired the concept of self-monitoring composite marine propeller, in which the sensors are embedded. The piezoelectric (PZT) sensor, for example, can be used in the measurements over a wide range of frequencies. It is insusceptible to environments during manufacturing and embedding procedures. However, the current understanding about the effect of embedded sensors on the structural response is still limited. This effect is determined by numerous factors, e.g., the way of embedding sensor (embedded in between two neighbouring plies, or in a cut-out inside the laminate), the associated insulation materials (shielding the sensor from electrically conductive surroundings), the defects introduced during handling, etc. Therefore, the effects of embedded sensors on the flexural stiffness and strength properties of CFRP specimens have been investigated in the second part of this research. The composite specimens with embedded small sensors at tension and compression sides, with embedded large sensor at compression side, and without embedded sensor (i.e., pristine laminate) were subjected to four-point bending up to failure. For each type of the specimen, a progressive failure analysis (PFA) was performed using 3D solid FE model. The PFA results were compared to the corresponding experimental records to identify the flexural stiffness degradation and ultimate failure mechanisms. It is concluded that the fibre tensile failure has exhibited a dominant role in the loss of flexural stiffness. In the experiments it was also observed that delaminations have dominated the ultimate bending failure. The defects and micro cracks, introduced during embedding a sensor into the composite specimen, propagated quickly before the end of loading procedure. They developed into delamination failure and destroyed specimen integrity. The effects of insulation materials (woven GFRP fabric and neat resin) on the structural stiffness have been

investigated as well. Due to the relatively limited use of insulation materials, this has been observed to have a negligible effect.

SAMENVATTING

Als primair onderdeel van het scheepsvoortstuwingssysteem wordt een scheepsschroef traditioneel gemaakt uit nikkel-aluminium-brons (NAB) of mangaan-brons (MB). Door de ontwikkeling van vezel-versterkte composieten worden geavanceerde kunststoffen overwogen voor toepassing in de productie van scheepsschroeven. Vergeleken met conventionele rigide schroeven lijken de voordelen van composieten scheepsschroeven te zijn dat ze lichter zijn, lagere onderhoudskosten hebben, hogere snelheden kunnen verdragen zonder dat cavitatie-inceptie plaatsvindt, een verlaagde akoestische signatuur hebben en bovenal een verhoogde efficiëntie in omstandigheden die buiten het initiele ontwerp-optimum vallen. Deze potentiële voordelen zijn de drijfveer geweest achter numerieke en (minder vaak) experimentele studies over composieten scheepsschroeven. De resultaten hiervan ondersteunen een veelbelovende toekomst voor de toepassing van composieten scheepschroeven. Echter, voordat composieten breder in de praktijk gebracht kunnen worden, is groter begrip van onderliggende mechanische eigenschappen van de schroeven vereist.

Deel 1:

Één cruciaal onderwerp betreft de vermoeiingseigenschappen van composieten scheepsschroeven in ruw zeewater. Het duikvaartuig Nautilus is in dit onderzoek gebruikt als case study. Het schip vaart rechtdoor in kalm water met een constante snelheid van 10.4 knopen en is uitgerust met een composieten schroef. Deze schroef draait met een constante rotatiesnelheid van 600 RPM in een niet-uniform instroomveld. In het eerste deel van dit onderzoek zijn de vermoeiingseigenschappen van een dergelijke composieten schroef onderzocht. Het schroefblad heeft een gelaagde structuur, waar het blad aan de druk- en zuigzijde gemaakt is van een koolstofvezel-versterkte, composieten laminaat. De kern van het blad is gemaakt van polymat/hars-rijk materiaal. Gebruikmakend van symmetrie is een 3D volumetrische eindige elementen (EE) model van één blad gegenereerd. Een volledige omwenteling van de schroef is gelijkmatig verdeeld in 60 tijdsstappen. In elke tijdsstap is de vloeistofdruk op specifieke punten berekend en getransformeerd naar knooppuntskrachten. Deze krachten zijn vervolgens aangebracht op het oppervlak van het bladmodel. Voor iedere tijdstap wordt de uitvoer van de EE-analyse gebruikt voor het berekenen van de Tsai-Wu faalindex in elke laag van de koolstofvezel-versterkte kunstof (CFRP) laminaten. Volgens statistische analyse van de kenmerken van de vier grootste kritische maximale faalindices, behorende bij een element, in elke tijdstap zijn vervolgens hot-spot elementen geïdentificeerd. Daarbij is één meest-kritisch hot-spot element geselecteerd door het vergelijken van de kritische spanningen en de resulterende momenten van alle hot-spots.

Het experimentele onderzoek is gefocust op de korte-termijnvermoeiingseigenschappen van de meest kritische hot-spot. Composieten proefstukken en de cyclische vermoeiingsbelasting zijn

ontworpen volgens de configuratie van het laminaat en de belastingcondities van het meest kritische hot-spot element. Een CFRP-laminaat is handmatig gefabriceerd en opgedeeld in 36 proefstukken. De kwaliteit van de proefstukken is experimenteel onderzocht voordat de vermoeiingstesten zijn uitgevoerd. Gebaseerd op dit onderzoek zijn de stijfheidseigenschappen van het eenrichtings (UD) CFRP-laminaat bijgewerkt. De helft van de in totaal 36 (droge) proefstukken zijn direct gebruikt voor vermoeiingstesten, gebruikmakend van de eerder gespecificeerde cyclische vermoeiingsbelasting. De andere 18 (natte) proefstukken werden ondergedompeld in 5% zout water en de massa van deze proefstukken werd periodiek vastgelegd. De proefstukken waren verzadigd na 60 dagen. De (rest-)trekstijfheid en de sterkte-eigenschappen van alle proefstukken (nat en droog, intact en na 10^4 en 10^6 vermoeiingscylci) zijn hierna met uniaxiale statische trektesten verkregen. De ultieme sterkte van de droge proefstukken liet geen duidelijke daling zien vergeleken met toenemende vermoeiingscycli. Omdat de treksterkte met name bepaald wordt door de vezels, laat dit zien dat de ontwerp-vermoeiingsbelasting een marginaal effect had op de beschadiging van de koolstofvezels. De waargenomen faalmodes voor de vezels onder trek waren onder andere de breuk van vezels, scheuren in de matrix en falen in desintegratie' van vessel-matrix-adhesie. Bovendien laat de equivalente (rest-)stijfheid van de droge proefstukken zien dat de gemiddelde trekstijfheid afneemt met 17% na 10^4 cycli, en dat dit niveau aanhoudt tot 10^6 vermoeiingscycli. Wat betreft de natte proefstukken was de ultieme treksterkte niet beïnvloed door de vermoeiing en dezelfde faalmodes zijn gevonden als in de droge proefstukken. Vanwege het kleine verschil tussen de (rest-)sterkte van de natte en droge proefstukken kan er geconcludeerd worden dat het verjaringseffect maar een beperkt effect heeft op de koolstofvezels. De gemiddelde stijfheid van de natte proefstukken nam niet af na 10^4 cycli, maar nam 7% af bij een toename tot 10^6 vermoeiingscycli. Het maximum aantal cycli in het vermoeiingsexperiment is veel lager dan het aantal rotaties van een schroef gedurende zijn levensduur. Desalniettemin zou dit onderzoek eerste inzichten in de degradatie van de mechanische eigenschappen van composieten schroeven moeten geven.

Deel 2:

De intrinsiek gelaagde structuur van het composieten laminaat is de inspiratie achter het concept van zelf-monitorende composieten scheepsschroeven, waarin sensors verwerkt zijn. De piëzo-elektrische sensor, bijvoorbeeld, kan gebruikt worden in metingen over een brede band van frequenties. Wanneer piëzo-elektrische sensors ingebed worden, zijn deze beschermd tegen degradatie van buitenaf. Ook verandert hiermee de externe geometrie van het propellerblad niet. Echter, de huidige kennis over het effect van ingebedde sensoren op de constructieve response is beperkt. Dit effect wordt bepaald door verschillende factoren, bijvoorbeeld; de manier waarop de sensors ingebed zijn (inbedding tussen lagen of een uitsnede in het laminaat), de bijbehorende isolatiematerialen (afscherming van de sensor van de elektrisch geleidende omgeving) en de defecten die geïntroduceerd worden tijdens gebruik. Daarom zijn in het tweede deel van dit onderzoek de effecten van ingebedde sensoren op de buigstijfheid- en sterkte-eigenschappen van CFRP proefstukken onderzocht. De composieten proefstukken met kleine ingebedde sensoren aan trek- en compressiezijde, met grote ingelegde sensoren aan de compressiezijde en zonder ingelegde sensor (een zuiver laminaat), zijn belast in vierpuntsbuigtoestand totdat de proefstukken faalden. Voor elk type proefstuk is een toenemende faalanalyse (PFA) gemaakt met een 3D volumetrisch eindige elementenmodel. De PFA resultaten zijn vergeleken met de bijbehorende

experimentele resultaten om de degradatie in buigstijfheid en ultieme sterkte-mechanismen te identificeren. De conclusie is dat het falen van een vezel onder trek een dominante speelt in het verlies van buigstijfheid. Ook delaminatie domineert in de ultieme buigsterkte, wat blijkt uit experimentele observaties. De defecten en microscheuren die tijdens het inbedden van een sensor in een proefstuk ontstaan zijn, ontwikkelden snel voor het einde van de belastingprocedure. Deze defecten en scheuren zorgden voor falen door delaminatie en schaadden hiermee de integriteit van het proefstuk. De effecten van isolatiematerialen (geweven Glasvezelcomposiet (GFRP) en zuiver kunsthars) op de constructiestijfheid is ook onderzocht, maar vanwege het relatief weinige gebruik van deze materialen lijken de effecten hiervan beperkt te zijn.

1

Introduction

1.1. MOTIVATION

During the past decades, the fibre reinforced plastic materials have been increasingly considered for manufacturing marine propellers (Fig. 1.1). The composite marine propellers can overweigh the traditional ones, which are generally made of nickel-aluminium-bronze (NAB) or manganese bronze (MB), in terms of lightening weight, lowering maintenance costs [1], improving cavitation inception speed [2-4], dismissing acoustic signature [5], and particularly enhancing efficiency at off-design conditions [6].

Fig. 1.1: Composite propeller used in test (Photo: MARIN).

These potential advantages have promoted research on the composite marine propeller. For example, the fluid-structure interaction (FSI) response of flexible composite propellers has been studied substantially, and are summarised in [7, 8]. They have been used together with genetic algorithms to maximise the efficiency gain at off-design conditions [6, 9-13]. Some other optimisation works concerned detaining cavitation [2-4] and improving vibration performance [5]. The experimental studies are important to validate the claimed advantages, though they have been mostly limited to small dimension propellers so far [4, 13, 14], and the setups of flows are simplified in experiments [16, 17]. Another important challenge encountered in experiments is the accuracy of different measuring techniques, which are designed for the rotating propellers submerged under water [16, 18, 19]. Although previous research has revealed the promising features of composite marine propellers, more thorough understandings on the mechanical properties of composite marine propellers are required [7, 8], e.g., in relation to the fatigue performance in aggressive seawater environment.

On the other hand, the characteristics of fibre reinforced plastic (FRP) materials aged in different types of fluids have been investigated [20-37]. In these studies, aging composite materials have been processed in different fluids, including seawater [20-24], substitute/artificial/synthetic seawater [25-32], purified water [31], deionised water [32], and distilled water [33, 34]. Immersing in fluids, the water molecules diffuse into the FRP materials. It is well acknowledged that the matrix plays a main role in absorbing water, and the voids and poorly bonded fibre/matrix interfaces are supplements to the main water diffusion pathway. The procedure of water uptaking can be influenced by several parameters, e.g.,

the fluid temperature [21], aging time [22, 24, 25], fibre type [35-37], fibre structure [22], matrix type [29], and manufacturing method, etc. The detrimental effects of aging procedure on the quasi-static tensile [20, 21, 28, 29, 31-34], flexural [20, 24, 26-29, 30, 32] and interlaminar shear [20, 21, 26] properties of composite materials have been investigated in experiments. A few publications discussed the effect on the tensile-tensile fatigue performance [20, 31, 34] and flexural fatigue performance [20, 23, 26, 27, 30]. These studies can provide references for analysing the fatigue behaviour of composite propeller. In spite of the pioneering works, however, the effect of water absorption on the mechanical properties of advanced composite materials, especially in practical engineering applications, is beyond the current understanding.

The built-in layered structure of composite laminates creates an inspiring vision of self-monitoring composite marine propellers using embedded sensors [38-40]. The piezoelectric (PZT) sensor, for example, has potentials to be used in a wide range of measurements, including dynamic pressure, acceleration, ultrasonic waves, and possible simultaneous combinations [41]. The PZT sensor is insusceptible to environments during manufacturing and embedding procedures [42]. It can be embedded either in between two neighbouring plies [41-50], or in a cut-out inside the laminate [40, 44, 45, 51]. Considering some composite materials are of electrically conductive, the insulation materials are required to shield the sensors from surroundings [38, 44-46, 48, 52-55]. In the meantime, the embedded sensors, wires (connected to outer data management systems) and possible insulation covers could affect the mechanical properties of the base materials. Therefore, depending on the choice of insulation materials and embedding setups, the global stiffness and strength would be influenced to different extents.

1.2. RESEARCH OBJECTIVE

One first objective of this research is to investigate the short-term fatigue performance of composite marine propeller. The study focuses on a CFRP propeller subjected to specific non-uniform wakefield. Besides, regarding to the concept of future self-monitoring composite propellers, this research aims to analyse the stiffness degradation mechanism and final failure mechanism of CFRP specimens with embedded PZT sensors which subjected to four-point bending.

1.3. THESIS OUTLINE

This dissertation consists of five chapters. Chapter 1 provided a concise description of the background, motivation, and objectives of this thesis. The finite element model of the CFRP marine propeller blade is elaborated in Chapter 2. In view of Tsai-Wu failure index, the numerical analysis identifies hot-spot elements in the considered blade model. The most critical hot-spot is determined by comparing critical stress and moment resultants of all hot-spots, the stacking sequence and stress states of which are employed in designing specimen and fatigue cyclic loading in Chapter 3. Moreover, this chapter consists of specimens manufacturing and composite quality evaluation. The non-aged (dry) and aged (wet) specimens are subjected to fatigue tests. After applying fatigue loads up to 10^4 and 10^6 cycles, the decline of ultimate tensile strength and tensile stiffness of both dry and wet specimens are investigated

experimentally, based on which the effects of fatigue cyclic loading and water uptaking on the mechanical properties of the critical hot-spot are illustrated. Chapter 4 focuses on the influence of embedded PZT sensor on the mechanical properties of CFRP laminates. A progressive failure analysis is performed with the finite element models of CFRP laminate without sensor, with small and large sensor. The outputs of load-displacement relation are compared with corresponding four-point bending test records. The mechanisms that dominate flexural stiffness degradation and ultimate failure are recognised. In addition, the effects of insulation materials on the global bending stiffness are studied. Finally, the overall conclusions are presented in Chapter 5, which also precede the recommendations for future work.

REFERENCES

[1] Kane, C. and Smith, J., 2003. Composite blades in marine propulsors. In *Proceedings of International Conference on Advanced Marine Materials: Technologies and Applications*.

[2] International Towing Tank Conference Resistance Committee, 2005. Final report and recommendations to the 24th ITTC. In *Proceedings of 24th international towing tank conference, Edinburgh, UK, 2005*.

[3] Solomon Raj, S. and Reddy, R., 2014. P. Bend-twist coupling and its effect on cavitation inception of composite marine propeller. *Int. J. Mech. Eng. Technol*, *5*, pp.306-314.

[4] CHEN, B., 2006. Design, fabrication and testing of pitch-adapting (flexible) composite propellers. In *Propellers/Shafting 2006 Symposium* (Vol. 8). SNAME.

[5] He, X.D., Hong, Y. and Wang, R.G., 2012. Hydroelastic optimisation of a composite marine propeller in a non-uniform wake. *Ocean engineering*, *39*, pp.14-23.

[6] Liu, Z. and Young, Y.L., 2009. Utilization of bend–twist coupling for performance enhancement of composite marine propellers. *Journal of Fluids and Structures*, *25*(6), pp.1102-1116.

[7] Young, Y.L., Motley, M.R., Barber, R., Chae, E.J. and Garg, N., 2016. Adaptive composite marine propulsors and turbines: progress and challenges. *Applied Mechanics Reviews*, *68*(6).

[8] Maljaars, P.J. and Kaminski, M.L., 2015. Hydro-elastic analysis of flexible propellers: an overview. In *Fourth International Symposium on Marine Propulsors*.

[9] Plucinski, M.M., Young, Y.L. and Liu, Z., 2007, July. Optimization of a self-twisting composite marine propeller using Genetic algorithms. In *16th International conference on composite materials, Kyoto, Japan* (pp. 8-13).

[10] Lin, C.C., Lee, Y.J. and Hung, C.S., 2009. Optimization and experiment of composite marine propellers. *Composite structures*, *89*(2), pp.206-215.

[11] Blasques, J.P., Berggreen, C. and Andersen, P., 2010. Hydro-elastic analysis and optimization of a composite marine propeller. *Marine Structures*, *23*(1), pp.22-38.

[12] Lee, Y.J. and Lin, C.C., 2004. Optimized design of composite propeller. *Mechanics of advanced materials and structures*, *11*(1), pp.17-30.

[13] Mulcahy, N.L., Prusty, B.G. and Gardiner, C.P., 2010. Hydroelastic tailoring of flexible composite propellers. *Ships and Offshore structures*, *5*(4), pp.359-370.

[14] Maljaars, P.J., Kaminski, M.L. and Den Besten, J.H., 2017. Finite element modelling and model updating of small scale composite propellers. *Composite Structures*, *176*, pp.154-163.

[15] Maljaars, P., Bronswijk, L., Windt, J., Grasso, N. and Kaminski, M., 2018. Experimental validation of fluid–structure interaction computations of flexible composite propellers in open water conditions using BEM-FEM and RANS-FEM methods. *Journal of Marine Science and Engineering*, *6*(2), p.51.

[16] Young, Y.L., 2008. Fluid–structure interaction analysis of flexible composite marine propellers. *Journal of fluids and structures*, *24*(6), pp.799-818.

[17] Taketani, T., Kimura, K., Ando, S. and Yamamoto, K., 2013, May. Study on performance of a ship propeller using a composite material. In *The Third International Symposium on Marine Propulsors smp* (Vol. 13).

[18] Maljaars, P.J. and Dekker, J.A., 2014. Hydro-elastic analysis of flexible marine propellers. In *Maritime Technology and Engineering-Edited by Guedes Soares and Santos*, pp.705-715.

[19] Maljaars, P., Grasso, N., Kaminski, M. and Lafeber, W., 2017, June. Validation of a steady BEM-FEM coupled simulation with experiments on flexible small scale propellers. In *Proceedings of the Fifth International Symposium on Marine Propulsors, Espoo, Finland* (pp. 12-15).

[20] Guen-Geffroy, L., Le Gac, P.Y., Diakhate, M., Habert, B. and Davies, P., 2018, January. Long-term durability of CFRP under fatigue loading for marine applications. In *MATEC web of conferences* (Vol. 165). EDP Sciences.

[21] Tual, N., Carrere, N., Davies, P., Bonnemains, T. and Lolive, E., 2015. Characterization of sea water ageing effects on mechanical properties of carbon/epoxy composites for tidal turbine blades. *Composites Part A: Applied Science and Manufacturing*, *78*, pp.380-389.

[22] Boisseau, A., Davies, P. and Thiebaud, F., 2012. Sea water ageing of composites for ocean energy conversion systems: influence of glass fibre type on static behaviour. *Applied Composite Materials*, *19*(3-4), pp.459-473.

[23] Boisseau, A., Davies, P. and Thiebaud, F., 2013. Fatigue behaviour of glass fibre reinforced composites for ocean energy conversion systems. *Applied Composite Materials*, *20*(2), pp.145-155.

[24] Visco, A.M., Calabrese, L. and Cianciafara, P., 2008. Modification of polyester resin based composites induced by seawater absorption. *Composites part A: applied science and manufacturing*, *39*(5), pp.805-814.

[25] Cavasin, M., Sangermano, M., Thomson, B. and Giannis, S., 2019. Exposure of glass fiber reinforced polymer composites in seawater and the effect on their physical performance. *Materials*, *12*(5), p.807.

[26] Boisseau, A. and Peyrac, C., 2015. Long term durability of composites in marine environment: comparative study of fatigue behavior. *Procedia Engineering*, *133*, pp.535-544.

[27] Poodts, E., Minak, G. and Zucchelli, A., 2013. Impact of sea-water on the quasi static and fatigue flexural properties of GFRP. *Composite Structures*, *97*, pp.222-230.

[28] Wei, B., Cao, H. and Song, S., 2011. Degradation of basalt fibre and glass fibre/epoxy resin composites in seawater. *Corrosion Science*, *53*(1), pp.426-431.

[29] Gu, H., 2009. Behaviours of glass fibre/unsaturated polyester composites under seawater environment. *Materials & Design*, *30*(4), pp.1337-1340.

[30] Kotsikos, G., Evans, J.T., Gibson, A.G. and Hale, J.M., 2000. Environmentally enhanced fatigue damage in glass fibre reinforced composites characterised by acoustic emission. *Composites Part A: Applied Science and Manufacturing*, *31*(9), pp.969-977.

[31] Nguyen, T., Tang, H., Chuang, T.J., Chin, J., Wu, F. and Lesko, J., 2000. A fatigue model for fiber-reinforced polymeric composites for offshore applications. *NIST Technical Note*.

[32] Liao, K., Schultheisz, C.R. and Hunston, D.L., 1999. Effects of environmental aging on the properties of pultruded GFRP. *Composites Part B: Engineering*, *30*(5), pp.485-493.

[33] Nunemaker, J.D., Voth, M.M., Miller, D.A., Samborsky, D.D., Murdy, P. and Cairns, D.S., 2018. Effects of moisture absorption on damage progression and strength of unidirectional and cross-ply fiberglass–epoxy composites. *Wind Energy Science*, *3*(1), p.427.

[34] Shan, Y. and Liao, K., 2002. Environmental fatigue behavior and life prediction of unidirectional glass–carbon/epoxy hybrid composites. *International Journal of Fatigue*, *24*(8), pp.847-859.

[35] Krauklis, A.E., Gagani, A.I., Vegere, K., Kalnina, I., Klavins, M. and Echtermeyer, A.T., 2019. Dissolution Kinetics of R-Glass Fibres: Influence of Water Acidity, Temperature, and Stress Corrosion. *Fibers*, *7*(3), p.22.

[36] Qiu, Q. and Kumosa, M., 1997. Corrosion of E-glass fibers in acidic environments. *Composites Science and Technology*, *57*(5), pp.497-507.

[37] Schmitz, G.K. and Metcalfe, A.G., 1966. Stress corrosion of E-glass fibers. *Industrial & Engineering Chemistry Product Research and Development*, *5*(1), pp.1-8.

[38] Andreades C, Mahmoodi P and Ciampa F. Characterisation of smart CFRP composites with embedded PZT transducers for nonlinear ultrasonic applications. *Composite Structures*. 2018; 206: 456-466.

[39] Seaver M, Trickey ST and Nichols JM. Strain measurements from FBGs embedded in rotating composite propeller blades. In: *Optical Fiber Sensors*, 2006 Oct 23, p. ThD2. Optical Society of America.

[40] Chilles JS, Croxford A and Bond IP. Design of an embedded sensor, for improved structural performance. *Smart Materials and Structures*. 2015; 24(11): 115014.

[41] Tang HY, Winkelmann C, Lestari W, et al. Composite structural health monitoring through use of embedded PZT sensors. *Journal of Intelligent Material Systems and Structures*. 2011; 22(8): 739-755.

[42] Yang B, Xuan FZ, Jin P, et al. Damage Localization in Composite Laminates by Building in PZT Wafer Transducers: A Comparative Study with Surface-Bonded PZT Strategy. *Advanced Engineering Materials*. 2019; 21(3): 1801040.

[43] Dziendzikowski M, Kurnyta A, Dragan K, et al. In situ Barely Visible Impact Damage detection and localization for composite structures using surface mounted and embedded PZT transducers: A comparative study. *Mechanical Systems and Signal Processing*. 2016; 78:91-106.

[44] Ghasemi-Nejhad MN, Russ R and Pourjalali S. Manufacturing and testing of active composite panels with embedded piezoelectric sensors and actuators. *Journal of Intelligent Material Systems and Structures*. 2005; 16(4): 319-333.

[45] Mall S. Integrity of graphite/epoxy laminate embedded with piezoelectric sensor/actuator under monotonic and fatigue loads. *Smart Materials and Structures*. 2002; 11(4): 527-533.

[46] Mall S and Coleman JM. Monotonic and fatigue loading behavior of quasi-isotropic graphite/epoxy laminate embedded with piezoelectric sensor. *Smart Materials and Structures*. 1998; 7(6): 822-832.

[47] Masmoudi S, El Mahi A and Turki S. Fatigue behaviour and structural health monitoring by acoustic emission of E-glass/epoxy laminates with piezoelectric implant. *Applied Acoustics*. 2016; 100(108): 50-58.

[48] Paget CA and Levin K. Structural integrity of composites with embedded piezoelectric ceramic transducers. In: *Smart Structures and Materials 1999: Smart Structures and Integrated Systems*, 1999 Jun 9, Vol. 3668, pp.306-313. International Society for Optics and Photonics.

[49] Qing XP, Beard SJ, Kumar A, et al. Built-in sensor network for structural health monitoring of composite structure. *Journal of Intelligent Material Systems and Structures*. 2007; 18(1): 39-49.

[50] Schulze R, Streit P, Fischer T, et al. Fiber-reinforced composite structures with embedded piezoelectric sensors. In: *SENSORS, 2014 IEEE*, 2014 Nov 2, pp.1563-1566. IEEE.

[51] Lampani L, Sarasini F, Tirillò J, et al. Analysis of damage in composite laminates with embedded piezoelectric patches subjected to bending action. *Composite Structures*. 2018; 202: 935-942.

[52] Lin M and Chang FK. The manufacture of composite structures with a built-in network of piezoceramics. *Composites Science and Technology*. 2002; 62(7-8): 919-939.

[53] Osmont DL, Dupont M, Gouyon R, et al. Piezoelectric transducer network for dual-mode (active/passive) detection, localization, and evaluation of impact damages in carbon/epoxy composite plates. In: *Fifth European Conference on Smart Structures and Materials*, 2000 Aug 24, Vol. 4073, pp.130-137. International Society for Optics and Photonics.

[54] Sala G, Olivier M, Bettini P, et al. Embedded piezoelectric sensors and actuators for control of active composite structures. In: *6th Cranfield Conference on Dynamics and Control of Systems and Structures in Space*, 2004, pp.437-446. Mechanical and Thermal Engineering Department, Carlo Gavazzi Space ESTEC, European Space Agency.

[55] Liew, CK and Veidt, M. Review of integrated piezoceramic transducers in smart materials and structures. In: Nelson WG *Piezoelectric materials: Structure, properties and applications*. New York, U.S.A.: Nova Science Publishers, 2010, pp.109-132.

2

Identifying Hot-spots at Composite Marine Propeller

2.1. INTRODUCTION

Marine propellers are one of the principal components that provide propulsion for ships. The flexible marine propellers made of fibre reinforced composite materials have been emerging during the past decades. In contrast to the conventional rigid propellers made of nickel-aluminium-bronze (NAB) or manganese bronze (MB), the composite materials can reduce the weight, improve corrosion resistance, and potentially cut down the maintenance expense [1]. Besides, composite propellers can offer increased cavitation inception speed [2-4] and lower the electro-magnetic signature [5]. A tailor-designed hydro-elastic behaviour of flexible composite propellers can also contribute to an improved propeller efficiency at off-design conditions [6]. In order to unlock these benefits of composite marine propellers, extensive research has been undertaken, as highlighted below.

The performance of composite propellers has been studied both numerically and experimentally. Various numerical modelling methods have been developed to simulate the fluid-structure interaction (FSI) effect for composite marine propellers operating in water environment. In principle, they are classified into inviscid and viscous FSI methods [7, 8]. The first category consists of a computational structural dynamics model coupled with the blade element momentum theory [9], the lifting line [10] or lifting surface [11] method, or the boundary element method [12]. The other category includes the coupling of computational structural dynamics and fluid dynamics methods [13, 14]. A comprehensive overview of the different numerical modelling methods is given by Young et al. [7], in which the advantages, drawbacks, and the applications of each method have been introduced. The FSI analysis methods have also been used together with genetic algorithms to optimise the lay-up configuration of the composite laminates, analyse the self-twisting behaviour of composite blades, and improve the propeller efficiency at off-design conditions. Some other studies about propeller efficiency improvement can be found in [6, 15-19]. Optimisation studies with focus on delaying cavitation [2-4] and improving vibration properties [5] have also been performed.

Compared to numerical simulations, fewer publications seem to have addressed the performance of composite marine propellers experimentally. For example, a 340 mm diameter propeller with two blades made of glass fibre reinforced plastic (GFRP) material and carbon fibre reinforced plastic (CFRP), respectively, was used by Maljaars et al. [20]. The displacements at blade tip regions recorded in static tests were employed in a unique mixed numerical-experimental technique to determine the material stiffness properties. Besides, four propellers with the diameter of 340 mm and the blades made of GFRP material, bronze and epoxy, respectively, were tested by Maljaars et al. [21]. The blade deformations were used to validate their fluid-structure interaction simulations. A 610 mm diameter propeller made of CFRP material was tested by Chen et al. [4]. Their research highlighted the improved propeller performance in terms of efficiency and cavitation when compared to the rigid counterpart. The uniform wake fields were employed in the experiments performed by Young [22], while the non-uniform wake fields were used by Chen et al. [4], and the steady flow was used by Takentani [23]. The measuring techniques include digital image correlation technique used by Maljaars et al. [24, 25], and laser tracking technique used by Young [22]. Both were shown to work well to measure the blade deformations in the

considered test conditions. The tip displacements and axial displacements of mid-chord points were experimentally obtained by Maljaars and Dekker [24]. The experimental records revealed that the blade stiffness is about half the predicted level by their hydrodynamic analysis. A composite propeller with appropriate design of stacking sequence was tested by Raj et al. [3], and showed enhanced cavitation performance when compared to the metallic counterpart.

As discussed above, the previous research has made notable progresses in simulating and measuring the flexible composite propeller performance, and highlighted the promising future of composite marine propellers. Nevertheless, the limited focus on and understanding of the fatigue performance of composite propellers, especially in harsh seawater environment, seem to have limited their adoption rate for more widespread applications [7, 8].

In the present research, the fatigue performance of a composite marine propeller is studied numerically and experimentally. The approach is formulated in two steps: first, a numerical study is presented which aims to identify the critical areas of the composite marine propeller blade. Next, an experimental investigation on fatigue behaviour of the composite propeller is carried out. In this chapter it is organised as follows: the details of the numerical model of the investigated composite marine propeller, including geometry and dimensions, lay-up configuration of the composite laminates, and 60 load cases in a full revolution, are described in section 2. Section 3 explains the calculation of failure index according to Tsai-Wu failure criterion. As examples, considering the 1st, 20th, and 55th load cases, the numerical outputs of the maximum failure index at each ply of the composite laminates, together with their attributes, are presented in section 3. The same FE analysis method has been applied to the other load cases. In section 4, the critical locations are identified according to the numerical outputs of the maximum failure index at all load cases. Moreover, the critical stress and moment resultants of the hot-spot elements are calculated. The most critical hot-spot element is finally determined by comparing the critical resultants.

2.2. NUMERICAL MODEL OF COMPOSITE BLADE

2.2.1. PROPELLER DESCRIPTION

The geometry, dimensions, and layup of the case-study CFRP propeller are the same as the one researched by Maljaars [26]: a four-blade propeller with the diameter of 1 m. The blades have a sandwich structure (Fig. 2.1). The blade faces in this research, however, are made of CFRP laminates, different to the GFRP propeller of Maljaars. The laminates consist of an outer ply of woven CFRP and multiple plies of unidirectional (UD) CFRP. The outer fabric plies help to minimise the damage to the blades created by impact loads. The blade core is made using polymat/resin rich material. The density of blade core material is 1200 kg/m^3. Elastic and strength properties of the isotropic core material, the woven and the UD CFRP materials are listed in Table 2.1 and Table 2.2, respectively. The mechanical properties include the ply thickness (t), Young's modulus (E), shear modulus (G), Poisson's ratio (v), tensile and compressive strengths (σ^t and σ^c), and shear strength (S). The subscripts L, T and H denote

the longitudinal, the transverse and the through-thickness directions relative to the fibre direction, respectively.

Table 2.1 Elastic properties of the polymat/resin rich material, the woven and the UD CFRP materials.

Elastic properties	polymat/resin rich material	woven CFRP lamina	UD CFRP lamina
t [mm]	Variable	0.19	0.15
E_L, E_T, E_H [GPa]	4	70, 70, 11.2	140, 11.9, 11.9
$\nu_{LT}, \nu_{TH}, \nu_{HL}$ [-]	0.3	0.05, 0.4, 0.29	0.29, 0.4, 0.29
G_{LT}, G_{TH}, G_{HL} [GPa]	1.538	4.9, 3.92, 3.92	4.9, 4.17, 4.9

Table 2.2 Strength properties of the polymat/resin rich material, the woven and the UD CFRP materials.

Strength properties	polymat/resin rich material	woven CFRP lamina	UD CFRP lamina
$\sigma_L^t, \sigma_T^t, \sigma_H^t$ [MPa]	N/A	910, 910, 70	2100, 84, 84
$\sigma_L^c, \sigma_T^c, \sigma_H^c$ [MPa]	N/A	665, 665, 70	1540, 280, 266
S_{LT}, S_{TH}, S_{HL} [MPa]	N/A	126, 84, 112	126, 119, 126

2.2.2. BLADE MODEL AND LOAD CASES

A solid model of the composite marine propeller blade is shown in Fig. 2.1, where the blade core was discretised using isotropic three-dimensional (3D) 20-node solid elements, and the blade faces were discretised using 3D 20-node composite brick elements. They have 3 degrees of freedom (DOF) at each node. A mesh density of 29×30×4 has been applied for spatial discretisation. 29 elements were placed along the chord, 30 elements in the radial direction, and 4 elements in through-thickness direction. The total number of elements was 2880. In the through-thickness direction, each of the four elements contributed to specific percentage of local blade thickness. A composite element at pressure or suction side constituted 31.25% of total thickness, and each of the two isotropic elements constituted 18.75%. A mesh convergence study has shown that this mesh density provided an accurate estimation on blade structural response [20, 21]. The model was implemented in the commercial FE analysis software MARC/Mentat. The isotropic and composite elements are type 21 and type 150, respectively. The latter account for different material properties and fibre directions in each ply of the composite laminate.
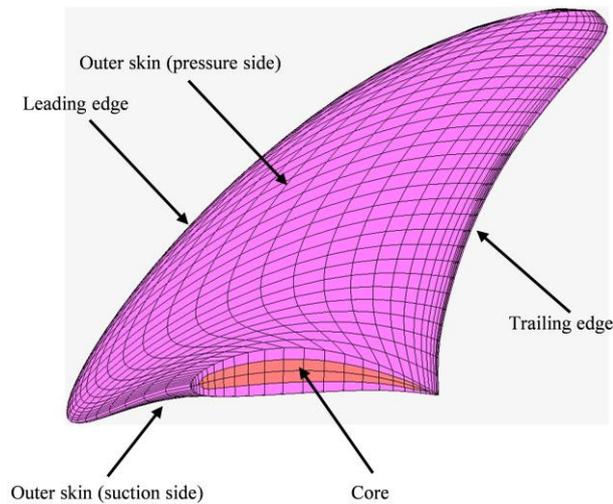
Fig. 2.1: FE model of the composite marine propeller blade and cross-sectional view: blade faces (magenta) and core (orange).

For doubly curved composite structures, proper definition of material orientations plays a key role in accurately predicting the structural response [27]. A user-developed approach was implemented to define the element-dependent (local) material orientations in the blade model (Fig. 2.2). According to this approach: direction 3 is the normal to element surface tangent plane and the positive direction points to outside surface of the element, direction 2 is the intersection between the element surface tangent plane and the (global) x-y plane and positive to starboard side, and direction 1 is therefore defined as the outer product of directions 2 and 3. For a composite element, the fibre orientation in each ply is defined as the angle with respect to direction 2. In Fig. 2.3 the blade model is presented in terms of lay-up configurations of the composite laminates, with each colour representing a unique stacking sequence. The different stacking sequences are listed in Appendix A.2.1. The positive fibre angle is defined in the anticlockwise direction with respect to the positive 2-direction.
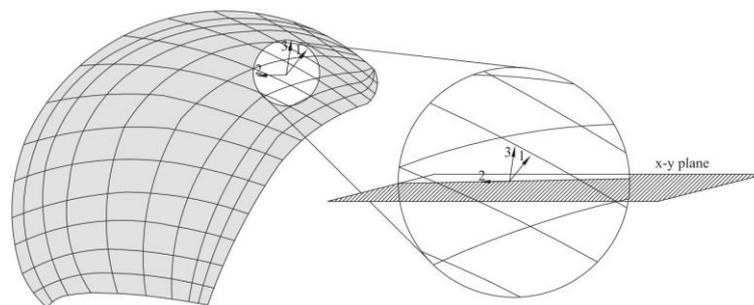
Fig. 2.2: Defining element-dependent (local) material orientation (image taken from [20] with permission of the author).

13
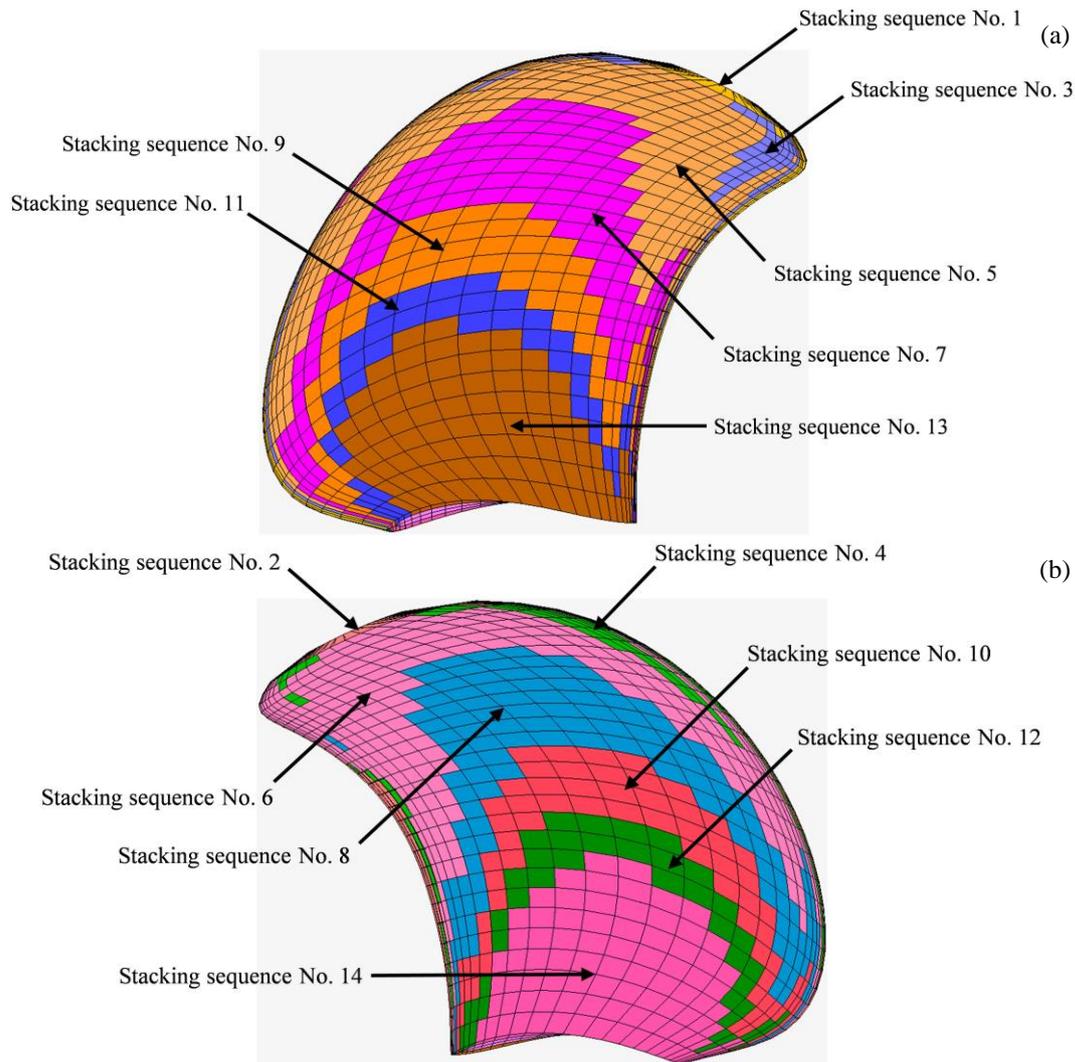
Fig. 2.3: The plot of lay-up configurations of CFRP laminates: (a) pressure side, and (b) suction side.

The load cases have been computed for a unique scenario. Considering a vessel to sail in straight path in calm water at the speed of 10.4 knots (5.35 m/s) [26]. The propeller working at the constant rotational speed of 600 rpm experiences a non-uniform wake field. Regarding to different positions at the wake field, a full revolution of the propeller was evenly divided into 60 time steps. For each time step, the velocity potential was first converted to pressure filed via Bernoulli's equation, and the pressure distribution over blade surfaces were then converted to nodal forces acting at the centroid of blade face elements (Fig. 2.4). The composite blades are bonded to the hub. Assuming the hub is much stiffer than the composite blade, therefore, the blade model is modelled as fully clamped at the blade-hub interface (Fig. 2.4). A critical assessment of the quality of this assumption and possible improvement are recommended for the future research.
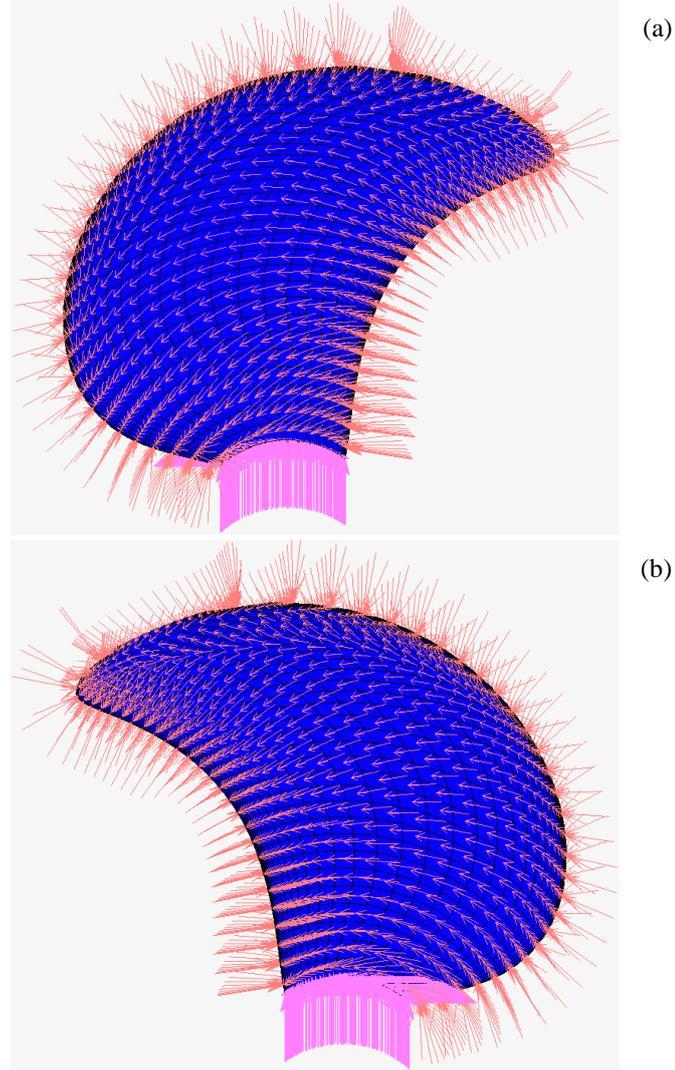
Fig. 2.4: The boundary and loading conditions: (a) pressure side, and (b) suction side.

2.3. FE ANALYSIS OF FAILURE INDEX

The three-dimensional Tsai-Wu failure criterion was employed in the numerical analysis to identify the hot-spots at the composite blade. The failure index of Tsai-Wu failure criterion is expressed as [28-33]:

$$FI = F_1\sigma_1 + F_2\sigma_2 + F_3\sigma_3 + F_{11}\sigma_1^2 + F_{22}\sigma_2^2 + F_{33}\sigma_3^2 + F_{44}\tau_{12}^2 + F_{55}\tau_{23}^2 + F_{66}\tau_{31}^2 + 2F_{12}\sigma_1\sigma_2 +$$
$$2F_{23}\sigma_2\sigma_3 + 2F_{31}\sigma_3\sigma_1, \tag{2.1}$$

where σ and τ are the normal and shear stresses, respectively, and $\tau_{ij} = \tau_{ji}$. The 1st and 2nd order strength tensors (F_i and F_{ij}, $i, j = 1, 2, \dots \dots, 6$) are expressed as:

$$F_1 = 1/\sigma_1^t - 1/\sigma_1^c, \tag{2.2}$$

$$F_2 = 1/\sigma_2^t - 1/\sigma_2^c, \tag{2.3}$$

$$F_3 = 1/\sigma_3^t - 1/\sigma_3^c, \tag{2.4}$$

$$F_{11} = 1/(\sigma_1^t \sigma_1^c), \tag{2.5}$$

$$F_{22} = 1/(\sigma_2^t \sigma_2^c), \tag{2.6}$$

$$F_{33} = 1/(\sigma_3^t \sigma_3^c), \tag{2.7}$$

$$F_{44} = 1/(S_{12})^2, \tag{2.8}$$

$$F_{55} = 1/(S_{23})^2, \tag{2.9}$$

$$F_{66} = 1/(S_{31})^2, \tag{2.10}$$

$$F_{12} = -0.5/\sqrt{\sigma_1^t \sigma_1^c \sigma_2^t \sigma_2^c}, \tag{2.11}$$

$$F_{23} = -0.5/\sqrt{\sigma_2^t \sigma_2^c \sigma_3^t \sigma_3^c}, \tag{2.12}$$

$$F_{31} = -0.5/\sqrt{\sigma_3^t \sigma_3^c \sigma_1^t \sigma_1^c}, \tag{2.13}$$

where σ^t and σ^c are the tensile and compressive strengths, respectively, and S is the shear strength. The Tsai-Wu failure criterion takes into account the interactions between different stress components, and it is easy to calculate the failure index via one scalar equation. $FI \geq 1$ indicates the failure of composite material.

The blade thrust variation of glass-epoxy and carbon-epoxy Seiun-Maru propellers, due to blade flexibility, was researched in [34]. In a full revolution, the blade thrust calculated using a linear static analysis turns to meet well with the output resulted from a hydro-elastic analysis. Therefore, for each of the 60 load cases in a full revolution, a linear static analysis was performed using the present blade model. Due to the layered structure of the CFRP laminates, the failure index at each ply was investigated. Considering load case 1, for example, the contour plots of failure index at ply 4 and ply 6 are given in Figs. 2.5 and 2.6, respectively. Furthermore, the corresponding maximum failure index (FI_{max}) at each ply is determined. As shown in Fig. 2.5(c), at ply 4, the maximum failure index of 0.288 exists at elements 1363 and 1421. At ply 6, the maximum failure index of 0.171 is located at elements 1421 and 1479 (Fig. 2.6(c)). Due to the curved geometry, these elements have one edge much longer than the shortest edge, i.e., they have large aspect ratio. The accuracy of FE analysis results may deteriorate. Therefore, the effect of element aspect ratio should be concerned in later research.

For the numerical analysis with load cases 1, 20 and 55, the relevant outputs data are provided in Tables 2.3, 2.4 and 2.5. The geometrical reference of all the elements listed in the three tables (apart from elements 24 and 29, 1305, 1306, 1363, 1364, 1421 and 1479 which are presented in Figs. 2.7 and 2.8, respectively) are shown in Appendix A.2.2.

(a)

(b)

(c)

Element 1421

Element 1363
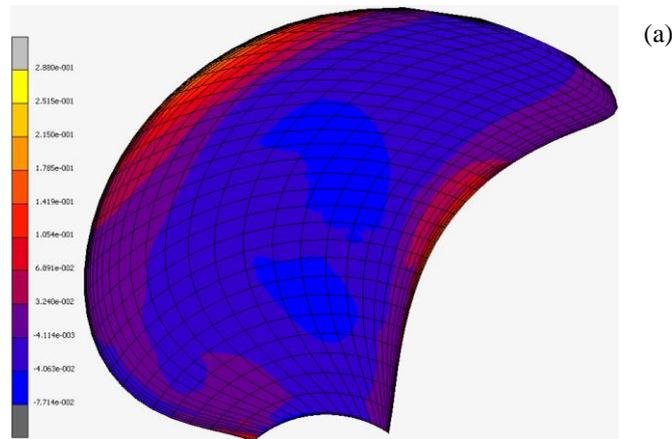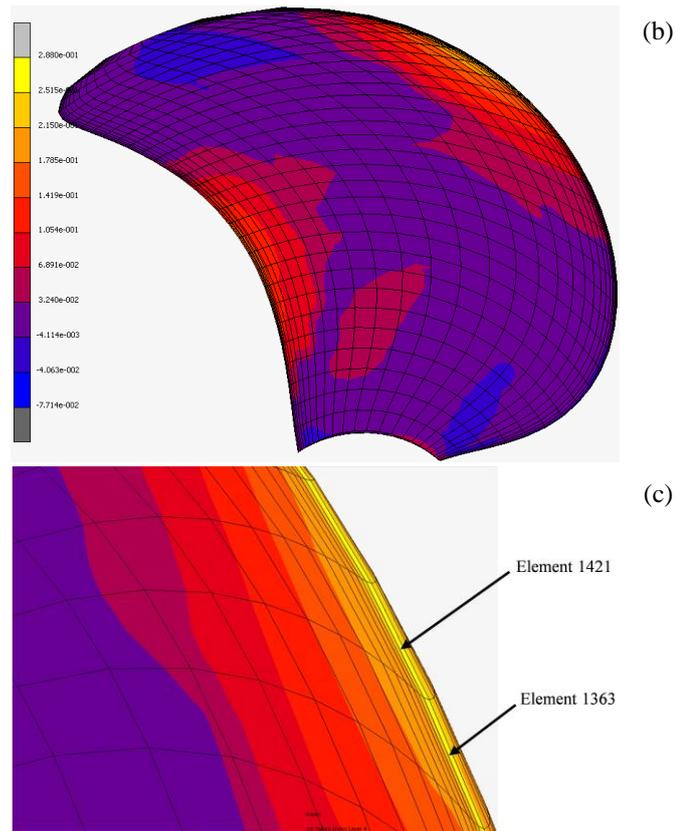
Fig. 2.5: FE analysis result of Tsai-Wu failure index at ply 4 of CFRP laminates (load case 1): (a) pressure side, (b) suction side, and (c) attributes of the maximum failure index.

(a)

(b)
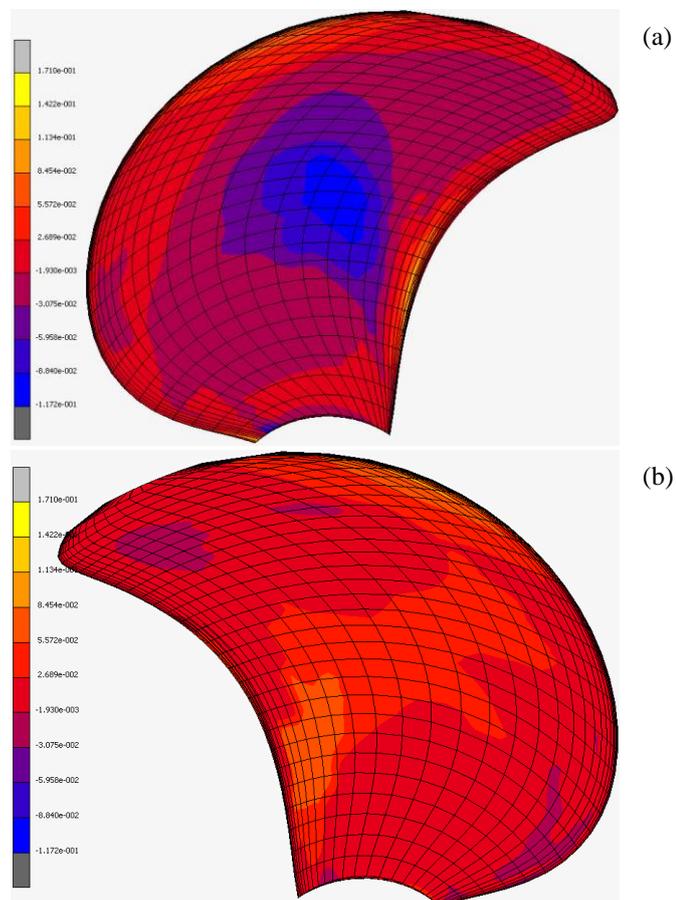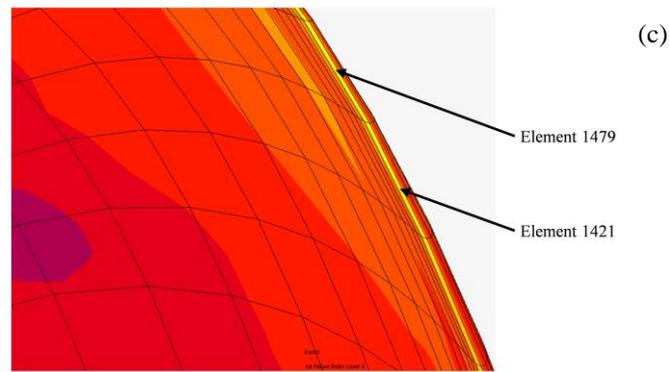
Fig. 2.6: FE analysis result of Tsai-Wu failure index at ply 6 of CFRP laminates (load case 1): (a) pressure side, (b) suction side, and (c) attributes of the maximum failure index.

Table 2.3: The maximum failure index in each ply and the corresponding attributes (load case 1).

FI_{max}	Ply No.	Element No.	FI_{max}	Ply No.	Element No.
0.053	1	626, 627	0.064	10	24
0.156	2	1363, 1421	0.053	11	27
0.160	3	24	0.066	12	24
0.288	4	1363, 1421	0.069	13	286, 344
0.150	5	1364	0.030	14	35, 36
0.171	6	1421, 1479	0.038	15	20, 21, 78, 79
0.129	7	577	0.035	16	169, 170
0.109	8	24	0.037	17	169, 170
0.110	9	345, 403	0.016	18	42, 43, 100, 101

Table 2.4: The maximum failure index in each ply and the corresponding attributes (load case 20).

FI_{max}	Ply No.	Element No.	FI_{max}	Ply No.	Element No.
0.051	1	626, 627	0.063	10	24
0.154	2	1363, 1421	0.062	11	27
0.144	3	24	0.067	12	24
0.284	4	1363, 1421	0.072	13	286, 344
0.148	5	1306, 1364	0.030	14	35
0.168	6	1363, 1421	0.034	15	79
0.130	7	577	0.035	16	169, 170
0.103	8	24	0.040	17	169, 170
0.115	9	345, 403	0.015	18	42, 43, 100, 101

Table 2.5: The maximum failure index in each ply and the corresponding attributes (load case 55).

FI_{max}	Ply No.	Element No.	FI_{max}	Ply No.	Element No.
0.052	1	626, 627	0.068	10	24
0.144	2	29	0.052	11	27
0.175	3	24	0.069	12	24
0.261	4	1305, 1363	0.066	13	286, 344
0.138	5	1248, 1306	0.031	14	35, 36
0.153	6	1363, 1421	0.042	15	20, 21, 78, 79
0.115	7	577	0.034	16	169, 170
0.117	8	24	0.037	17	73
0.103	9	345, 403	0.018	18	42, 100

2.4. CRITICAL LOCATIONS (HOT-SPOTS) OF COMPOSITE BLADE

2.4.1. THE FOUR LARGEST MAXIMUM FAILURE INDICES

For all the other load cases, the same analysis method has been applied to determine the maximum failure index at each ply of the CFRP laminates. Under a specific load case p ($p = 1, 2, ..., 60$), the maximum failure indices of all plies were sorted in descending order. The kth ($k = 1, 2, 3, 4$) largest maximum failure index, which is denoted as $FI^p_{max,k}$, are listed in Appendix A.2.3. The corresponding attributes of the four largest maximum failure indices, i.e., the specific ply number ($ply^p_{max,k}$) and element number(s) ($ele^p_{max,k}$), are listed in Appendices A.2.4 and A.2.5, respectively.

A statistical analysis concerning the frequency distribution of $ele^p_{max,k}$ is summarised in Table 2.6. For example, the first largest maximum failure index ($FI^p_{max,1}$) has been observed at element 1305 under 18 out of the 60 load cases ($p_1 = 18$), at element 1363 under each load case ($p_1 = 60$), and at element 1421 for 44 times ($p_1 = 44$). The second largest maximum failure index ($FI^p_{max,2}$) has been observed at element 24, 1363, 1421, and 1479 for 10, 48, 50, and 2 times ($p_2 = 10, 48, 50,$ and 2), respectively. The locations of all $ele^p_{max,k}$ are presented in Figs. 2.7 and 2.8. It can be observed that the neighbouring elements 1305, 1306, 1363, 1364, 1421, and 1479 are located at the leading edge of the blade, while the elements 24 and 29 are located at the blade root. Because the blade model is fully clamped at blade-hub interface (Fig. 2.4), which does not represent the realistic boundary condition, further analysis of elements 24 and 29 is not prioritised and these two elements are not considered among the hot-spots. Further assessment of this consideration will be the subject of future research.

Table 2.6: Frequency distribution of attributes of the four largest maximum failure indices.

$ele_{max,k}^{p}$	p_1	p_2	p_3	p_4
24	N/A	10	17	6
29	N/A	N/A	N/A	4
1305	18	N/A	N/A	N/A
1306	N/A	N/A	N/A	27
1363	60	48	42	23
1364	N/A	N/A	N/A	27
1421	44	50	43	23
1479	N/A	2	1	N/A
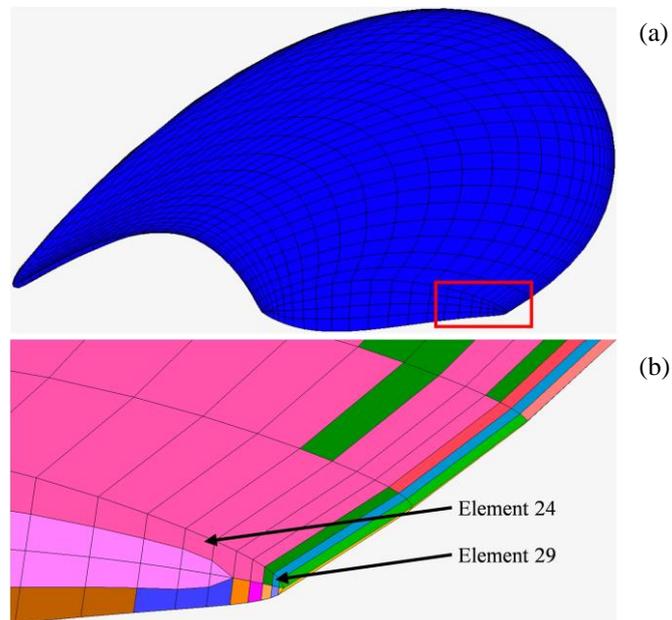
Fig. 2.7: The location of elements 24 and 29: (a) global view, and (b) zooming in on blade root, and plot in respect of lay-up configuration.
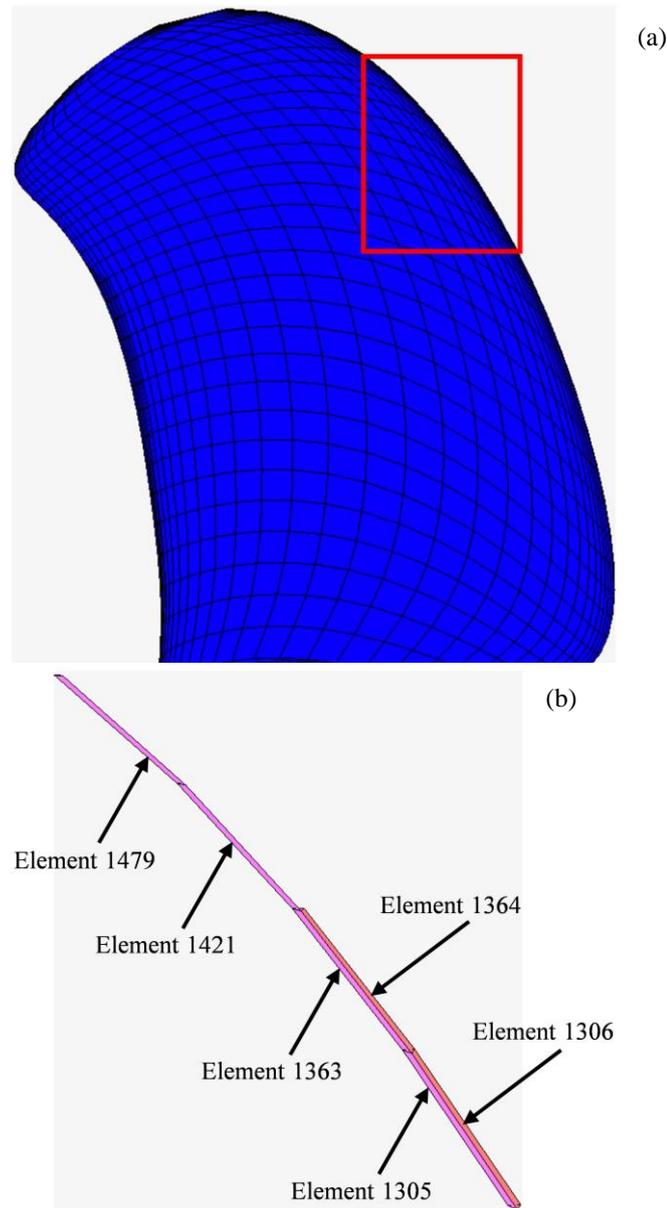
Fig. 2.8: The location of elements 1305, 1306, 1363, 1364, 1421 and 1479: (a) global view, and (b) zooming in on trailing edge, and plot in respect of lay-up configuration.

2.4.2. IDENTIFYING HOT-SPOTS

All the $ele^{p}_{max,k}$ are classified with respect to their lay-up configurations in Table 2.7. First, in view of their unique lay-up configurations, the elements 1306 and 1364 are identified as the hot-spots. The neighbouring elements 1305, 1363, 1421, 1479 have identical lay-up configuration. Considering the frequency distribution in Table 2.6, elements 1363 and 1421 are more critical than the other two. Therefore, they are added to the list of hot-spots.

21

Table 2.7: Lay-up configurations of composite elements.

$ele^p_{max,k}$	Lay-up configuration
1305, 1363, 1421, 1479	woven/0/-90/-45/-90/0
1306, 1364	woven/0/90/45/90/0

2.4.3. CRITICAL LOAD CASE

For each hot-spot element, the corresponding largest (ever) maximum failure index ($FI^{p_{crit}}_{max}$) under all the load cases is given in Table 2.8. Meanwhile the corresponding load case is treated as the critical load case index (p_{crit}). For example, for the hot-spot element 1306, the largest ever maximum failure index of 0.1477 has been observed under the 20th load case.

Table 2.8: The largest maximum failure indices of hot-spot elements, and the corresponding critical load cases.

Hot-spot element No.	Critical load case (p_{crit})	Largest maximum failure index $(FI^{p_{crit}}_{max})$
1306	20	0.1477
1363	59	0.3169
1364	20	0.1477
1421	59	0.3169

2.4.4. CRITICAL STRESS AND MOMENT RESULTANTS

The blade faces in the FE model were discretised using 3D composite elements (type 150). This element type has four integration points at each ply [35]. The outputs of FE analysis can provide the stress state of each integration point. The ply-wise stress state of the composite element is calculated by averaging the stresses at the four integration points:

$$\sigma^{(i)} = \frac{\sigma^{(i,1)} + \sigma^{(i,2)} + \sigma^{(i,3)} + \sigma^{(i,4)}}{4}, \tag{2.14}$$

where $\sigma^{(i)}$ denotes the stresses of ply i, and $\sigma^{(i,1)}$, $\sigma^{(i,2)}$, $\sigma^{(i,3)}$ and $\sigma^{(i,4)}$ are the stresses of the four integration points.

The through-thickness integration of in-plane stresses produces the stress (N) and moment (M) resultants. Because of the layered structure of the composite elements, the integration can be converted to the summation of ply-wise stresses. The operations of integration and summation are performed in accordance with the classical laminate theory [36]:

$$N_1 = \int_{-\frac{T}{2}}^{\frac{T}{2}} \sigma_1 \, dz = \sum_{i=1}^{n} \sigma_1^{(i)} t^{(i)}, \tag{2.15}$$

$$N_2 = \int_{-\frac{T}{2}}^{\frac{T}{2}} \sigma_2 \, dz = \sum_{i=1}^{n} \sigma_2^{(i)} t^{(i)}, \tag{2.16}$$

$$N_{12} = \int_{-\frac{T}{2}}^{\frac{T}{2}} \sigma_{12} dz = \sum_{i=1}^{n} \sigma_{12}^{(i)} t^{(i)}, \tag{2.17}$$

$$M_1 = \int_{-\frac{T}{2}}^{\frac{T}{2}} \sigma_1 z dz = \sum_{i=1}^{n} \sigma_1^{(i)} t^{(i)} \left(h^{(i)} - \frac{T}{2} \right), \tag{2.18}$$

$$M_2 = \int_{-\frac{T}{2}}^{\frac{T}{2}} \sigma_2 z dz = \sum_{i=1}^{n} \sigma_2^{(i)} t^{(i)} \left(h^{(i)} - \frac{T}{2} \right), \tag{2.19}$$

$$M_{12} = \int_{-\frac{T}{2}}^{\frac{T}{2}} \sigma_{12} z dz = \sum_{i=1}^{n} \sigma_{12}^{(i)} t^{(i)} \left(h^{(i)} - \frac{T}{2} \right), \tag{2.20}$$

where $t^{(i)}$ is the thickness of ply i, $h^{(i)}$ is the height (of the mid-plane) of ply i, and T is the total element thickness (Fig. 2.9).

Under the corresponding critical load case (Table 2.8), the stress and moment resultants of each hot-spot element, i.e., the critical stress ($N^{p crit}$) and moment ($M^{p crit}$) resultants, are calculated according to Eqs. 2.14 to 2.20. The calculation results are given in Table 2.9.
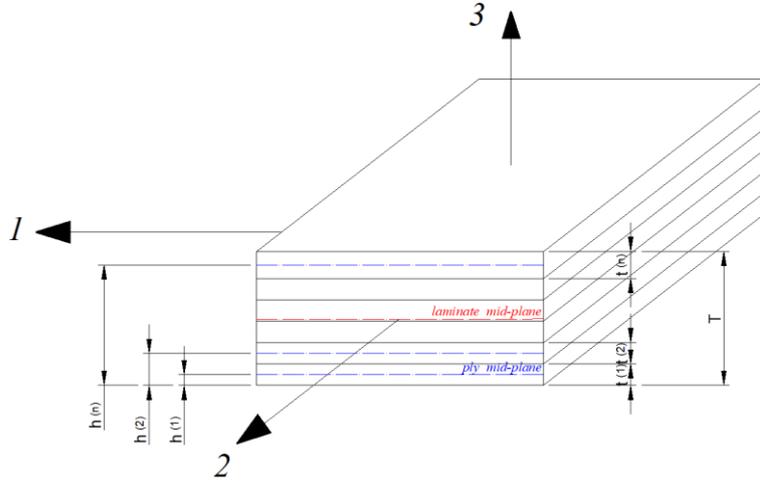
Fig. 2.9: The cross section of CFRP laminate.

Table 2.9: Critical stress and moment resultants of the hot-spot elements.

Hot-spot element No.	$N_1^{p crit}$ [MPa·mm]	$N_2^{p crit}$ [MPa·mm]	$N_{12}^{p crit}$ [MPa·mm]	$M_1^{p crit}$ [MPa·mm²]	$M_2^{p crit}$ [MPa·mm²]	$M_{12}^{p crit}$ [MPa·mm²]
1306	10.7	54.3	3.0	-0.0	1.5	0.7
1363	21.1	34.3	-2.9	3.1	-1.0	-1.2
1364	11.3	50.4	3.1	0.2	1.5	0.8
1421	22.5	37.5	-2.6	3.6	-1.6	-1.1

2.4.5. COMPARING HOT-SPOT ELEMENTS

In view of the frequency distribution in Table 2.6, elements 1363 and 1421 are identified as the most severely-stressed elements. Moreover, the comparison of their critical stress and moment resultants shows that element 1421 generally has higher stress level. Though $N_{12}^{p crit}$ of element 1363 is slightly larger than that of element 1421, the expected contribution of in-plane shear stress to the failure of the

23

element is much lower than normal stresses. Therefore, element 1421 is considered as the most critical area. To investigate the fatigue lifetime of the propeller working under the considered operation condition, the lay-up configuration and stress states of element 1421 will be employed in designing fatigue tests. For element 1421, note that the stress and moment resultants under each load case have been calculated, and are given in Appendix A.2.6.

2.5. CONCLUSION

Despite significant progress in composite propeller design, limited understanding on the fatigue performance of composite propeller working in aggressive seawater environment hinders the potential widespread application. A numerical study which aims at identifying hot-spots in a composite propeller is presented in this chapter. The results will serve as the inputs for experimental investigation of fatigue properties. The numerical simulation and analysis present that:

- A FE model of a composite marine propeller blade was created using solid elements.
- A total of 60 load cases are generated from a full revolution of the blade in a specific non-uniform wake field.
- For each load case, the maximum failure index in each ply at every location in the blade was determined using the Tsai-Wu failure criterion.
- The critical elements and the corresponding critical plies were determined for each location. These were then compared to determine the most critical location and the corresponding load case in terms of applied stress and moment resultants. This is used as inputs to the follow-on experimental work.

REFERENCES

[1] Kane, C. and Smith, J., 2003. Composite blades in marine propulsors. In *Proceedings of International Conference on Advanced Marine Materials: Technologies and Applications*.

[2] International Towing Tank Conference Resistance Committee, 2005. Final report and recommendations to the 24th ITTC. In *Proceedings of 24th international towing tank conference, Edinburgh, UK, 2005*.

[3] Raj, S. and Reddy, R., 2014. P. Bend-twist coupling and its effect on cavitation inception of composite marine propeller. *Int. J. Mech. Eng. Technol*, *5*, pp.306-314.

[4] CHEN, B., 2006. Design, fabrication and testing of pitch-adapting (flexible) composite propellers. In *Propellers/Shafting 2006 Symposium* (Vol. 8). SNAME.

[5] He, X.D., Hong, Y. and Wang, R.G., 2012. Hydroelastic optimisation of a composite marine propeller in a non-uniform wake. *Ocean engineering*, *39*, pp.14-23.

[6] Liu, Z. and Young, Y.L., 2009. Utilization of bend–twist coupling for performance enhancement of composite marine propellers. *Journal of Fluids and Structures*, *25*(6), pp.1102-1116.

[7] Young, Y.L., Motley, M.R., Barber, R., Chae, E.J. and Garg, N., 2016. Adaptive composite marine propulsors and turbines: progress and challenges. *Applied Mechanics Reviews*, *68*(6).

[8] Maljaars, P.J. and Kaminski, M.L., 2015. Hydro-elastic analysis of flexible propellers: an overview. In *Fourth International Symposium on Marine Propulsors*.

[9] Masters, I., Chapman, J.C., Willis, M.R. and Orme, J.A.C., 2011. A robust blade element momentum theory model for tidal stream turbines including tip and hub loss corrections. *Journal of Marine Engineering & Technology*, *10*(1), pp.25-35.

[10] Gonzalez-Martino, I., Costes, M., Rodriguez, B. and Devinant, P., 2012. Application of an unsteady curved lifting-line theory to propeller simulations. In *30th AIAA Applied Aerodynamics Conference* (p. 2917).

[11] Kerwin, J.E. and Lee, C.S., 1978. *Prediction of steady and unsteady marine propeller performance by numerical lifting-surface theory* (No. Paper No. 8).

[12] Young, Y.L. and Kinnas, S.A., 2001. A BEM for the prediction of unsteady midchord face and/or back propeller cavitation. *J. Fluids Eng.*, *123*(2), pp.311-319.

[13] Raj, S.S. and Reddy, P.R., 2011. Performance evaluation of composite marine propeller using L8 orthogonal array. *International Journal of Engineering Science and Technology*, *3*(11).

[14] Miller, R., Kim, S., Rhee, B. and Young, Y., 2012, August. Unsteady fluid structure interaction response of marine propellers in crashback. In *29th Symposium on Naval Hydrodynamics, Gothenburg, Sweden, Aug* (pp. 26-31).

[15] Plucinski, M.M., Young, Y.L. and Liu, Z., 2007, July. Optimization of a self-twisting composite marine propeller using Genetic algorithms. In *16th International conference on composite materials, Kyoto, Japan* (pp. 8-13).

[16] Lin, C.C., Lee, Y.J. and Hung, C.S., 2009. Optimization and experiment of composite marine propellers. *Composite structures*, *89*(2), pp.206-215.

[17] Blasques, J.P., Berggreen, C. and Andersen, P., 2010. Hydro-elastic analysis and optimization of a composite marine propeller. *Marine Structures*, *23*(1), pp.22-38.

[18] Lee, Y.J. and Lin, C.C., 2004. Optimized design of composite propeller. *Mechanics of advanced materials and structures*, *11*(1), pp.17-30.

[19] Mulcahy, N.L., Prusty, B.G. and Gardiner, C.P., 2010. Hydroelastic tailoring of flexible composite propellers. *Ships and Offshore structures*, *5*(4), pp.359-370.

[20] Maljaars, P.J., Kaminski, M.L. and Den Besten, J.H., 2017. Finite element modelling and model updating of small scale composite propellers. *Composite Structures*, *176*, pp.154-163.

[21] Maljaars, P., Bronswijk, L., Windt, J., Grasso, N. and Kaminski, M., 2018. Experimental validation of fluid–structure interaction computations of flexible composite propellers in open water conditions using BEM-FEM and RANS-FEM methods. *Journal of Marine Science and Engineering*, *6*(2), p.51.

[22] Young, Y.L., 2008. Fluid–structure interaction analysis of flexible composite marine propellers. *Journal of fluids and structures*, *24*(6), pp.799-818.

[23] Taketani, T., Kimura, K., Ando, S. and Yamamoto, K., 2013, May. Study on performance of a ship propeller using a composite material. In *The Third International Symposium on Marine Propulsors smp* (Vol. 13).

[24] Maljaars, P.J. and Dekker, J.A., 2014. Hydro-elastic analysis of flexible marine propellers. In *Maritime Technology and Engineering-Edited by Guedes Soares and Santos*, pp.705-715.

[25] Maljaars, P., Grasso, N., Kaminski, M. and Lafeber, W., 2017, June. Validation of a steady BEM-FEM coupled simulation with experiments on flexible small scale propellers. In *Proceedings of the Fifth International Symposium on Marine Propulsors, Espoo, Finland* (pp. 12-15).

[26] Maljaars, P.J., 2019. Hydro-elastic analysis of flexible marine propellers.

[27] Chen, J., Hallett, S. and Wisnom, M.R., 2010. Modelling complex geometry using solid finite element meshes with correct composite material orientations. *Computers & structures*, *88*(9-10), pp.602-609.

[28] Echaabi, J., Trochu, F. and Gauvin, R., 1996. Review of failure criteria of fibrous composite materials. *Polymer composites*, *17*(6), pp.786-798.

[29] París, F. and Jackson, K.E., 2001. A study of failure criteria of fibrous composite materials.

[30] Davila, C.G., Camanho, P.P. and Rose, C.A., 2005. Failure criteria for FRP laminates. *Journal of Composite materials*, *39*(4), pp.323-345.

[31] Icardi, U., Locatto, S. and Longo, A., 2007. Assessment of recent theories for predicting failure of composite laminates.

[32] Rajanish, M., Nanjundaradhya, N.V. and Ramesh, S.S., 2012. A Review Of Failure Of Composite Materials. *International Journal of Enginnering Research and Applications*, *3*, pp.122-124.

[33] De Luca, A. and Caputo, F., 2017.

[34] Maljaars, P., Kaminski, M. and Den Besten, H., 2018. Boundary element modelling aspects for the hydro-elastic analysis of flexible marine propellers. *Journal of Marine Science and Engineering*, *6*(2), p.67.

[35] A review on analytical failure criteria for composite materials. *AIMS Materials Science*, *4*(5), pp.1165-1185. Marc, M.S.C., 2010. Volume B: Element Library. *MSC. Software Corporation*, pp.113-661.

[36] Nettles, A.T., 1994. Basic mechanics of laminated composite plates.

APPENDIX

A.2.1: The stacking sequence of CFRP laminates at pressure and suction sides.

Stacking sequence No.	Lay-up configuration
1	[woven/0/90°/45°/90°/0]
2	[woven/0/-90°/-45°/-90°/0]
3	[woven/0/90°/45°/90°/0]
4	[woven/0/-90°/-45°/-90°/0]
5	[woven/0/90°/45°/90°/0]
6	[woven/0/-90°/-45°/-90°/0]
7	[woven/0/45°/90°/45°/90°/45°/0]
8	[woven/0/-45°/-90°/-45°/-90°/-45°/0]
9	[woven/0/45°/0/90°/45°/90°/0/45°/0]
10	[woven/0/-45°/0/-90°/-45°/-90°/0/-45°/0]
11	[woven/0/45°/0/-45°/90°/0/45°/0/90°/-45°/0/45°/0]
12	[woven/0/-45°/0/45°/-90°/0/-45°/0/-90°/45°/0/-45°/0]
13	[woven/0/90°/45°/-45°/0/-45°/90°/0/45°/0/90°/-45°/0/-45°/45°/90°/0]
14	[woven/0/-90°/-45°/45°/0/45°/-90°/0/-45°/0/-90°/45°/0/45°/-45°/-90°/0]

A.2.2: The geometrical reference of concerned elements in Tables 2.3, 2.4 and 2.5.
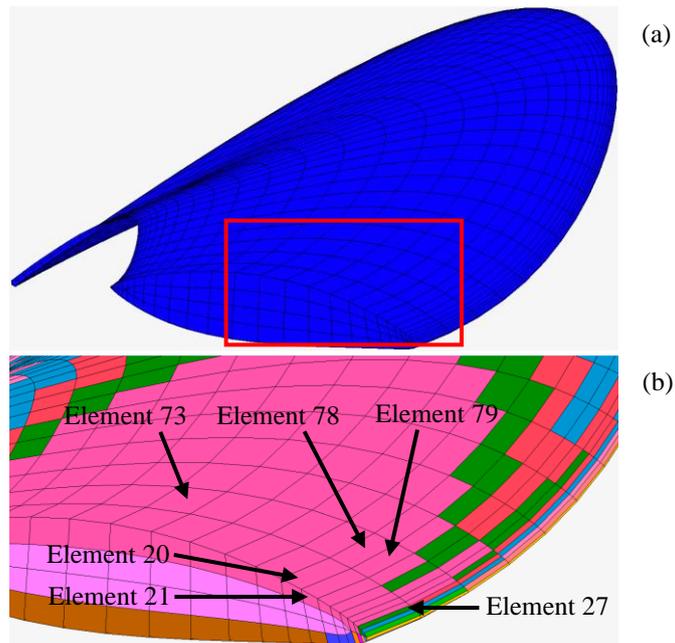
Fig. 2.10: The location of elements: (a) global view, and (b) zooming in, and plot in respect of lay-up configuration.
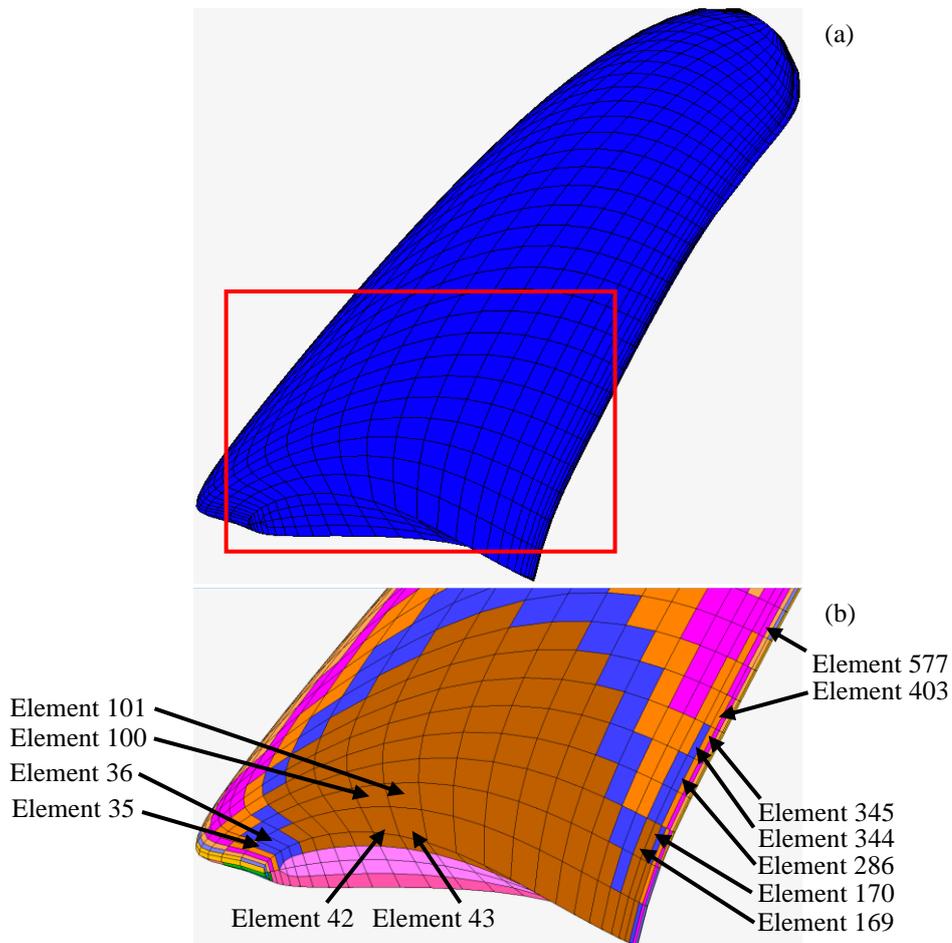
Fig. 2.11: The location of elements: (a) global view, and (b) zooming in, and plot in respect of lay-up configuration.
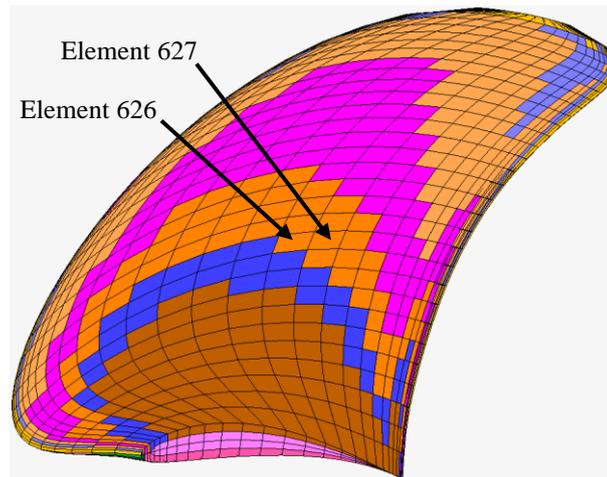
Fig. 2.12: The location of elements: plot in respect of lay-up configuration.

(a)

(b)
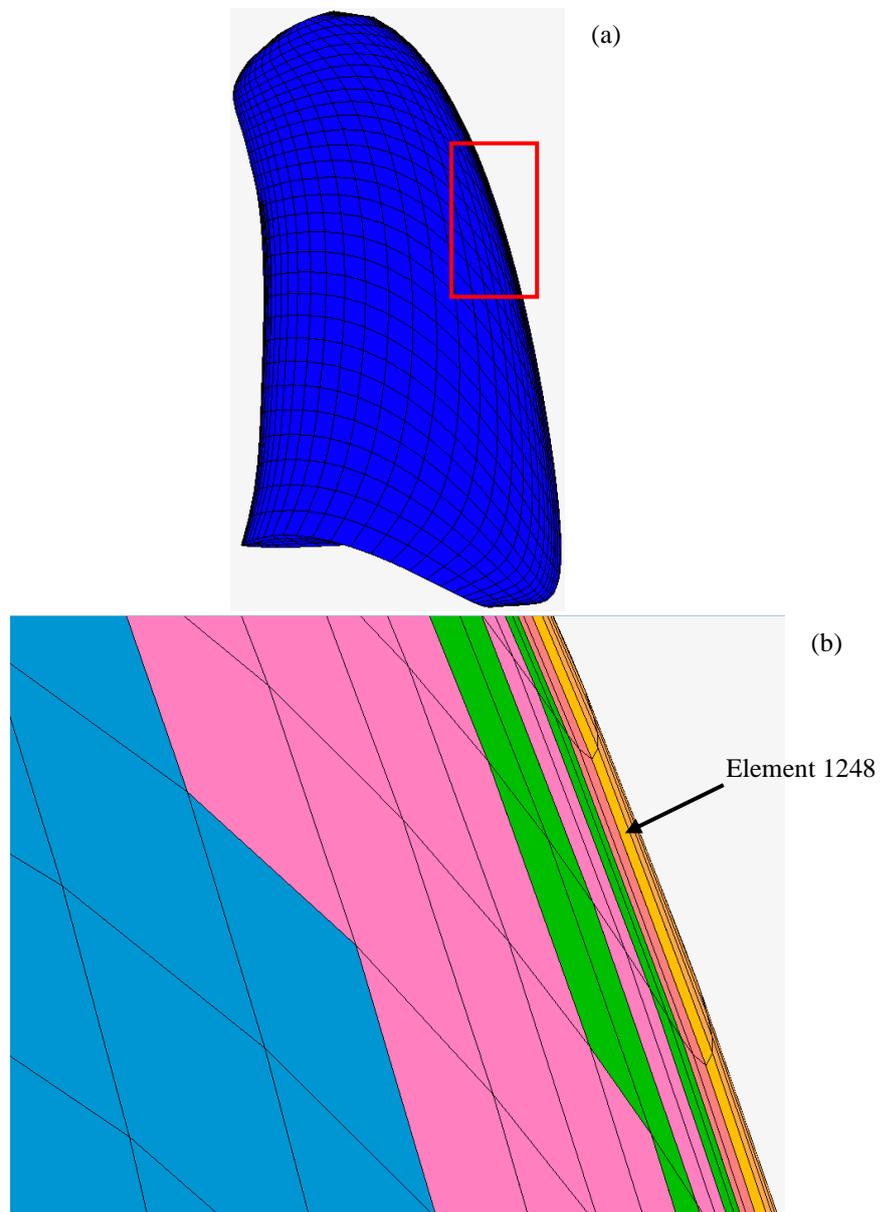
Fig. 2.13: The location of element: (a) global view, and (b) zooming in, and plot in respect of lay-up configuration.

A.2.3: The kth ($k = 1, 2, 3, 4$) largest maximum failure index ($FI_{max,k}^p$) under the load case p.

Load case (p)	$FI_{max,1}^p$	$FI_{max,2}^p$	$FI_{max,3}^p$	$FI_{max,4}^p$
1	0.288	0.171	0.160	0.156
2	0.275	0.163	0.158	0.149
3	0.266	0.158	0.157	0.144
4	0.263	0.157	0.155	0.142
5	0.269	0.157	0.157	0.144
6	0.275	0.162	0.157	0.148
7	0.276	0.163	0.156	0.149
8	0.275	0.162	0.156	0.148
9	0.274	0.162	0.155	0.148
10	0.273	0.161	0.153	0.147
11	0.272	0.160	0.152	0.146
12	0.271	0.160	0.152	0.146
13	0.276	0.163	0.152	0.149
14	0.279	0.165	0.151	0.150
15	0.280	0.165	0.151	0.150
16	0.281	0.166	0.152	0.149
17	0.282	0.167	0.153	0.148
18	0.283	0.168	0.153	0.147
19	0.284	0.168	0.153	0.148
20	0.284	0.168	0.154	0.148
21	0.284	0.168	0.154	0.148
22	0.284	0.168	0.153	0.147
23	0.283	0.168	0.153	0.147
24	0.282	0.167	0.153	0.147
25	0.281	0.166	0.152	0.146
26	0.280	0.166	0.151	0.145
27	0.278	0.165	0.151	0.144
28	0.277	0.164	0.150	0.143
29	0.275	0.163	0.148	0.142
30	0.273	0.161	0.147	0.141
31	0.270	0.160	0.146	0.140
32	0.268	0.159	0.145	0.139
33	0.265	0.157	0.143	0.137
34	0.263	0.156	0.142	0.136
35	0.260	0.154	0.140	0.135
36	0.257	0.152	0.139	0.133
37	0.254	0.151	0.137	0.132
38	0.252	0.149	0.136	0.130

39	0.249	0.147	0.134	0.129
40	0.246	0.146	0.133	0.128
41	0.243	0.144	0.131	0.126
42	0.241	0.142	0.130	0.125
43	0.238	0.141	0.128	0.124
44	0.236	0.140	0.127	0.123
45	0.234	0.139	0.126	0.125
46	0.233	0.138	0.129	0.126
47	0.232	0.137	0.132	0.125
48	0.232	0.138	0.137	0.125
49	0.232	0.143	0.138	0.125
50	0.233	0.149	0.138	0.126
51	0.234	0.155	0.139	0.127
52	0.234	0.161	0.139	0.129
53	0.235	0.167	0.140	0.134
54	0.244	0.172	0.144	0.140
55	0.261	0.175	0.153	0.144
56	0.282	0.176	0.164	0.151
57	0.301	0.176	0.174	0.162
58	0.313	0.185	0.171	0.169
59	0.317	0.188	0.172	0.168
60	0.305	0.181	0.166	0.164

A.2.4: Existence of $FI^p_{max,k}$ at the specific ply number $(ply^p_{max,k})$.

Load case (p)	$ply^p_{max,1}$	$ply^p_{max,2}$	$ply^p_{max,3}$	$ply^p_{max,4}$
1	4	6	3	2
2	4	6	3	2
3	4	6	3	2
4	4	3	6	2
5	4	6	3	2
6	4	6	3	2
7	4	6	3	2
8	4	6	3	2
9	4	6	3	2
10	4	6	3	2
11	4	6	3	2
12	4	6	3	2
13	4	6	3	2
14	4	6	3	2
15	4	6	2	3
16	4	6	2	3
17	4	6	2	3
18	4	6	2	5
19	4	6	2	5
20	4	6	2	5
21	4	6	2	5
22	4	6	2	5
23	4	6	2	5
24	4	6	2	5
25	4	6	2	5
26	4	6	2	5
27	4	6	2	5
28	4	6	2	5
29	4	6	2	5
30	4	6	2	5
31	4	6	2	5
32	4	6	2	5
33	4	6	2	5
34	4	6	2	5
35	4	6	2	5
36	4	6	2	5
37	4	6	2	5
38	4	6	2	5

39	4	6	2	5
40	4	6	2	5
41	4	6	2	5
42	4	6	2	5
43	4	6	2	5
44	4	6	2	5
45	4	6	2	3
46	4	6	3	2
47	4	6	3	2
48	4	3	6	2
49	4	3	6	2
50	4	3	6	2
51	4	3	6	2
52	4	3	6	2
53	4	3	6	2
54	4	3	6	2
55	4	3	6	2
56	4	3	6	2
57	4	6	3	2
58	4	6	3	2
59	4	6	2	3
60	4	6	2	3

A.2.5: Existence of $FI_{max,k}^p$ at the specific element number(s) ($ele_{max,k}^p$).

Load case (p)	$ele_{max,1}^p$	$ele_{max,2}^p$	$ele_{max,3}^p$	$ele_{max,4}^p$
1	1421, 1363	1479, 1421	24	1421, 1363
2	1421, 1363	1421, 1363	24	1421, 1363
3	1421, 1363, 1305	1421, 1363	24	1421, 1363
4	1363, 1305	24	1421, 1363	1421, 1363
5	1363, 1305	1421, 1363	24	1421, 1363
6	1363, 1305	1421, 1363	24	1421, 1363
7	1421, 1363	1421, 1363	24	1421, 1363
8	1363, 1305	1421, 1363	24	1421, 1363
9	1363, 1305	1421, 1363	24	1421, 1363
10	1363, 1305	1421, 1363	24	1421, 1363
11	1363, 1305	1421, 1363	24	1421, 1363
12	1363, 1305	1421, 1363	24	1421, 1363
13	1363, 1305	1421, 1363	24	1421, 1363
14	1363, 1305	1421, 1363	24	1421, 1363
15	1363, 1305	1421, 1363	1421, 1363	24
16	1421, 1363, 1305	1421, 1363	1421, 1363	24
17	1421, 1363	1421, 1363	1421, 1363	24
18	1421, 1363	1421, 1363	1421, 1363	1364, 1306
19	1421, 1363	1421, 1363	1421, 1363	1364, 1306
20	1421, 1363	1421,1363	1421, 1363	1364, 1306
21	1421, 1363	1421, 1363	1421, 1363	1364, 1306
22	1421, 1363	1421, 1363	1421, 1363	1364, 1306
23	1421, 1363	1421, 1363	1421, 1363	1364, 1306
24	1421, 1363	1421, 1363	1421, 1363	1364, 1306
25	1421, 1363	1421, 1363	1421, 1363	1364, 1306
26	1421, 1363	1421, 1363	1421, 1363	1364, 1306
27	1421, 1363	1421, 1363	1421, 1363	1364, 1306
28	1421, 1363	1421, 1363	1421, 1363	1364, 1306
29	1421, 1363	1421, 1363	1421, 1363	1364, 1306
30	1421, 1363	1421, 1363	1421, 1363	1364, 1306
31	1421, 1363	1421, 1363	1421, 1363	1364, 1306
32	1421, 1363	1421, 1363	1421, 1363	1364, 1306
33	1421, 1363	1421, 1363	1421, 1363	1364, 1306
34	1421, 1363	1421, 1363	1421, 1363	1364, 1306
35	1421, 1363	1421, 1363	1421, 1363	1364, 1306
36	1421, 1363	1421, 1363	1421, 1363	1364, 1306
37	1421, 1363	1421, 1363	1421, 1363	1364, 1306
38	1421, 1363	1421, 1363	1421, 1363	1364, 1306

39	1421, 1363	1421, 1363	1421, 1363	1364, 1306
40	1421, 1363	1421, 1363	1421, 1363	1364, 1306
41	1421, 1363	1421, 1363	1421, 1363	1364, 1306
42	1421, 1363	1421, 1363	1421, 1363	1364, 1306
43	1421, 1363	1421, 1363	1421, 1363	1364, 1306
44	1421, 1363	1421, 1363	1421, 1363	1364, 1306
45	1421, 1363	1421, 1363	1421, 1363	24
46	1421, 1363	1421, 1363	24	1421, 1363
47	1421, 1363	1421, 1363	24	1421, 1363
48	1421, 1363	24	1421, 1363	1421, 1363
49	1421, 1363	24	1421, 1363	1421, 1363
50	1421, 1363	24	1421, 1363	1421, 1363
51	1421, 1363	24	1421, 1363	1421, 1363
52	1421, 1363	24	1479, 1421	29
53	1421, 1363	24	1421, 1363	29
54	1363, 1305	24	1421, 1363	29
55	1363, 1305	24	1421, 1363	29
56	1363, 1305	24	1421, 1363	1421, 1363
57	1363, 1305	1421, 1363	24	1421, 1363
58	1363, 1305	1421, 1363	24	1421, 1363
59	1421, 1363	1421, 1363	1421, 1363	24
60	1421, 1363	1479, 1421	1421, 1363	24

A.2.6: Stress and moment resultants of element 1421 under each load case.

Load case (p)	N_1^p [MPa·mm]	N_2^p [MPa·mm]	N_{12}^p [MPa·mm]	M_1^p [MPa·mm²]	M_2^p [MPa·mm²]	M_{12}^p [MPa·mm²]
1	20.8	34.5	-2.4	3.3	-1.4	-1.0
2	19.8	33.0	-2.3	3.1	-1.4	-1.0
3	19.2	32.0	-2.2	3.0	-1.3	-0.9
4	19.0	31.6	-2.2	3.0	-1.3	-0.9
5	19.1	31.8	-2.2	3.0	-1.3	-0.9
6	19.6	32.7	-2.3	3.1	-1.4	-1.0
7	19.9	33.1	-2.3	3.2	-1.4	-1.0
8	19.8	32.9	-2.3	3.1	-1.4	-1.0
9	19.7	32.8	-2.3	3.1	-1.4	-1.0
10	19.6	32.7	-2.3	3.1	-1.4	-1.0
11	19.5	32.4	-2.3	3.1	-1.3	-1.0
12	19.4	32.3	-2.3	3.1	-1.3	-1.0
13	19.8	33.0	-2.3	3.1	-1.4	-1.0
14	20.0	33.3	-2.3	3.2	-1.4	-1.0
15	20.1	33.4	-2.3	3.2	-1.4	-1.0
16	20.2	33.6	-2.4	3.2	-1.4	-1.0
17	20.3	33.8	-2.4	3.2	-1.4	-1.0
18	20.4	33.9	-2.4	3.2	-1.4	-1.0
19	20.4	33.9	-2.4	3.2	-1.4	-1.0
20	20.5	34.0	-2.4	3.2	-1.4	-1.0
21	20.5	34.0	-2.4	3.2	-1.4	-1.0
22	20.4	33.9	-2.4	3.2	-1.4	-1.0
23	20.4	33.9	-2.4	3.2	-1.4	-1.0
24	20.4	33.8	-2.4	3.2	-1.4	-1.0
25	20.3	33.7	-2.4	3.2	-1.4	-1.0
26	20.2	33.6	-2.3	3.2	-1.4	-1.0
27	20.1	33.4	-2.3	3.2	-1.4	-1.0
28	20.0	33.2	-2.3	3.2	-1.4	-1.0
29	19.9	33.0	-2.3	3.2	-1.4	-1.0
30	19.7	32.8	-2.3	3.1	-1.4	-1.0
31	19.6	32.5	-2.3	3.1	-1.4	-1.0
32	19.4	32.2	-2.3	3.1	-1.3	-1.0
33	19.3	32.0	-2.2	3.1	-1.3	-0.9
34	19.1	31.7	-2.2	3.0	-1.3	-0.9
35	18.9	31.4	-2.2	3.0	-1.3	-0.9
36	18.7	31.1	-2.2	3.0	-1.3	-0.9
37	18.5	30.8	-2.2	2.9	-1.3	-0.9

38	18.3	30.5	-2.1	2.9	-1.3	-0.9
39	18.2	30.2	-2.1	2.9	-1.3	-0.9
40	18.0	29.8	-2.1	2.8	-1.2	-0.9
41	17.8	29.5	-2.1	2.8	-1.2	-0.9
42	17.6	29.2	-2.0	2.8	-1.2	-0.9
43	17.4	28.9	-2.0	2.8	-1.2	-0.9
44	17.3	28.7	-2.0	2.7	-1.2	-0.8
45	17.2	28.5	-2.0	2.7	-1.2	-0.8
46	17.1	28.4	-2.0	2.7	-1.2	-0.8
47	17.0	28.3	-2.0	2.7	-1.2	-0.8
48	17.0	28.2	-2.0	2.7	-1.2	-0.8
49	17.0	28.3	-2.0	2.7	-1.2	-0.8
50	17.1	28.4	-2.0	2.7	-1.2	-0.8
51	17.2	28.6	-2.0	2.7	-1.2	-0.8
52	17.2	28.7	-2.0	2.7	-1.2	-0.8
53	17.3	28.8	-2.0	2.7	-1.2	-0.8
54	17.6	29.4	-2.0	2.8	-1.2	-0.9
55	18.5	30.8	-2.1	2.9	-1.3	-0.9
56	19.7	32.8	-2.3	3.1	-1.3	-1.0
57	21.0	35.0	-2.4	3.3	-1.4	-1.0
58	22.0	36.7	-2.6	3.5	-1.5	-1.1
59	22.5	37.5	-2.6	3.6	-1.6	-1.1
60	21.9	36.4	-2.5	3.5	-1.5	-1.1

3

Stiffness and Strength Reduction in Early Fatigue Stages of Composite Marine Propellers

---

3.1.INTRODUCTION

During the past decades, the fibre reinforced composite materials have been considered to manufacture marine propellers. The composite marine propellers overweigh the traditional ones, which generally made of nickel-aluminium-bronze (NAB) or manganese bronze (MB), in the ways of lightening weight, lowering maintenance costs [1], improving cavitation inception speed [2-4], dismissing electro-magnetic signature [5], and particularly enhancing efficiency at off-design conditions [6]. The potential advantages promote researches on the composite marine propeller. First the fluid-structure interaction (FSI) response of the flexible composite propellers has been studied numerically. The various computational methods for coupling structural and fluid models are summarised in [7, 8]. Generally, they have been used, and working together with genetic algorithms, to simulate efficiency gain at off-design conditions [6, 9-13]. Some other optimisation works concerned detaining cavitation [2-4] and improving vibration performance [5]. The experimental studies are important to validate the claimed advantages. However, a fewer number of experiments have been performed, and which are confined to use small dimension propellers [4, 13, 14]. Besides, the flow properties in the experiments are simplified [16, 17]. The other difficulties encountered in experiments include the accuracy of measuring techniques [16, 18, 19] and different measurement outputs [3, 18]. All previous research has revealed the promising future of applying composite marine propellers. Yet more thorough understandings on the mechanical properties of composite marine propellers are required [7, 8]. For example, the fatigue performance of composite marine propeller working in aggressive seawater environment is a crucial topic.

In other application domains and fundamental studies, fatigue of aged FRP composites have been more elaborately investigated. First, aging of composite materials have been studied, for example, when immersed in seawater [20-24], in substitute/artificial/synthetic seawater [25-32], in purified water [31], in deionised water [32], and in distilled water [33, 34], etc. The prevailing conclusion is that the water is mainly absorbed by the matrix, and the voids and poorly bonded fibre/matrix interfaces work as the secondary pathways for moisture diffusion. The fibres seem to absorb negligible amount of water. The experiments performed by Nguyen et al. [31] indicate that only the water, other than salt particles, can be absorbed into the composite material. Generally gravimetric measurements are performed to monitor the mass gain of aging specimens. The procedure of water uptake can be affected by a few parameters: fluid temperature, aging time, matrix type, fibre type and structure, etc. Elevated water temperature, i.e., thermos-aging of composites, promotes moisture diffusion. But the extreme temperature must be constrained below the glass transition temperature of corresponding matrix [21]. Regarding aging time, the mass records of aged composite materials stay at plateau after reaching saturation. However, the aged specimens gain extra mass [22, 24] or further lose mass [25] over an extended period of time. After reaching saturation, the mass loss of aged specimens due to hydrolysis of polyester resin was observed [29]. The different fibre structures also play a role, e.g., chopped fibre mat, stitched fibres, unidirectional fibres in different lay-up configurations, and woven fibres in different patterns (plain weave, twill weave, and satin weave), etc. The various fibre structures alter the moisture diffusion pathways, and therefore affect water uptake. The possible effect of stitching threads was discussed by Boisseau et al. [22]. The aging effect can be affected by fibre type. The water molecules penetrate the interior and

interact with glass fibres. The mechanisms of water-glass chemical reactions and the subsequent stress corrosion effect have long been observed [35-37]. Besides, the different manufacturing methods determine the production quality, and ultimately affect water uptake. Mechanical properties of the aged specimens have been investigated at certain intervals of the aging procedure, and compared with the intact specimens. Reduction of tensile stiffness and strength properties, for example, were presented in [20, 21, 28, 29, 31-34]. Decreasing flexural stiffness and strength properties were investigated via four-point bending tests [20, 30, 32] and three-point bending tests [24, 26-29]. Besides, the degradations of interlaminar shear properties of aged composite laminates were introduced in [20, 21, 26]. Compared to the static tests of aged composites, a limited number of fatigue tests concerning tensile-tensile fatigue performance of aged composites were performed as well [20, 31, 34]. The flexural fatigue properties of aged composites were investigated in [20, 23, 26, 27, 30].

In the first step of this research (Chapter 2), the one most critical hot-spot element at a composite blade model has been determined via finite element analysis. Based on the numerical study result, the experimental investigation on the fatigue performance of the composite marine propeller is continued and presented in this chapter. It is organised as follows: the design of composite specimens and fatigue cyclic loading are explained in section 2. Thereafter, making specimens and evaluating composite qualities are introduced in section 3 and 4, respectively. In section 5, mechanical properties of the unidirectional carbon fibre reinforced plastic material are calculated and compared with the value provided by material data sheet. The experimental plans for 18 non-aged (for convenience of expression, denoted as "dry") specimens and the other 18 aged (for convenience of expression, denoted as "wet") specimens are provided in section 6. The experimental results of dry and wet specimens are presented in section 7 and 8, respectively. Moreover, the effects of fatigue cyclic loading on the stiffness and strength properties of dry and wet specimens are discussed.

3.2. DESIGNING TEST SPECIMENS AND DETERMINING REPRESENTATIVE FATIGUE LOADS

The numerical simulation results have indicated that element 1421 (see Fig. 2.6) is the most critical element in the FE model of the composite marine propeller blade. Therefore, the lay-up configuration (woven/0/-90/-45/-90/0) of this element and stress (N) and moment (M) resultants specific to that element should be used in the tests. The stress and moment resultants were calculated under each load case ($p = 1, 2, ... , 60$) (Appendix A.3.1), and were used to develop the fatigue test loads.

3.2.1. DESIGNING UNIAXIAL CYCLIC LOADING

In view of the stress and moment resultants of the hot-spot element, the ideal way of applying loads would be a combination of multiaxial forces and moments. The approach, however, is to start with simpler tests to isolate failure modes (and subsequently move to more complex element or sub-component tests, but not in the scope of this thesis). Therefore, it was decided to use uniaxial test coupons first with layup and geometry which would locally reproduce most of the multi-directional

aspects (Appendix A.3.1) of the full-scale structure at the location of interest. This was done by rotating the layup of the critical element so that a uniaxial tension or compression load would create a combined state of stress which represents the main stress components of the full-scale propeller at that location. The hot-spot element 1421 is located at the outer skin of the blade model where the failure is dominated by in-plane stresses. Therefore, the simplification of disregarding moment resultants was used in the load designs.

As shown in Fig. 3.1, when a uniaxial force (F_x) is applied at a certain angle (θ) with respect to the $0°$ fibre direction, i.e., direction 2 of the element-dependent (local) coordinate system in the blade model [14], the stress resultants generated from the uniaxial force can be expressed as:

$$N_1^* = N_x (\sin \theta)^2, \tag{3.1}$$

$$N_2^* = N_x (\cos \theta)^2, \tag{3.2}$$

$$N_{12}^* = -N_x \sin \theta \cos \theta, \tag{3.3}$$

where $N_x = \frac{F_x}{b}$, and b denotes the specimen width.

42
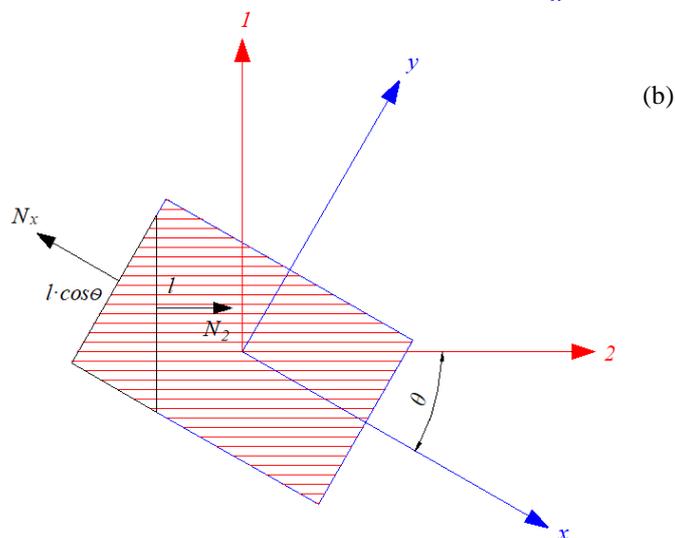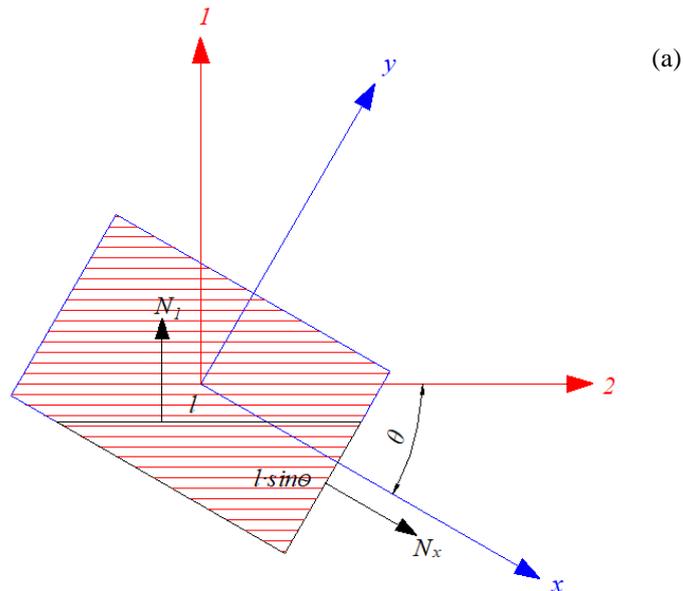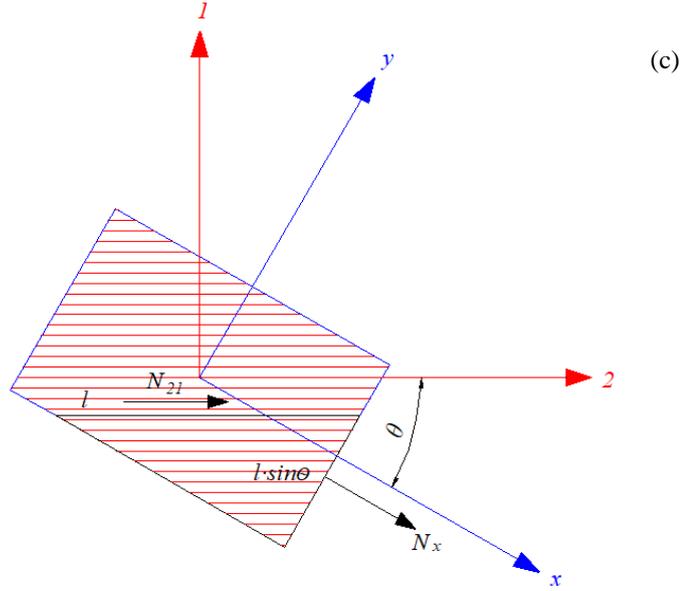
Fig. 3.1: Applying uniaxial force to composite specimens.

For example, considering the hot-spot element 1421 and the corresponding critical load case 59 (Table 2.9), the stress resultants (N_1, N_2 and N_{12}) of the composite element provided by the output of FE analysis are given in Table 3.1. Requiring that N_1^* and N_2^* generated from F_x to be identical with N_1 and N_2, respectively, we can get:

$$\theta = tan^{-1}\left(\sqrt{\frac{N_1}{N_2}}\right), \tag{3.4}$$

$$N_x = \frac{N_1}{(sin\,\theta)^2}. \tag{3.5}$$

Then, N_{12}^* is calculated according to Eq. 3.3 (solution 1 in Table 3.1).

Alternatively (solution 2 in Table 3.1), N_2^* and N_{12}^* are matched to N_2 and N_{12}, respectively. Hence:

$$\theta = tan^{-1}\left(-\frac{N_{12}}{N_2}\right), \tag{3.6}$$

$$N_x = \frac{N_2}{(cos\,\theta)^2}, \tag{3.7}$$

and N_1^* is calculated according to Eq. 3.1.

Comparing the stress resultants in Table 3.1, it can be found that N_1^* of the second solution is much smaller than the required value. It would underestimate the loading effect on the structural performance. On the other hand, the magnitude of N_{12}^* of the first solution is much larger than the magnitude of the required value, which would result in a conservative estimation of the structural behaviour. In the present research, therefore, the first solution has been selected.

Table 3.1: Stress resultants generated from uniaxial force in two load designs.

Stress resultants	FE analysis results (load case 59)	Load design: solution 1	Load design: solution 2
N_x [MPa·mm]	N/A	60.0	37.7
θ [°]	N/A	38	4
N_1 (N_1^*) [MPa·mm]	22.5	22.5	0.2
N_2 (N_2^*) [MPa·mm]	37.5	37.5	37.5
N_{12} (N_{12}^*) [MPa·mm]	-2.6	-29.1	-2.6

The first approach, i.e., Eqs. 3.4 and 3.5, has been applied to the other load cases. The calculation results of N_x and θ are listed in Appendix A.3.2. They show that the maximum N_x is 60 MPa·mm under load case 59, and the minimum N_x is 45.2 MPa·mm under load case 48. Besides, θ remains constant at 38° under each load case. The uniaxial force is therefore applied at 38° with respect to the 0° fibre direction.

3.2.2. TEST SPECIMEN DESIGN

Because N_x is always positive under each load case, the in-plane dimensions of the specimens (Table 3.2) have been designed according to the ASTM D3039 standard [38]. The lay-up configuration of the specimens is (in principle) a duplicate of the hot-spot element. However, the woven ply has been left out of account because the woven CFRP material was not available. It is expected that not using a woven ply would result in slightly more conservative results. Quantification of the exact effect of the woven ply is however to be further investigated.

Table 3.2: The specimen dimensions and lay-up configuration.

Length (a) [mm]	Width (b) [mm]	Lay-up configuration
250	25	0/-90/-45/-90/0

The first set of tests are constant amplitude tests. The maximum and minimum uniaxial forces (Table 3.3) are calculated by $F_x = N_x b$, where b is the specimen width. The load ratio (R) is therefore determined.

Table 3.3: The fatigue cyclic loading.

Minimum load ($F_{x,min}$) [kN]	Maximum load ($F_{x,max}$) [kN]	Load ratio (R)
1.13	1.5	0.75

3.3. MANUFACTURING OF SPECIMENS

The unidirectional (UD) carbon fibre (HexTow® IM7, 12K filament count tows, fibre areal weight of 134 g/m²) reinforced epoxy (HexPly® 8552, resin ratio of 33%) composite material was used to

manufacture the specimens. First a laminated composite plate of 675×675 mm was fabricated using hand lay-up (Fig. 3.2). The UD plies were laid up in the required orientations and stacking sequence. Because the width of the raw material sheet is 300 mm, each ply composed of several material patches. The composition of the patches is schematically explained in Appendix A.3.3. The resulting laminates were cured in an autoclave (Fig. 3.3), following the cure cycle recommended by the material supplier (Fig. 3.4).

Fig. 3.2: Making composite plate by hand lay-up method.
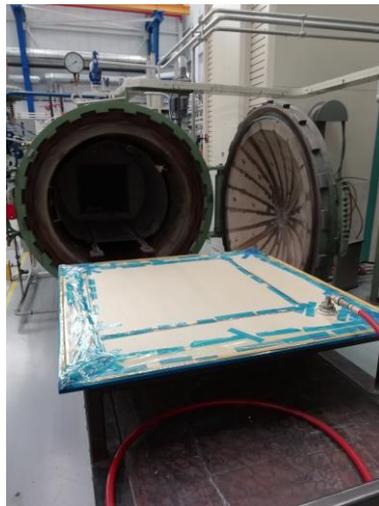
Fig. 3.3: Curing composite plate in autoclave.
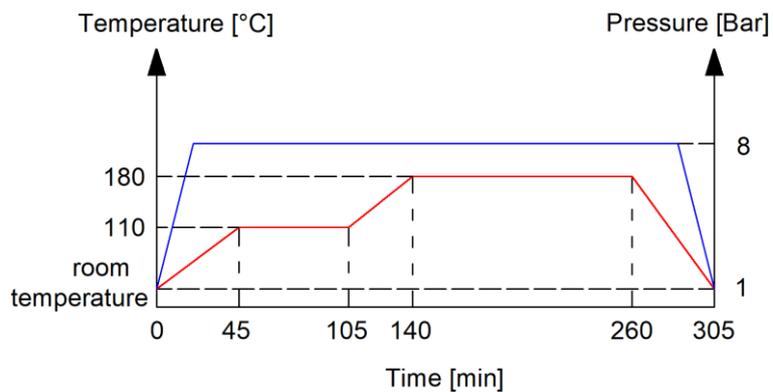
Fig. 3.4: Temperature and pressure control in the autoclave.

To comply with the requirement that the load would be applied at 38º to the fibres in the 0º direction, the composite plate was cut at 38º with respect to the fibre direction in 0º ply. A blade saw was used (Fig. 3.5). A schematic explanation of the cutting process is given in Appendix A.3.4. After thorough visual inspection, a total of 36 specimens without any obvious manufacturing defects were selected for the tests.
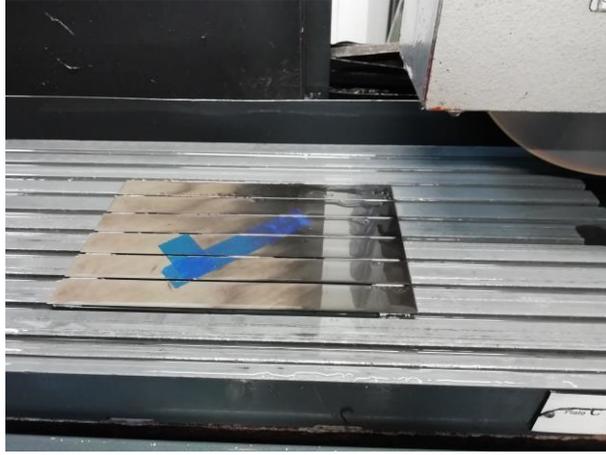
Fig. 3.5: Cutting composite plate to specimens, where the two blue tapes denote 0 and 90º fibre directions.

3.4. EVALUATING THE PHYSICAL PROPERTIES

In addition, the quality of the composite plate in terms of fibre volume fraction and void content ratio were investigated.

3.4.1. FIBRE VOLUME FRACTION

Because the composite density can be defined as a function of the density of individual constituents and the fibre volume fraction [39]:

$$\rho_c = V_f \rho_f + (1 - V_f)\rho_m, \tag{3.8}$$

where ρ_c, ρ_f and ρ_m denote the density of the composite material, the reinforcement and the matrix, respectively, and V_f is the fibre volume fraction. This equation can be converted to:

$$V_f = \frac{\rho_c - \rho_m}{\rho_f - \rho_m}. \tag{3.9}$$

ρ_f and ρ_m are provided by the HEXCEL® product data sheets: 1.77 and 1.30 g/cm³, respectively [40]. While the composite density was measured via experiment. Three smaller specimens with the approximate dimensions of 15×30 mm were cut from the composite plate. They were weighed in air (m_0) and distilled water (m_1) using the density kit and a laboratory balance (Fig. 3.6). The composite density was then calculated by:

$$\rho_c = \frac{m_0}{m_0 - m_1}(\rho_t - \rho_r) + \rho_r. \tag{3.10}$$

Due to the high-accuracy requirement on calculating composite density, the air buoyancy correction was considered via the parameter of air density (ρ_r, taken as 0.0012 g/cm³). Besides, the in-situ density

of the distilled water (ρ_t) at 21.5°C was 0.99791 g/cm³. The weight records of the three specimens, as well as the calculation results of ρ_c and V_f, are given in Table 3.4. The mean fibre volume fraction for the three specimens cut out from the panel turned out to be 62.0%. This is higher than the nominal value of 57.7% given in the product data sheet [40].

Fig. 3.6: Weighing specimens in air and in water.

Table 3.4: Calculating composite density and fibre volume fraction.

Specimen No.	m_0 [mg]	m_1 [mg]	ρ_c [g/cm3]	V_f [%]
1	646.8	242.0	1.5938	62.5
2	520.1	193.4	1.5879	61.3
3	512.6	191.6	1.5928	62.3
			Mean:	62.0

3.4.2. VOID CONTENT RATIO

As explained in the introduction section, it is generally acknowledged that the voids in the composite material are the main water absorbing path. Therefore, the void content of the composite plate was evaluated according to the ASTM D3171 standard [41]. First the three specimens were weighed together with desiccated crucibles (m_{c0}). They were heated in a furnace (Fig. 3.7), and the temperature control is explained in Fig. 3.8. The epoxy resin was burnt off during this procedure. The fibres were left (Fig. 3.9) and were weighed with the crucibles (m_{cf}) after cooling down. The void content ratio was calculated by:

$$V_v = 1 - (V_f + V_m),\tag{3.11}$$

where V_f and V_m are the fibre and matrix volume fraction, respectively. They were calculated by:

$$V_f = \frac{[m_{cf} - (m_{c0} - m_0)]/\rho_f}{m_0/\rho_c},\tag{3.12}$$

$$V_m = \frac{(m_{c0} - m_{cf})/\rho_m}{m_0/\rho_c}.\tag{3.13}$$

The weight records and the calculation results of V_v are given in Table 3.5. For all three specimens the void content was negative. This is due to inaccuracies in the calculation method but clearly suggests that the actual void content was very low.

Table 3.5: Calculating void content ratio.

Specimen No.	m_{c0} [mg]	m_{cf} [mg]	V_v [%]
1	8779.8	8133.5	-22.6
2	8707.4	8188.2	-22.1
3	8320.4	7808.5	-22.5

Fig. 3.7: Heating specimens in muffle furnace.
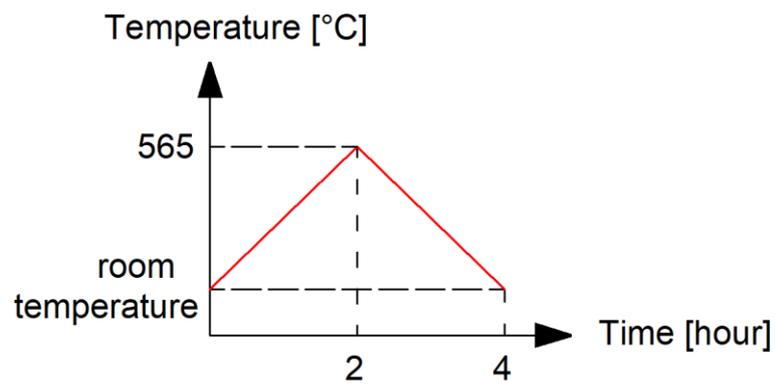
Fig. 3.8: Temperature control in the muffle furnace.

Fig. 3.9: The fibres were left behind in crucibles after heating.

3.5. CALCULATING THE MECHANICAL PROPERTIES

The experimental investigation has shown that the fibre volume fraction of the composite plate is 4.3% higher than the nominal value given in product data sheet. Therefore, the mechanical properties of the UD CFRP material were updated accordingly.

The nominal stiffness properties, including the Young's moduli in longitudinal (E_L) and transverse (E_T) directions, are given in Table 3.6. According to the rule of mixtures [39]:

$$E_L = E_f V_f + E_m V_m, \tag{3.14}$$

$$\frac{1}{E_T} = \frac{1}{E_f} V_f + \frac{1}{E_m} V_m. \tag{3.15}$$

E_L is a weighted average of the stiffness of fibre (E_f) and matrix (E_m), and $\frac{1}{E_T}$ is a weighted average of the compliance of the individual constituents. Because the nominal fibre volume fraction is 57.7%, and the void content ratio is very small, the nominal matrix volume fraction can be calculated simply by:

$$V_m = 1 - V_f. \tag{3.16}$$

Therefore, E_f and E_m can be estimated by solving Eqs. 3.14 and 3.15.

With the fibre volume fraction of about 62.0%, the Young's moduli (Table 3.6) in longitudinal and transverse directions were estimated from Eqs. 3.14 to 3.16. As can be seen from Table 3.6, the estimated stiffness properties using the actual fibre volume fraction are higher than those reported by the material supplier for a lower fibre volume fraction. Besides, the shear modulus (G_{LT}) and Poisson's ratio (ν_{LT}) are included in Table 3.6.

Table 3.6: Comparing nominal and actual material properties.

Material physical and mechanical properties	Nominal	Actual
Fibre volume fraction (V_f)	57.7	62.0

[%]		
Matrix volume fraction (V_m)	42.3	38.0
[%]		
Fibre stiffness (E_f)	280.4	
[GPa]		
Matrix stiffness (E_m)	7.0	
[GPa]		
Composite stiffness in longitudinal direction (E_L)	164	176.5
[GPa]		
Composite stiffness in transverse direction (E_T)	12	17.7
[GPa]		
Shear modulus (G_{LT})	4.9	
[GPa]		
Poisson's ratio (ν_{LT})	0.29	

3.6. DESIGNING THE EXPERIMENTS

Under pre-defined cyclic loading, the fatigue lifetime of composite specimens can be quantified by cyclic loading up to failure. However, the final failure is not the adequate criterion for designing composite components and structures. Generally, the accumulation of fatigue damage can be signified by the loss of functionality, e.g., the residual stiffness or strength [42]. Therefore, the effect of fatigue loads on the (residual) stiffness and strength properties of composite specimens is investigated experimentally. Moreover, the combined effect of fatigue loads and seawater environment is investigated by using the aged specimens.

3.6.1. EFFECT OF FATIGUE LOADS

Eighteen out of the 36 specimens were tested to investigate the effect of designed fatigue loads on the material stiffness and strength properties. According to the design, 4 intact specimens were loaded up to failure to determine the ultimate tensile strength ($\sigma_{ult,0}$), and around 10% of the mean failure load ($\overline{F_{ult,0}}$) was applied to the other 14 intact specimens to determine their stiffness (E_0). The defined cyclic loading was applied to the 14 surviving specimens. After 10^4 (N_1) cycles of fatigue loads, 4 specimens were tested quasi-statically to failure, and the failure load ($F_{ult}(N_1)$) and strength ($\sigma_{ult}(N_1)$) were determined. Around 10% of the mean failure load ($\overline{F_{ult}(N_1)}$) was applied to the other 10 specimens to determine their stiffness ($E(N_1)$). The fatigue tests continued with the last 10 specimens. After 10^6 (N_2) cycles of fatigue loads, the failure load ($F_{ult}(N_2)$) and strength ($\sigma_{ult}(N_2)$), and the stiffness ($E(N_2)$) were determined in the same way using 4 and 6 of the remaining specimens, respectively.

3.6.2. COMBINED EFFECTS OF CYCLIC LOADING AND SEAWATER ENVIRONMENT

The other 18 specimens were aged by immersing in the salt water of 5% salinity for up to 60 days. The specimens and the container were kept in a water spray system, which was spraying the same salt water (Fig. 3.10). The water temperature was heated to and maintained at 35 ℃. The humidity in the water spray system was kept at 50%. To evaluate the progress of water absorbing, the specimen weight was measured at scheduled intervals. When the 18 specimens reached saturation, they were tested in the same procedure as the non-aged specimens.
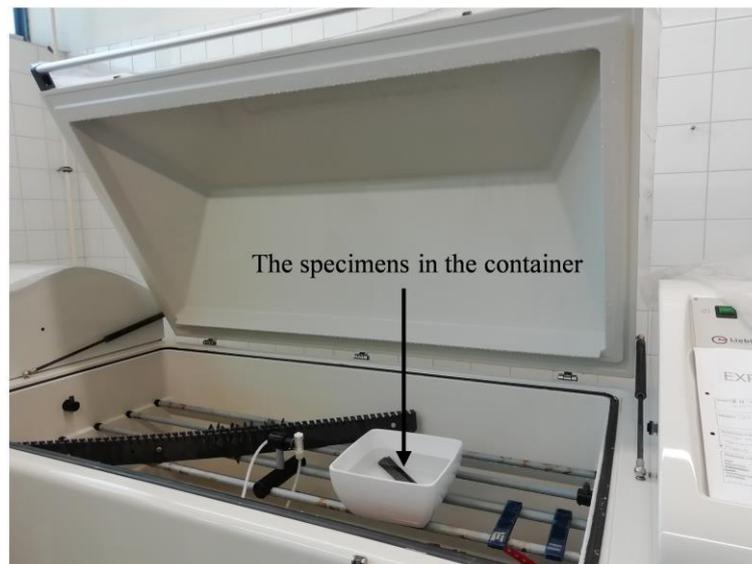
Fig. 3.10: Aging composite specimens in water spray system.

3.7. EXPERIMENT OF DRY CFRP SPECIMENS

3.7.1. OVERVIEW OF TESTS

The effect of fatigue cyclic loading on the mechanical properties of dry CFRP specimens was investigated experimentally. According to the aforementioned experiment design, first the stiffness and strength properties of the intact specimens were measured. Then the specimens were subjected to the uniaxial constant amplitude fatigue loads. The stiffness and strength properties were measured again after 10^4 (N_1) and 10^6 (N_2) cycles of fatigue loads. As given in Table 3.3, the cyclic loading varies from the minimum value of 1.13 kN to the maximum value of 1.5 kN. Therefore, the load ratio (R) is 0.75. In order to avoid the self-heating effect, which has been proved to degrade the properties of composite materials and structures [42-49], the loading frequency (f) was set to 5 Hz. Considering the fatigue load range in Table 3.3, an MTS fatigue testing machine which can apply force up to 10 kN was employed for the fatigue tests.

An overview of the tests with dry specimens is provided in Table 3.7. The different types of tests include the quasi-static failure test, the stiffness test (not using/using extensometer), and the fatigue test. A schematic explanation of the uniaxial force with respect to fibre directions in each ply of the

composite specimens is given in Fig. 3.11. According to load design and specimen design described in section 2, the uniaxial force should be applied at 38º with respect to the 0º fibre direction.
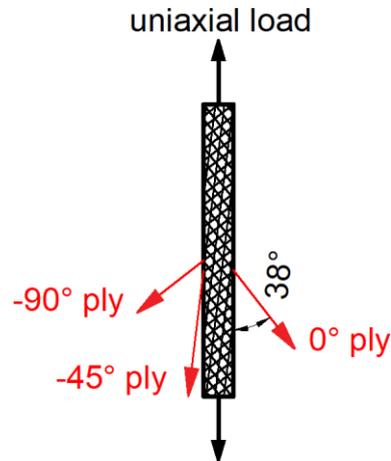
Fig. 3.11: Applying uniaxial load to CFRP specimens.

The experimental records of the quasi-static failure tests and the stiffness tests are plotted in Figs. 3.12 to 3.14. The failure tests of the intact specimens (No. 1 to 4) and of the specimens (No. 15 to 18) after applying 10^6 cycles of fatigue loads were carried out using a Zwick 10kN static testing machine. The displacement-controlled loading was applied to the specimens, and the constant loading head speed was 1 mm/min. Because the intact specimens (No. 1 to 4) were not protected using tabs, slippage happened when the tensile load increased to 4 kN, and premature failure happened afterwards. The ultimate tensile failure loads of the intact specimens (No. 1 to 4) were therefore seriously underestimated. All the other specimens were protected using tabs in this research. The tabs were made of thick paper (160 g/m^2), which has proved to work well in previous applications. The failure tests of the specimens (No. 6 to 9) after applying 10^4 cycles of fatigue loads were carried out using a Zwick 20kN static testing machine, and the displacement-controlled loading with the same loading head speed was applied to the specimens. The 10kN and 20kN static testing machine has hydraulic grips (Fig. 3.15(a)) and wedge grips (Fig. 3.15(b)), respectively. When using wedge grips, the slipping happened in the beginning of tests. Therefore, the experimental records in Fig. 3.12 have shown different patterns at small loads.

The stiffness tests have been performed first using a Zwick 10kN static testing machine. For each group of specimens, i.e., the intact specimens (No. 5 to 18), the specimens (No. 10 to 18) after applying 10^4 cycles of fatigue loads, and the specimens (No. 10 to 14) after applying 10^6 cycles of fatigue loads, one specimen was tested with the maximum load of 1 kN, and the others were tested with the maximum load of 800 N. The calculation of tensile strain based on the displacement record of loading head turns out to be inaccurate, and it will be explained in detail later.

In the end, the five survived specimens (No. 10 to 14) were tested using a Zwick 250kN static testing machine, where an extensometer was employed to measure strain at gauge section of each specimen during the loading procedure. The hydraulic grips (Fig. 3.15(c)) were used in this machine. In order to accurately capture the elongation between two clips of the extensometer, the constant loading head

speed was set as 0.5 mm/min for these tests. The experimental records of stiffness tests using an extensometer to measure strain are plotted in Fig. 3.14.
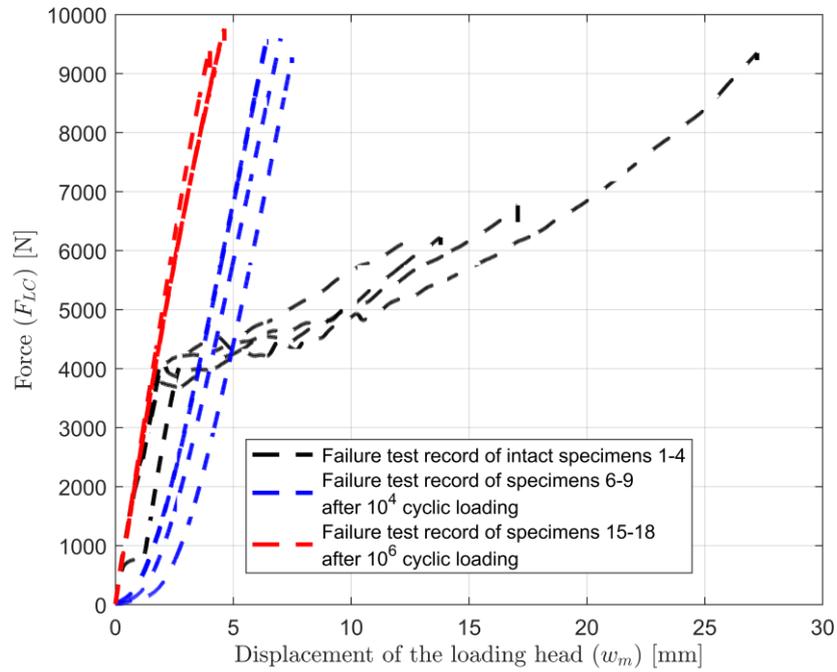
Fig. 3.12: Experimental records of quasi-static failure tests (note that for intact specimens 1-4, slippage happened at tensile load of 4 kN).
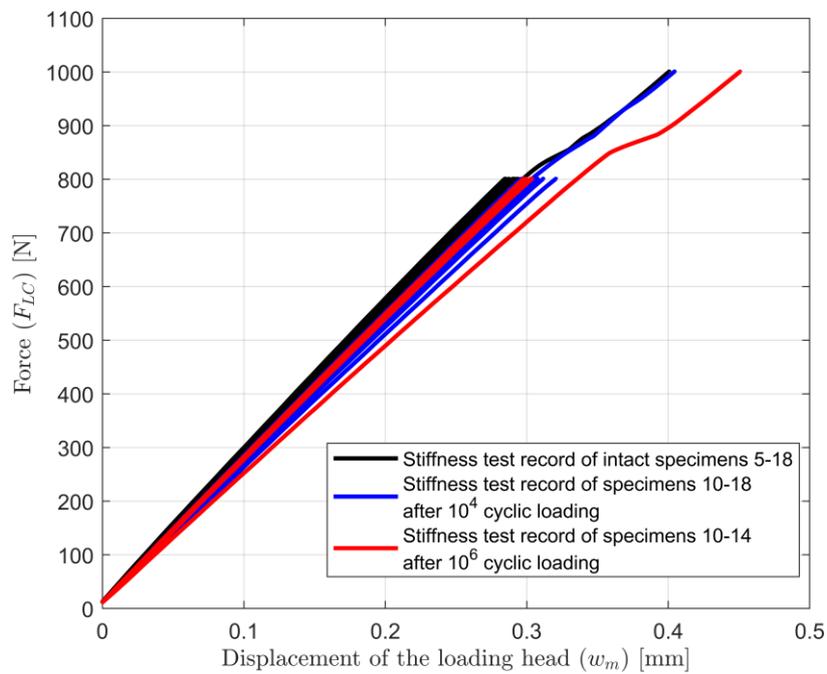
Fig. 3.13: Experimental records of stiffness tests.

53
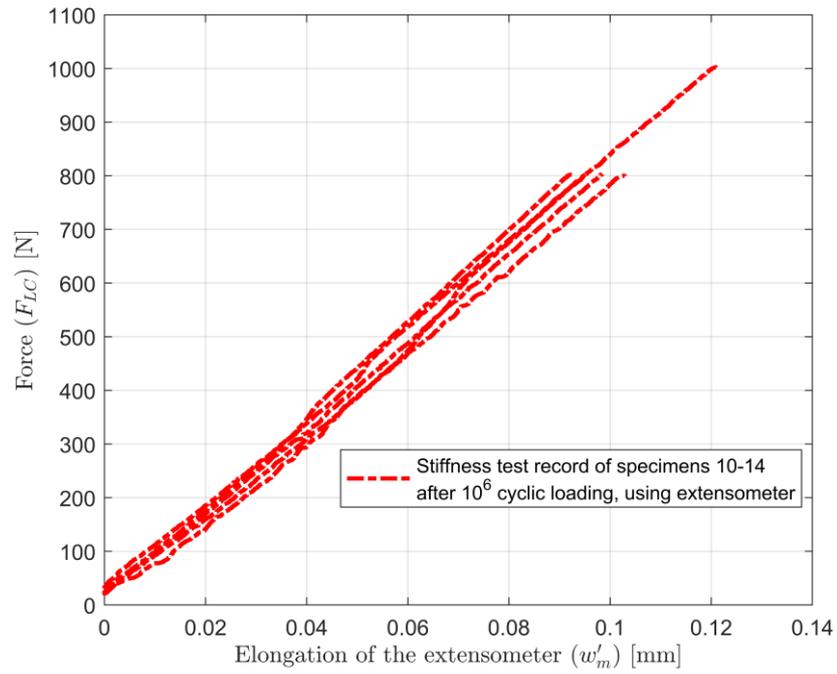
Fig. 3.14: Experimental records of stiffness tests using extensometer to measure strain.

(a)

(b)
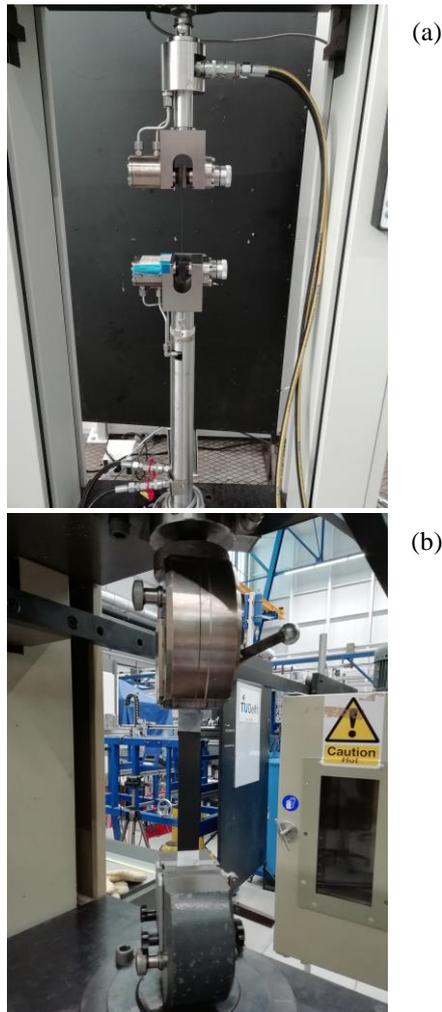
(c)

Fig. 3.15: The 10kN, 20kN and 250kN testing machine has (a) hydraulic grips, (b) wedge grips, and (c) hydraulic grips, respectively.

Table 3.7: Overview of the tests with dry specimens.

Specimen No.	Step 1	Step 2	Step 3	Step 4	Step 5	Step 6
1	F	N/A	N/A	N/A	N/A	N/A
2	F	N/A	N/A	N/A	N/A	N/A
3	F	N/A	N/A	N/A	N/A	N/A
4	F	N/A	N/A	N/A	N/A	N/A
5	S	X	N/A	N/A	N/A	N/A
6	S	10^4 C	F	N/A	N/A	N/A
7	S	10^4 C	F	N/A	N/A	N/A
8	S	10^4 C	F	N/A	N/A	N/A
9	S	10^4 C	F	N/A	N/A	N/A
10	S	10^4 C	S	10^6 C	S	Se
11	S	10^4 C	S	10^6 C	S	Se
12	S	10^4 C	S	10^6 C	S	Se
13	S	10^4 C	S	10^6 C	S	Se
14	S	10^4 C	S	10^6 C	S	Se
15	S	10^4 C	S	10^6 C	F	N/A
16	S	10^4 C	S	10^6 C	F	N/A
17	S	10^4 C	S	10^6 C	F	N/A
18	S	10^4 C	S	10^6 C	F	N/A

F: quasi-static failure test.

S: stiffness test.

C: fatigue test with defined cyclic loading.

Se: stiffness test, using extensometer to measure strain.

X: Specimen 5 was destroyed due to wrong setup in the fatigue testing machine.

Table 3.8: Experimental results of ultimate tensile failure tests with dry specimens.

Specimen No.	Loading history	Ultimate tensile failure load (F_{ult}) [N]	Ultimate tensile strength (σ_{ult}) [MPa]	Mean tensile strength ($\overline{\sigma_{ult}}$) [MPa]	Standard deviation [MPa]
1		6126.2	382.9		
2	F	6223.8	389.0	N/A	N/A
3		6768.7	423.0		
4		9348.6	584.3		
6		9273.7	579.6		
7	S, 10^4C, F	9596.2	599.8	594.7	10.0
8		9602.3	600.1		
9		9586.2	599.1		
15		9761.6	610.1	590.7	18.5

16	S, 10^4C, S, 10^6C, F	9531.9	595.7
17		9053.3	565.8
18		9459.3	591.2

3.7.2. EFFECT OF FATIGUE LOADS ON SPECIMEN STRENGTH

The ultimate tensile failure loads (F_{ult}) of the intact specimens (No. 1 to 4), the specimens (No. 6 to 9) after applying 10^4 cycles of fatigue loads, and the specimens (No. 15 to 18) after applying 10^6 of fatigue loads are listed in Table 3.8. The ultimate tensile strength (σ_{ult}) was therefore calculated by:

$$\sigma_{ult} = \frac{F_{ult}}{b \cdot h}, \tag{3.17}$$

where b and h denote the specimen width and thickness. According to the specimen design, the specimen width is 25 mm (Table 3.2). The average of measured specimen thickness (0.64 mm) is taken as h in the calculations.

Because the intact specimens (No. 1 to 4) were not protected using tabs, the premature failure has happened when the tensile load was above 4 kN (Fig. 3.12). The ultimate failure generally happened at the area close to the upper fixed grip (Fig. 3.16), leading to small failure load. Meanwhile, specimen No. 4 has failed at the area close to the upper fixed grip as well as the gauge area. Therefore, the failure load and strength of specimen No. 4 are much higher than the other three specimens.
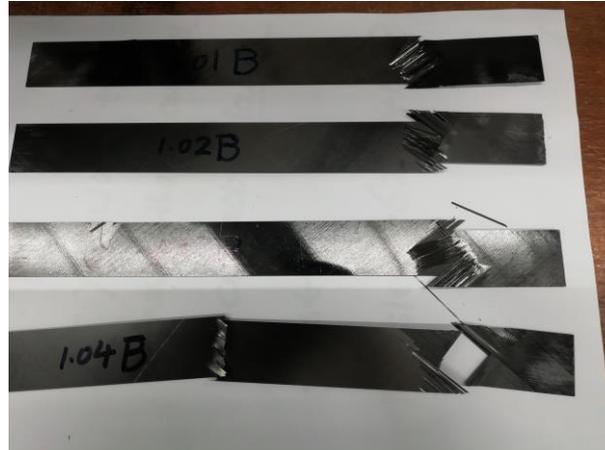
Fig. 3.16: Ultimate tensile failure tests of intact specimens No. 1 to 4 (from top to bottom).

The ultimate tensile strengths of the specimens (No. 6 to 9) after applying 10^4 cycles of fatigue loads, and the specimens (No. 15 to 18) after applying 10^6 cycles of fatigue loads were calculated in the same way. As shown in Table 3.8, the mean tensile strength ($\overline{\sigma_{ult}}$) has decreased from 594.7 to 590.7 MPa with increasing cycles of fatigue loads. While the standard deviation increased from 10.0 to 18.5 MPa. Therefore, it is hard to conclude the effect of fatigue cyclic loading on specimen strength based on the current experimental results. Because these specimens were protected using tabs, it has been observed that the failures were located at gauge areas (Figs. 3.17 and 3.18). As shown in Fig. 3.17, the failure modes include fibre rupture in the -45° ply, matrix cracking in the 0 and -90° plies. Besides, there is fibre-matrix disbond (pull-out) because the fibre fuzzes are observed at the failure positions.
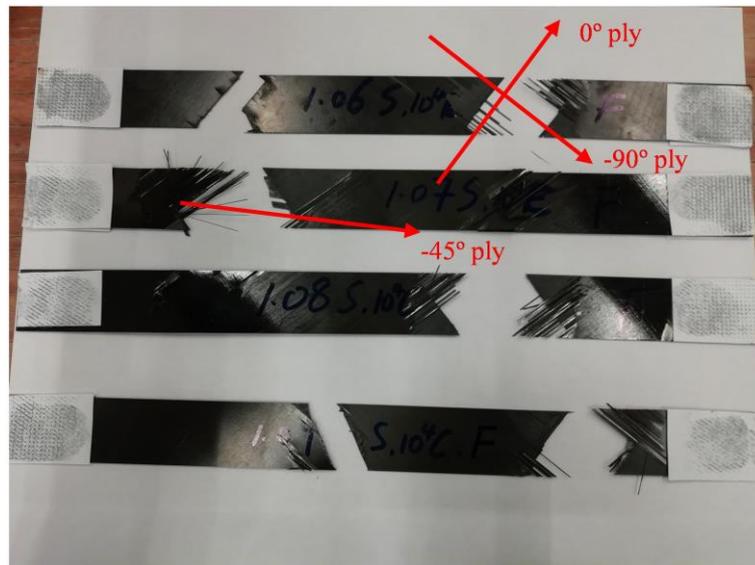
Fig. 3.17: Ultimate tensile failure tests of specimens No. 6 to 9 (from top to bottom).

(a)

(b)

(c)

(d)
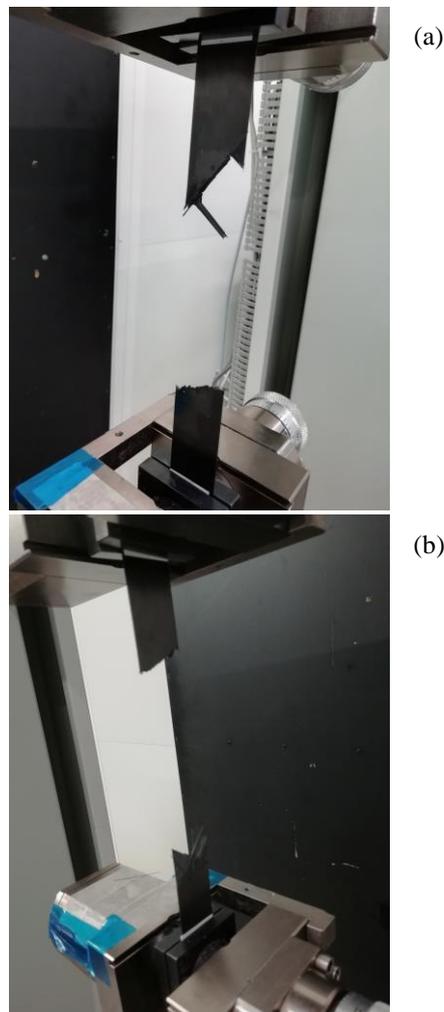
Fig. 3.18: Ultimate tensile failure tests of specimens No. 15 to 18 (from (a) to (d)).

3.7.3. EFFECT OF FATIGUE LOADS ON SPECIMEN STIFFNESS

3.7.3.1. OVERALL STIFFNESS

For the stiffness tests (without using extensometer) of intact specimens (No. 5 to 18), the tensile force (F_{LC}) is plotted as a function of the displacement of loading head (w_m) in Fig. 3.13. They were converted to stress and strain via:

$$\sigma = \frac{F'_{LC}}{b \cdot h}, \tag{3.18}$$

$$\varepsilon = \frac{w_m}{a}, \tag{3.19}$$

where the initial distance between two grips (a) varied from one to another stiffness test. Therefore, the setup of initial distance between two grips in each stiffness test is listed in Table 3.9. Moreover, F'_{LC} is the fitting result of F_{LC} using linear regression model. The first five data points in each load-displacement record were considered as noisy data, and filtered before processing the linear fitting of F_{LC}. Starting from the 6th data points, every 10 (6th to 15th), 20 (6th to 25th), 30 (6th to 35th), …… data points were linearly fitted and converted to stress-strain relations. Thereafter, the specimen stiffness was calculated by:

$$E_x = \frac{\Delta\sigma}{\Delta\varepsilon}, \tag{3.20}$$

where the stiffness was defined as the slope of stress-strain curve. Taking intact specimen No. 5 as an example, the calculation results of specimen stiffness (E_x) is plotted as a function of the number of raw data points (n) in Fig. 3.19.

In order to capture the actual stiffness, the coefficient of determination (R^2) was employed to evaluate the linear fitting result (F'_{LC}). The coefficient of determination is a statistical concept which measures the goodness of fit [50]. The larger the coefficient is, the smaller difference between dependent (F'_{LC}) and independent (F_{LC}) variables. For the intact specimen No. 5, the coefficient of determination is plotted as a function of the number of raw data points (n) in Fig. 3.20. It can be seen that the goodness of fit worsens quickly when $n > 600$. The largest coefficient appears at $n = 30$, i.e., the optimal range (n_{opt}) of raw data points for linear fitting is 6th to 35th. Therefore, the stiffness calculation result at $n = 30$ was picked for the intact specimen No. 5.

For the intact specimens (No. 5 to 18), the specimens (No. 10 to 18) after applying 10^4 cycles of fatigue loads, and the specimens (No. 10 to 14) after applying 10^6 cycles of fatigue loads, the same method has been used in stiffness calculation. Along with the corresponding optimal range of raw data points, the stiffness calculations results are given in Tables 3.10 to 3.12. The mean stiffness has decreased from 28.14 to 25.71 and 25.6 GPa with increasing cycles of fatigue loads. While the standard deviation increased from 0.43 to 0.65 and 1.3 GPa.

In Fig. 3.19 the stiffness calculation results have shown a decreasing trend with the increasing number of raw data points, particularly when $n > 600$. A plausible explanation could be the specimen slippage happened in the grips during loading procedure. As shown in Fig. 3.21, the slipping could result in larger displacement record for the same increment of force. The slope of the load-displacement curve and the stress-strain curve, i.e., the stiffness calculation result, would decrease accordingly. Besides, the possible displacements of grips and testing machine could have similar consequence as the slippage.
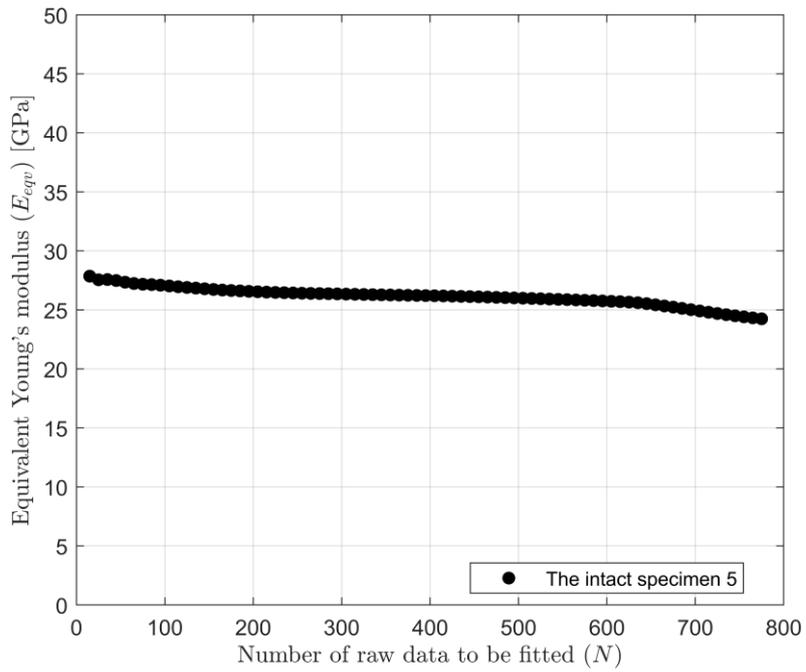
Fig. 3.19: Plotting specimen stiffness as a function of the number of raw data points (intact
specimen No. 5).
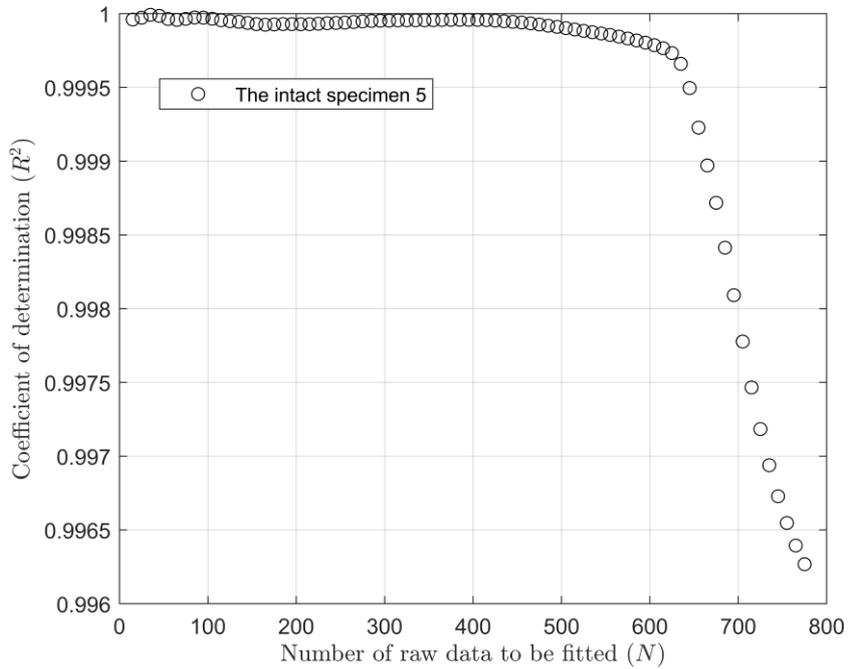
Fig. 3.20: Plotting coefficient of determination as a function of the number of raw data points
(intact specimen No. 5).

61
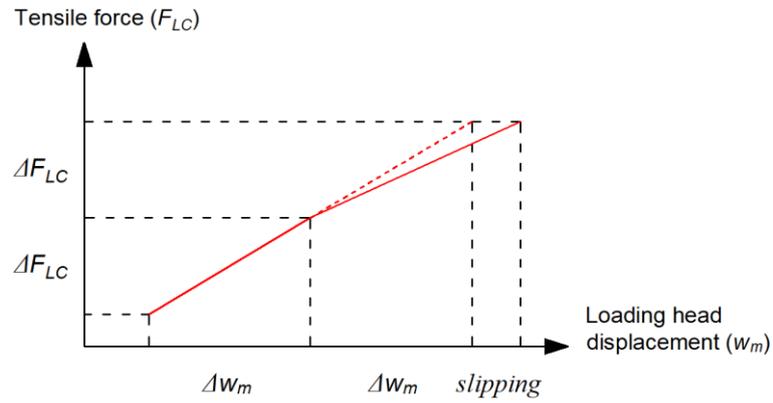
Fig. 3.21: Decreasing stiffness calculation result due to specimen slippage.

Table 3.9: Initial distance between two grips in the stiffness tests.

Specimen No.	Step 1	Step 3	Step 5
1	155	N/A	N/A
2	155	N/A	N/A
3	155	N/A	N/A
4	155	N/A	N/A
5	155	N/A	N/A
6	155	N/A	N/A
7	155	N/A	N/A
8	155	N/A	N/A
9	155	N/A	N/A
10	155	190	185
11	155	185	185
12	155	185	185
13	155	185	185
14	155	185	185
15	155	185	N/A
16	155	185	N/A
17	155	185	N/A
18	155	185	N/A

Table 3.10: The stiffness calculation results for the intact specimens (No. 5 to 18).

Specimen No.	n_{opt}	E_x [GPa]
5	6-35	27.57
6	6-65	27.65
7	6-45	28.17
8	6-35	27.92
9	6-55	28.34
10	6-55	27.86
11	6-45	28.79

12	6-35	28.88
13	6-25	28.8
14	6-55	27.94
15	6-65	27.89
16	6-65	28.29
17	6-35	28.12
18	6-55	27.7
	Mean:	28.14
	Standard deviation:	0.43

Table 3.11: The stiffness calculation results for the specimens (No. 10 to 18) after applying 10^4 cycles of fatigue loads.

Specimen No.	n_{opt}	E_x [GPa]
10	6-205	25.8
11	6-125	26.71
12	6-65	25.53
13	6-235	24.48
14	6-85	25.98
15	6-345	25.58
16	6-25	26.47
17	6-325	25.45
18	6-375	25.4
	Mean:	25.71
	Standard deviation:	0.65

Table 3.12: The stiffness calculation results for the specimens (No. 10 to 14) after applying 10^6 cycles of fatigue loads.

Specimen No.	n_{opt}	E_x [GPa]
10	6-295	23.36
11	6-105	26.67
12	6-345	25.71
13	6-295	26.26
14	6-135	25.99
	Mean:	25.6
	Standard deviation:	1.3

3.7.3.2. SPECIMEN EQUIVALENT STIFFNESS

During the loading process, the displacement record (w_m) consists of more than the tensile deformation of a composite specimen, but also the possible deflections of the grips and other parts of the testing machine. Therefore, the stiffness calculation result (E_x) is considered as the hybrid stiffness of

composite specimen and testing machine. In order to calculate the neat stiffness of composite specimen and estimate the approximate stiffness of testing machine, the stiffness tests were performed with specimens No. 10 to 14, and using an extensometer to measure the strain directly (Fig. 3.22). As shown in Fig. 3.14, the load record (F_{LC}) is plotted as a function of the elongation of extensometer (w'_m). Then the stress and strain were calculated by:

$$\sigma = \frac{F'_{LC}}{b \cdot h},$$ (3.21)

$$\varepsilon = \frac{w'_m}{100},$$ (3.22)

where the initial distance between two clips of the extensometer was always 100 mm. The noisy data in the beginning of each experimental record were identified and filtered. Afterwards the linear fitting of F_{LC} provided F'_{LC}. The specimen equivalent stiffness (E_{eqv}) was defined as the slope of the stress-strain curve. The stiffness of specimens No. 10 to 14 are given in Table 3.13, in which the stiffness calculation results (E_x) are included as well. Apparently, the value of E_{eqv} is generally twice the corresponding E_x.

The stiffness of testing machine was estimated according to the principle of series springs (Fig. 3.23). The correlation between the specimen equivalent stiffness (E_{eqv}), the stiffness of testing machine (E_t), and the hybrid stiffness (E_x) can be expressed as:

$$\frac{1}{E_x} = \frac{1}{E_{eqv}} + \frac{1}{E_t}.$$ (3.23)

Therefore, the stiffness of testing machine was calculated according to Eq. 3.23, and is listed in Table 3.13. It varies in a big range between 43.16 and 56.41 GPa, and the standard deviation of E_t is much larger than that of E_{eqv} and E_x.

Afterwards the mean value of E_t was taken as the stiffness of testing machine in the present research. Then the equivalent stiffness of the intact specimens (No. 5 to 18), the specimens (No. 10 to 18) after applying 10^4 cycles of fatigue loads were calculated according to Eq. 3.23. The results are given in Table 3.14 and 3.15, respectively.

Fig. 3.22: Using extensometer to measure strain in the stiffness tests.
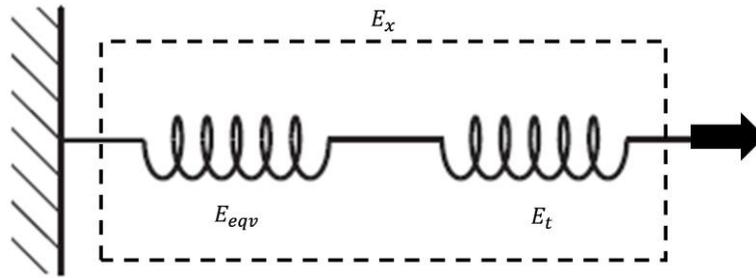
Fig. 3.23: The principle of series springs.

Table 3.13: Comparing the specimen equivalent stiffness, the hybrid stiffness, and the stiffness of testing machine.

Specimen No.	E_{eqv} [GPa]	E_x [GPa]	E_t [GPa]
10	50.92	23.36	43.16
11	50.59	26.67	56.41
12	53.91	25.71	49.15
13	51.94	26.26	53.11
14	49.34	25.99	54.92
Mean:	51.34	25.6	51.35
Standard deviation:	1.71	1.3	5.32

Table 3.14: Equivalent stiffness of the intact specimens (No. 5-18).

Specimen No.	E_{eqv} [GPa]
5	59.53
6	59.91
7	62.4
8	61.19
9	63.25
10	60.9
11	65.53
12	66
13	65.58
14	61.29
15	61.05
16	63
17	62.16
18	60.14
Mean:	62.28
Standard deviation:	2.15

Table 3.15: Equivalent stiffness of the specimens (No. 10-18) after applying 10^4 cycles of fatigue loads.

Specimen No.	E_{eqv} [GPa]
10	51.85
11	55.66
12	50.77
13	46.78
14	52.59
15	50.97
16	54.63
17	50.46
18	50.26
Mean:	51.55
Standard deviation:	2.6

3.7.3.3. EFFECT OF FATIGUE LOADS

A damage parameter (D) is defined in the present research to indicate the fatigue damage accumulation in specimen:

$$D(N) = 1 - \frac{\overline{E(N)}}{\overline{E_0}}, \tag{3.24}$$

where $\overline{E_0}$ is the mean initial stiffness of the intact specimens, and $\overline{E(N)}$ is the mean equivalent stiffness after applying 10^4 (N_1) and 10^6 (N_2) cycles of fatigue loads. As shown in Table 3.16, the damage parameter suggests that the failures accumulated in the specimens after applying cyclic loading, but it remains at a constant level when the fatigue load cycles are 100 times larger. Therefore, it can be concluded that the damage accumulation has reached a plateau before applying 10^4 cycles of fatigue loads.

Table 3.16: The variation of damage parameters of dry specimens.

Damage parameter	$N = N_1$	$N = N_2$
$D(N)$	17.2%	17.6%

Considering the limited number of specimens subjected to stiffness tests, the paired t-test [51] was applied to justify whether the stiffness difference is literally zero. For example, the specimens No. 10-18 have been subjected to stiffness tests in the as-received state and after applying 10^4 cycles of fatigue loads. For each specimen, the difference of equivalent stiffness (ΔE) before and after the fatigue tests is given in Table 3.17. Therefore, the statistic t value is calculated by:

$$t = \frac{\overline{\Delta E} - \mu_E}{S_E / \sqrt{k}}, \tag{3.25}$$

where $\overline{\Delta E}$ is the mean value of the stiffness difference, S_E is the standard deviation of the stiffness difference, k is the number of specimens to be compared. Assuming the average difference of specimen

stiffness is literally 0 before and after applying 10^4 cycles of fatigue loads, i.e., the null hypothesis, then we have:

$$\mu_E = 0. \tag{3.26}$$

The calculation of t value turns out to be 9.686. Because it is bigger than the critical t value of 2.306 [51], the null hypothesis should be rejected. On the contrary, the alternative hypothesis is valid, i.e., the average difference is not 0. Therefore, the specimen stiffness has deteriorated after suffering fatigue loads.

The same paired t-test is applied to compare the stiffness difference of the specimens No. 10-14, which have been subjected to stiffness tests after applying 10^4 and 10^6 cycles of fatigue loads. For each specimen, the difference of equivalent stiffness (ΔE) is given in Table 3.18. The null hypothesis assumes that the average difference is 0, i.e., $\mu_E = 0$. The t value is calculated according to Eq. 3.25, which turns out to be 0.099. Because it is smaller than the critical t value of 2.776 [51], the null hypothesis is accepted. It can be claimed that the stiffness accumulation has not further progressed between the interval of 10^4 and 10^6 cyclic loading.

Table 3.17: The stiffness difference of specimens No. 10-18 before and after applying 10^4 cycles of fatigue loads.

Specimen No.	E_0 [GPa]	$E(N_1)$ [GPa]	ΔE [GPa]
10	60.9	51.85	9.05
11	65.53	55.66	9.87
12	66	50.77	15.23
13	65.58	46.78	18.8
14	61.29	52.59	8.7
15	61.05	50.97	10.08
16	63	54.63	8.37
17	62.16	50.46	11.7
18	60.14	50.26	9.88
		Mean:	11.3
		Standard deviation:	3.5

Table 3.18: The stiffness difference of specimens No. 10-14 after applying 10^4 and 10^6 cycles of fatigue loads.

Specimen No.	$E(N_1)$ [GPa]	$E(N_2)$ [GPa]	ΔE [GPa]
10	51.85	50.92	0.93
11	55.66	50.59	5.07
12	50.77	53.91	-3.14
13	46.78	51.94	-5.16
14	52.59	49.34	3.25
		Mean:	0.19
		Standard deviation:	4.28

3.7.3.4. SPECIMEN STIFFNESS PREDICTED BY CLT

The assumptions of the classical laminate theory (CLT) hold well for the specimens used in stiffness tests, e.g., specimen thickness is relatively very small compared to the dimensions of length and width. Therefore, the theoretical specimen stiffness (E_{clt}) can be calculated by solving the constitutive equations:

$$\begin{bmatrix} \varepsilon_x \\ \varepsilon_y \\ \gamma_{xy} \end{bmatrix} = \begin{bmatrix} a_{11} & a_{12} & a_{16} \\ a_{12} & a_{22} & a_{26} \\ a_{16} & a_{26} & a_{66} \end{bmatrix} \begin{bmatrix} N_x \\ N_y \\ N_{xy} \end{bmatrix}. \tag{3.27}$$

Because no force was applied in the transverse direction during the stiffness tests, N_y is 0 in Eq. 3.27. Then the constitutive equations are converted to:

$$\varepsilon_x = a_{11}N_x + a_{16}N_{xy}, \tag{3.28}$$

$$\varepsilon_y = a_{12}N_x + a_{26}N_{xy}, \tag{3.29}$$

$$\gamma_{xy} = a_{16}N_x + a_{66}N_{xy}. \tag{3.30}$$

The shear deformation of the specimens was restrained by the grips, so γ_{xy} is 0 in Eq. 3.30, and N_{xy} can be defined as a function of N_x:

$$N_{xy} = -\frac{a_{16}}{a_{66}}N_x. \tag{3.31}$$

Substituting this expression into Eq. 3.28, we can get:

$$N_x = \frac{1}{a_{11}-\frac{a_{16}^2}{a_{66}}}\varepsilon_x. \tag{3.32}$$

Dividing both sides of Eq. 3.32 by the specimen thickness (h), then we have:

$$\frac{N_x}{h} = \frac{1}{h\left(a_{11}-\frac{a_{16}^2}{a_{66}}\right)}\varepsilon_x. \tag{3.33}$$

In fact, the left-hand side of Eq. 3.33 is the axial stress (σ_x) in loading direction. This equation is reformed as:

$$\sigma_x = \frac{1}{h\left(a_{11}-\frac{a_{16}^2}{a_{66}}\right)}\varepsilon_x. \tag{3.34}$$

Therefore, the specimen stiffness is calculated by:

$$E_{clt} = \frac{1}{h\left(a_{11}-\frac{a_{16}^2}{a_{66}}\right)}. \tag{3.35}$$

The mechanical properties of the UD CFRP lamina have provided in Table 3.6. Accordingly, the calculation of theoretical specimen stiffness turns out to be 54.87 GPa.

The mean value of equivalent stiffness (E_{eqv}) of the intact specimens No. 5 to 18, resulted from experimental study and the tuning by series springs principle, is 62.28 GPa (Table 3.14). It is 14% higher than the theoretical value. It is suspected that equivalent stiffness of the intact specimens have been overestimated due to the low stiffness of testing machine (E_t). E_t is taken as 51.35 GPa (Table 3.13) in the present research, which would have been underestimated. According to Eq. 3.23, the smaller E_t would have resulted in the larger value of E_{eqv}.

3.8. EXPERIMENT OF WET CFRP SPECIMENS

3.8.1. SALT SOLUTION UPTAKE

According to the experiment design (section 6.2), 18 specimens were submerged in salt water prior to the tests. Water uptake of the 18 specimens were monitored by weighing the specimens at certain intervals. The specimen mass (m) is plotted as a function of time (t) in Fig. 3.24(a). The blue triangles represent the mean of sample mass ($\bar{m}$), and the top and bottom limits represent the maximum and minimum records, respectively. It can be seen that the sample mass has increased quickly in the first three days, subsequently, the increasing trend slowed down. The sample mass remained approximately constant after 40 days, i.e., the specimens have reached saturation. The mass gain ratio ($\Delta\bar{m}/\bar{m}_0$) is given in Fig. 3.24(b), and the maximum ratio is 1.13%. In the experimental investigation of void content ratio (section 4.2), it has been proved that the voids in the composite specimens are very limited. Because the voids are important moisture diffusion paths, a small amount of water could be absorbed by the specimens. Moreover, the moisture diffusion coefficient was calculated based on the mass record of aged specimens (Appendix A.3.5).
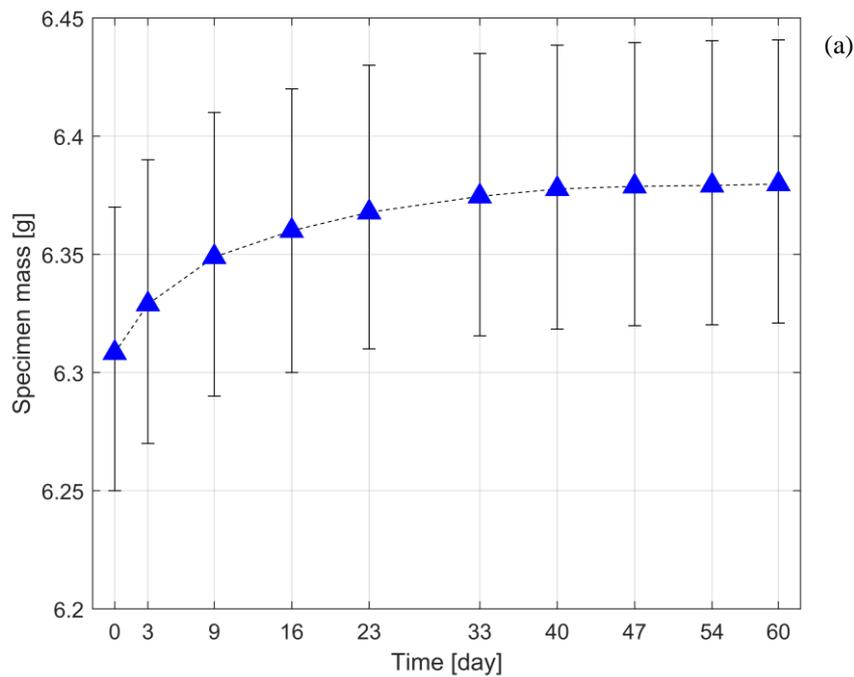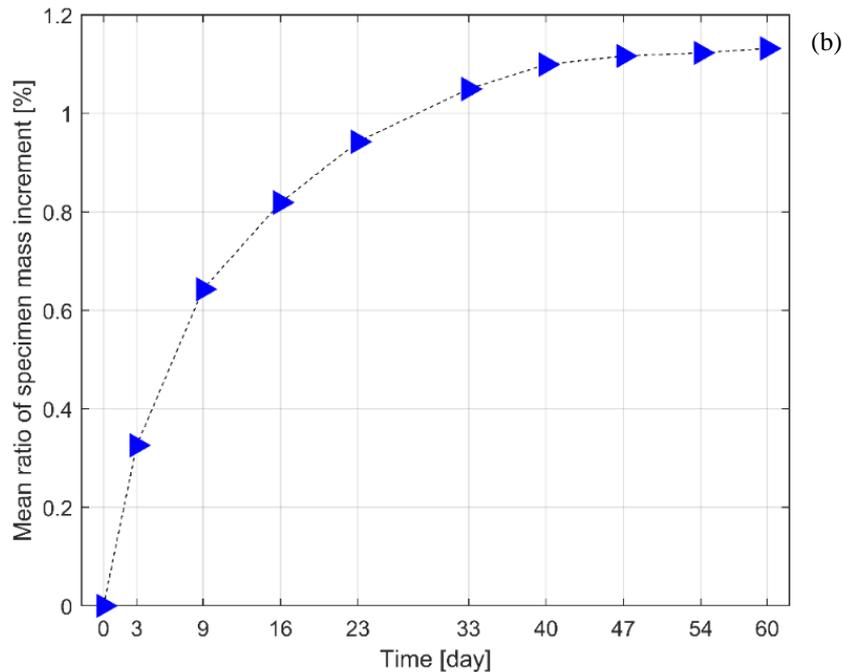
Fig. 3.24: The mass gain of specimens during aging procedure: (a) mass record, and (b) ratio of mean mass gain.

3.8.2. OVERVIEW OF TESTS

The effect of fatigue cyclic loading on the mechanical properties of the saturated ("wet") CFRP specimens was investigated in the same way as for the dry specimens. An overview of the tests with wet specimens is provided in Table 3.19. The strength and stiffness properties of the intact wet specimens were measured, using a Zwick 20kN (Fig. 3.25) and 250kN (Fig. 3.26) static testing machine, respectively. Moreover, the wet specimens were subjected to fatigue tests at a MTS 10kN fatigue testing machine (Fig. 3.27(c)). The residual stiffness and strength properties were measured after 10^4 (N_1) and 10^6 (N_2) cycles of fatigue loads.

In order to maintain the saturation state, the specimens were wrapped with wet papers (Fig. 3.27(a)) and plastic foil (Fig. 3.27(b)) during the fatigue tests. After the fatigue tests (the longest of which lasted for 55 hours), the specimens were protected by the wet papers, the plastic foil, and aluminium foil before proceeding with stiffness/failure tests (Fig. 3.28). All the cover materials were used to stop absorbed moisture from evaporating. Before and after applying 10^6 cycles of fatigue loads (Step 4 in Table 3.19), each specimen was weighed to monitor the mass loss during fatigue tests. The mass record and the result of mass loss ratio are given in Appendix A.3.6. The mean ratio of mass loss turns out to be 0.88%, which is more than 50% of the maximum ratio of mass gain. The mass loss was resulted from not only moisture evaporation, but also the tab damage during fatigue tests. A non-negligible amount of the absorbed moisture was still lost. Therefore, a better solution of maintaining the moisture content in wet specimens is planned in future work.

The experimental records of the quasi-static failure tests are plotted in Fig. 3.29. Apparently, the load (F_{LC})-displacement (w_m) curves of the intact wet specimens (No. 1 to 4) and of the specimens (No. 5 to 9) after applying 10^4 cycles of fatigue loads differ with the curves of specimens (No. 10 to 13) after applying 10^6 cycles of fatigue loads. Because the tabs made of paper were partly damaged during the fatigue tests, the tabs made of sandpaper (Fig. 3.33) have been used for the specimens (No. 10 to 13) in failure tests. The kinks at the curves indicate that some slippage has happened in the beginning of tests and at the tensile force of 2500 N.

All the stiffness tests were performed at a Zwick 250kN static testing machine, using extensometer to measure strain at the gauge area. The tensile force (F_{LC}) is plotted as a function of the elongation (w_m') between two clips of the extensometer in Fig. 3.30. For each group of the specimens, i.e., the intact specimens (No. 5 to 18), the specimens (No. 10 to 18) after applying 10^4 cycles of fatigue loads, and the specimens (No. 14 to 18) after applying 10^6 cycles of fatigue loads, one specimen was loaded up to 1 kN, and the others were loaded up to 800 N.

Fig. 3.25: Failure tests of wet specimens (e.g., specimen No. 1).

Fig. 3.26: Stiffness tests of wet specimens (e.g., specimen No. 18).

(a)
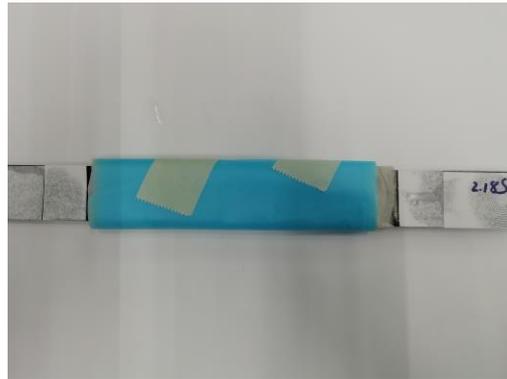
(b)

(c)

Fig. 3.27: The specimens were wrapped with wet papers and plastic foil during fatigue tests (e.g., specimen No. 18).

Fig. 3.28: The wrapped specimens were protected using aluminium foil after fatigue tests (e.g., specimen No. 18).
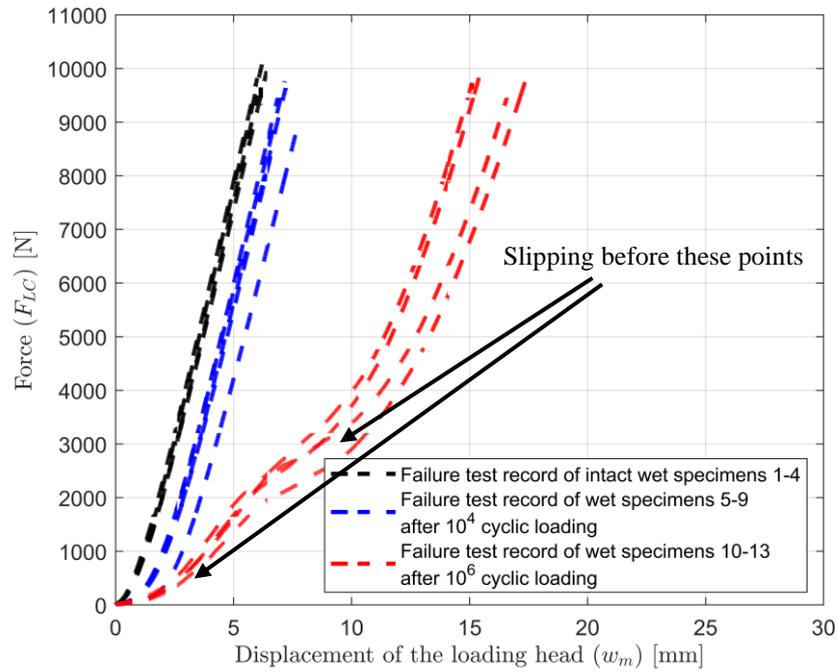
Fig. 3.29: Experimental records of quasi-static failure tests.
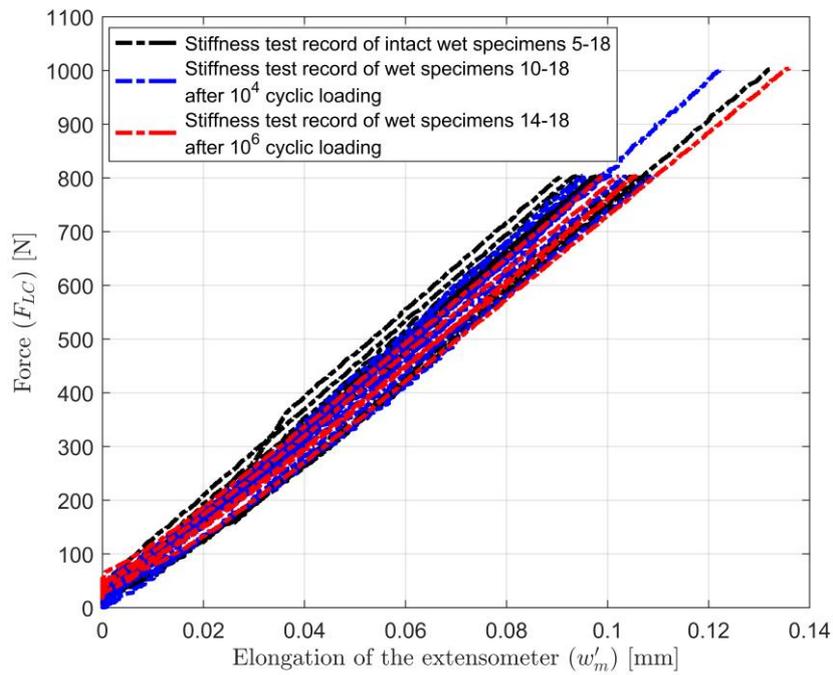
Fig. 3.30: Experimental records of stiffness tests using extensometer to measure strain.

Table 3.19: Overview of the tests with wet specimens.

Specimen No.	Step 1	Step 2	Step 3	Step 4	Step 5
1	F	N/A	N/A	N/A	N/A
2	F	N/A	N/A	N/A	N/A
3	F	N/A	N/A	N/A	N/A

73

4	F	N/A	N/A	N/A	N/A
5	Se	10^4 C	F	N/A	N/A
6	Se	10^4 C	F	N/A	N/A
7	Se	10^4 C	F	N/A	N/A
8	Se	10^4 C	F	N/A	N/A
9	Se	10^4 C	F	N/A	N/A
10	Se	10^4 C	S	10^6 C	F
11	Se	10^4 C	S	10^6 C	F
12	Se	10^4 C	S	10^6 C	F
13	Se	10^4 C	S	10^6 C	F
14	Se	10^4 C	S	10^6 C	Se
15	Se	10^4 C	S	10^6 C	Se
16	Se	10^4 C	S	10^6 C	Se
17	Se	10^4 C	S	10^6 C	Se
18	Se	10^4 C	S	10^6 C	Se

F: quasi-static failure test.

Se: stiffness test, using extensometer to measure strain.

C: fatigue test with defined cyclic loading.

Table 3.20: Experimental results of ultimate tensile failure tests with wet specimens.

Specimen No.	Loading history	Ultimate tensile failure load (F_{ult}) [N]	Ultimate tensile strength (σ_{ult}) [MPa]	Mean tensile strength ($\overline{\sigma_{ult}}$) [MPa]	Standard deviation [MPa]
1		9952.7	622.04		
2	F	9728.8	608.05	618.4	9.37
3		9823.7	613.98		
4		10072.1	629.51		
5		9761.2	610.08		
7	Se, 10^4C, F	8795.8	549.74	588.25	26.84
8		9635	602.19		
9		9456.3	591.02		
10		9974	623.38		
11	Se, 10^4C, Se,	9730.5	608.16	610.73	11.24
12	10^6C, F	9835.3	614.71		
13		9547.2	596.7		

3.8.3. EFFECT OF FATIGUE LOADS ON STRENGTH OF WET SPECIMENS

After the ultimate tensile failure tests, the failed specimens No. 1 to 4, 5 to 9, and 10 to 13 are shown in Figs. 3.31 to 3.33, respectively. The same failure modes, as for the dry specimens, are observed in Fig. 3.31, and which include fibre rupture in the -45° ply, matrix cracking in the 0 and -90° plies, and fibre-matrix disbond (pull-out). Because the tabs made of paper were damaged during the fatigue tests, the tabs made of sandpaper (Fig. 3.33) were used in the failure tests of specimens No. 10 to 13. The experimental results of the ultimate tensile failure load (F_{ult}) are listed in Table 3.13. Because the specimen No. 6 has failed at the tab (Fig. 3.22), which led to a smaller failure load, the strength of specimen No. 6 will not be considered.

The experimental records of ultimate tensile failure load (F_{ult}) are listed in Table 3.20. Moreover, the corresponding tensile strength (σ_{ult}) of each specimen was calculated according to Eq. 3.20. Considering the variation of mean and standard deviation of the tensile strength, no apparent effect of fatigue cyclic loading on the tensile strength of wet specimens can be confirmed. Because the tensile strength is mainly determined by the carbon fibres, the defined fatigue loads have little negative effect on the carbon fibres.

A comparison of the (residual) tensile strength of dry and wet specimens is given in Fig. 3.34, and no significant difference can be observed. Because the carbon fibres are hardly affected by the absorbed moisture, it can be claimed that the aging procedure has not affected the tensile strength of the CFRP specimens used in this research.
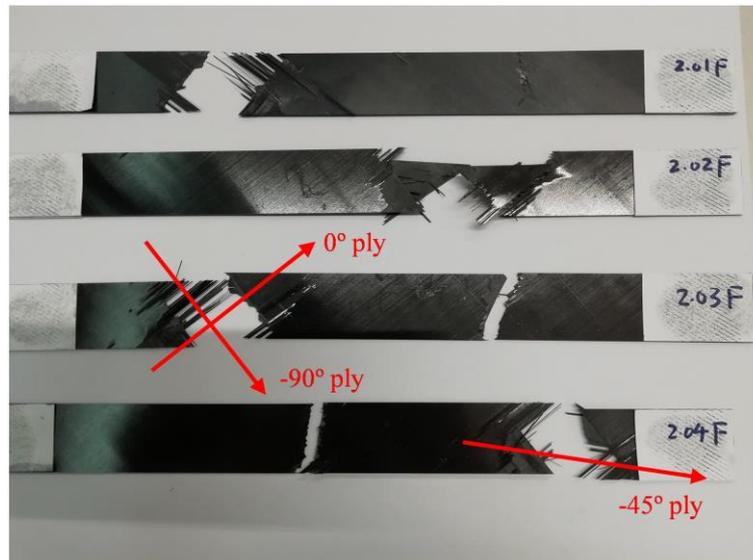
Fig. 3.31: Ultimate tensile failure tests of intact wet specimens No. 1 to 4 (from top to bottom).
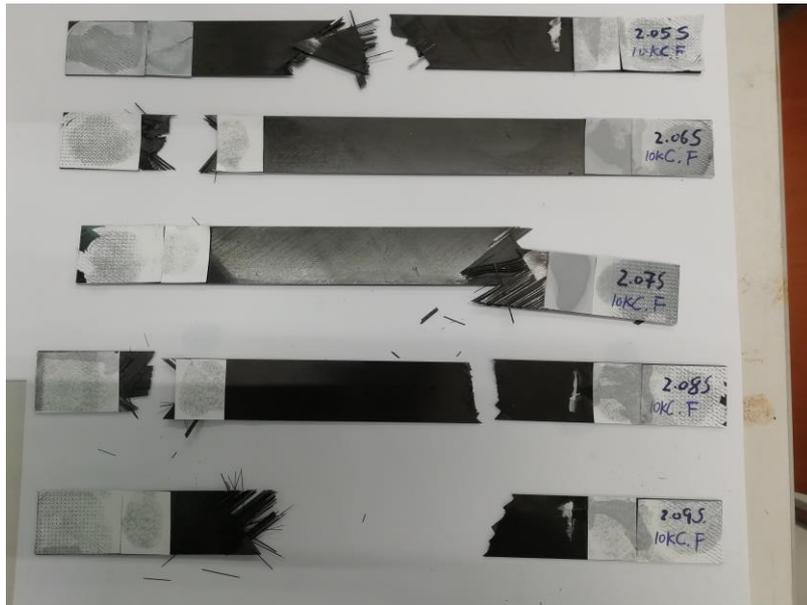
Fig. 3.32: Ultimate tensile failure tests of specimens No. 5 to 9 (from top to bottom).
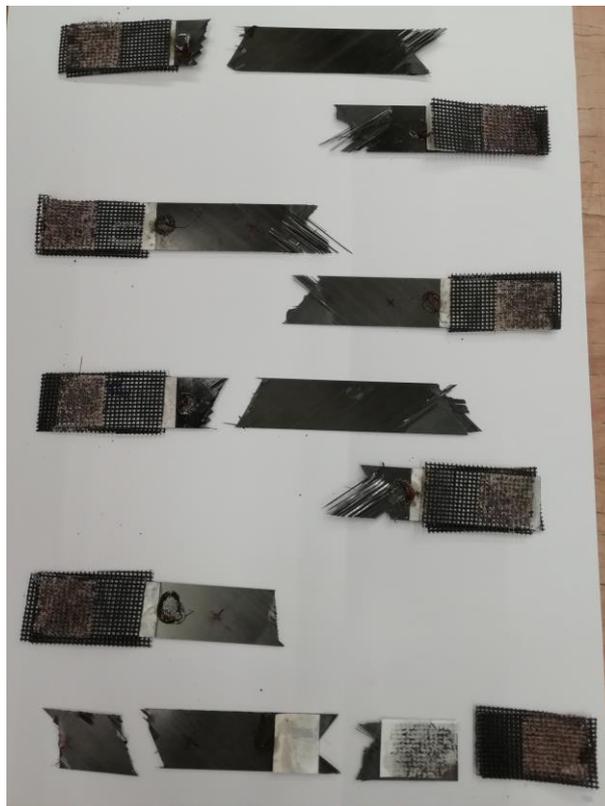
Fig. 3.33: Ultimate tensile failure tests of specimens No. 10 to 13 (from top to bottom).
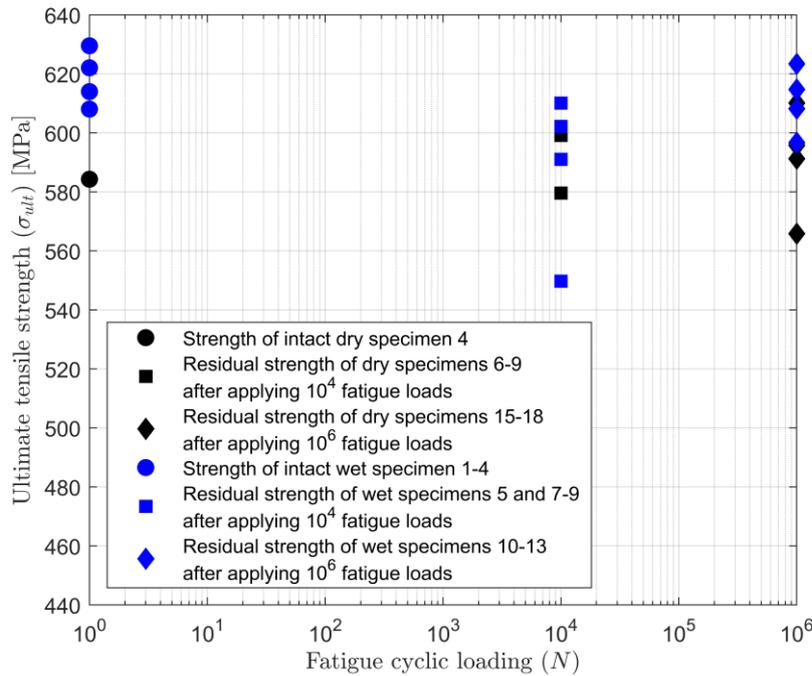
Fig. 3.34: Comparing the (residual) tensile strength of dry and wet specimens.

3.8.4. EFFECT OF FATIGUE LOADS ON STIFFNESS OF WET SPECIMENS

3.8.4.1. EQUIVALENT STIFFNESS OF WET SPECIMENS

In the stiffness tests of wet specimens, the extensometer was used to measure the strain at the gauge area. Therefore, the stress and strain were calculated according to Eqs. 3.21 and 3.22. The specimen equivalent stiffness (E_{eqv}) was defined as the slope of the stress-strain curve. Before each stiffness test, the specimen width (b) and thickness (h) were measured at three different places in the gauge area (Appendix A.3.7). The average of measured width and thickness (25 and 0.64 mm, respectively), were taken in the calculations.

The equivalent stiffness of the intact specimens (No. 5 to 18), the specimens (No. 10 to 18) after 10^4 cycles of fatigue loads, and the specimens (No. 14 to 18) after applying 10^6 cycles of fatigue loads are listed in Table 3.21. Mean stiffness of the intact wet specimens is very close to 54.87 GPa which predicted by the CLT. With the increasing number of cyclic loading, the mean stiffness of the wet specimens decreases from 50.37 GPa to 50.06 and 46.98 GPa, i.e., decreasing by 6.7% after applying 10^6 cycles of fatigue loads. Meanwhile, the standard deviation remains at small values. Therefore, the fatigue cyclic loading has shown damaging effect on the stiffness of wet specimens.

Table 3.21: Equivalent stiffness of wet specimens after applying N cycles of fatigue loads.

Specimen No.	$E_{eqv}(N)$ [GPa]		
	$N = 0$	$N = 10^4$	$N = 10^6$
5	48.71	N/A	N/A
6	50.62	N/A	N/A
7	50.82	N/A	N/A
8	50.29	N/A	N/A
9	48.42	N/A	N/A
10	52.62	50.66	N/A
11	49.12	50.76	N/A
12	52.43	49.97	N/A
13	50.73	49.65	N/A
14	50.17	46.72	46.44
15	50.12	50.01	46.87
16	50.93	52.06	46.57
17	47.33	50.93	47.16
18	52.85	49.77	47.88
Mean:	50.37	50.06	46.98
Standard deviation:	1.61	1.46	0.57

3.8.4.2. EFFECT OF FATIGUE LOADS

The calculation results of damage parameter (D), defined as a function of mean stiffness of the wet specimens (Eq. 3.24), are given in Table 3.22. The damage parameters suggest that the stiffness of wet specimens have not been affected after applying 10^4 (N_1) cycles of fatigue loads, but the stiffness property deteriorated with increasing load cycles up to 10^6 (N_2).

Table 3.22: The variation of damage parameter of wet specimens.

Damage parameter	$N = N_1$	$N = N_2$
$D(N)$	0.6%	6.7%

The paired t-test was applied to compare the stiffness (E_0) of intact specimens (No. 10 to 18) and the residual stiffness of which after applying 10^4 cycles of fatigue loads. The stiffness difference (ΔE) of each specimen is listed in Table 3.23. Holding the null hypothesis that there is literally no difference in stiffness of the two groups of specimens. Therefore, the statistic t value is calculated according to Eq. 3.25, and which turns out to be 0.803. Because it is smaller than the critical t value of 2.306 [51], the null hypothesis is valid. Besides, the residual stiffness of specimens (No. 14 to 18), after applying 10^4 and 10^6 cycles of fatigue loads, as well as the stiffness difference are listed in Table 3.24. The statistic t value turns out to be 3.32 by holding the same null hypothesis. It is larger than the critical t value of 2.776 [51]. Therefore, the null hypothesis should be rejected, i.e., the stiffness of wet specimens have decreased when the fatigue load cycles increased from 10^4 to 10^6.

Table 3.23: The stiffness difference of specimens No. 10-18 before and after 10^4 fatigue cyclic
loading.

Specimen No.	E_0 [GPa]	$E(N_1)$ [GPa]	ΔE [GPa]
10	52.62	50.66	1.96
11	49.12	50.76	-1.64
12	52.43	49.97	2.46
13	50.73	49.65	1.08
14	50.17	46.72	3.45
15	50.12	50.01	0.11
16	50.93	52.06	-1.13
17	47.33	50.93	-3.6
18	52.85	49.77	3.08
		Mean:	0.64
		Standard deviation:	2.39

Table 3.24: The stiffness difference of specimens No. 14-18 after 10^4 and 10^6 fatigue cyclic loading.

Specimen No.	$E(N_1)$ [GPa]	$E(N_2)$ [GPa]	ΔE [GPa]
14	46.72	46.44	0.28
15	50.01	46.87	3.14
16	52.06	46.57	5.49
17	50.93	47.16	3.77
18	49.77	47.88	1.89
		Mean:	2.91
		Standard deviation:	1.96

3.9. CONCLUSION

This is the second step of investigating the short-term fatigue performance of a composite marine propeller. Based on the numerical study of hot-spots at the blade model, the experimental studies given in this chapter include:

- Designing and manufacturing composite specimens according to the lay-up configuration of the most critical hot-spot element.
- Evaluating composite qualities in view of fibre volume fraction and void content ratio, the results show that the hand-made composite laminate has very limited void content.
- Calculating stiffness properties of the unidirectional CFRP material with experiment determined fibre volume fraction, the stiffness properties turn out to be higher than the value provided by material data sheet.
- Designing fatigue cyclic loading according to the stress and moment resultants of the most critical hot-spot element.
- Designing experiments for each 18 non-aged (dry) and aged (wet) specimens. The designed fatigue loads are applied to the composite specimens. Before and after the fatigue tests, the (residual)

stiffness and strength properties are tested for the intact specimens and for specimens after suffering 10^4 and 10^6 cycles of fatigue loads.

The experimental results of the dry specimens show that:

- The tabs are critical for protecting composite specimens. In the quasi-static tensile failure tests, premature failure happened at the specimens without tabs, which has led to serious underestimation of specimen strength. The tabs made of thick paper are proved to work well with all the other specimens.
- Tensile strength of the CFRP specimens are hardly affected by up to 10^6 cycles of fatigue loads. Because the tensile strength is mainly determined by fibres, the carbon fibres are not susceptible to the designed cyclic loading.
- The observed tensile failure modes include fibre rupture in the -45° ply, matrix cracking in the 0 and -90° plies, and fibre-matrix de-adhesion.
- Calculating strain based on the displacement of loading head would seriously underestimate the stiffness. Therefore, the extensometer is crucial for measuring strain at gauge area of the composite specimens.
- The stiffness calculation results are corrected by the principle of series springs, deducting stiffness of the testing machine. The resulted equivalent stiffness of intact specimens is larger than stiffness predicted by classical laminate theory, possibly due to underestimation of stiffness of the testing machine.
- The equivalent stiffness of dry specimens decreased by 17% after applying 10^4 cycles of fatigue loads, while it did not change anymore when the fatigue load cycles increased to 10^6.

The experimental results of the wet specimens show that:

- The procedure of water uptaking is very efficient in the beginning of the aging procedure. The specimens have reached saturation state after immersing in 5% salt water for 60 days. The mass gain is small due to the limited void content.
- The variation of (residual) tensile strength of the wet specimens is very small. Therefore, 10^6 cycles of the designed uniaxial fatigue loads have not much damaging effect on the carbon fibres.
- There is little difference between the strength of dry and wet specimens. Therefore, the ageing procedure has not much damaging effect on the carbon fibres.
- The same tensile failure modes are observed in the wet specimens as in the dry specimens.
- The equivalent stiffness of wet specimens has not affected by applying 10^4 cycles of fatigue loads, but it decreased by 7% after applying 10^6 cycles of fatigue loads.
- Equivalent stiffness of the intact wet specimens is very close to the stiffness predicted by classical laminate theory. It proves that the extensometer has measure the strain accurately.
- During fatigue tests, the mass loss resulted from moisture evaporation and some tab damage accounted for approximately 50% of the mass gain from water uptaking. Therefore, a new method for maintaining wet specimens is required for future research.

- Compared to 10^6 cycles of fatigue loading in the performed tests, the expected number of load cycles on a real propeller during its lifetime is one or more orders higher. Therefore, future experiments with larger number of fatigue load cycles will be necessary for understanding of the long-term fatigue performance of composite propellers.

REFERENCES

[1] Kane, C. and Smith, J., 2003. Composite blades in marine propulsors. In Proceedings of International Conference on Advanced Marine Materials: Technologies and Applications.

[2] International Towing Tank Conference Resistance Committee, 2005. Final report and recommendations to the 24th ITTC. In Proceedings of 24th international towing tank conference, Edinburgh, UK, 2005.

[3] Raj, S. and Reddy, R., 2014. P. Bend-twist coupling and its effect on cavitation inception of composite marine propeller. Int. J. Mech. Eng. Technol, 5, pp.306-314.

[4] CHEN, B., 2006. Design, fabrication and testing of pitch-adapting (flexible) composite propellers. In Propellers/Shafting 2006 Symposium (Vol. 8). SNAME.

[5] He, X.D., Hong, Y. and Wang, R.G., 2012. Hydroelastic optimisation of a composite marine propeller in a non-uniform wake. Ocean engineering, 39, pp.14-23.

[6] Liu, Z. and Young, Y.L., 2009. Utilization of bend–twist coupling for performance enhancement of composite marine propellers. Journal of Fluids and Structures, 25(6), pp.1102-1116.

[7] Young, Y.L., Motley, M.R., Barber, R., Chae, E.J. and Garg, N., 2016. Adaptive composite marine propulsors and turbines: progress and challenges. Applied Mechanics Reviews, 68(6).

[8] Maljaars, P.J. and Kaminski, M.L., 2015. Hydro-elastic analysis of flexible propellers: an overview. In Fourth International Symposium on Marine Propulsors.

[9] Plucinski, M.M., Young, Y.L. and Liu, Z., 2007, July. Optimization of a self-twisting composite marine propeller using Genetic algorithms. In 16th International conference on composite materials, Kyoto, Japan (pp. 8-13).

[10] Lin, C.C., Lee, Y.J. and Hung, C.S., 2009. Optimization and experiment of composite marine propellers. Composite structures, 89(2), pp.206-215.

[11] Blasques, J.P., Berggreen, C. and Andersen, P., 2010. Hydro-elastic analysis and optimization of a composite marine propeller. Marine Structures, 23(1), pp.22-38.

[12] Lee, Y.J. and Lin, C.C., 2004. Optimized design of composite propeller. Mechanics of advanced materials and structures, 11(1), pp.17-30.

[13] Mulcahy, N.L., Prusty, B.G. and Gardiner, C.P., 2010. Hydroelastic tailoring of flexible composite propellers. Ships and Offshore structures, 5(4), pp.359-370.

[14] Maljaars, P.J., Kaminski, M.L. and Den Besten, J.H., 2017. Finite element modelling and model updating of small scale composite propellers. Composite Structures, 176, pp.154-163.

[15] Maljaars, P., Bronswijk, L., Windt, J., Grasso, N. and Kaminski, M., 2018. Experimental validation of fluid–structure interaction computations of flexible composite propellers in open water conditions using BEM-FEM and RANS-FEM methods. Journal of Marine Science and Engineering, 6(2), p.51.

[16] Young, Y.L., 2008. Fluid–structure interaction analysis of flexible composite marine propellers. Journal of fluids and structures, 24(6), pp.799-818.

[17] Taketani, T., Kimura, K., Ando, S. and Yamamoto, K., 2013, May. Study on performance of a ship propeller using a composite material. In The Third International Symposium on Marine Propulsors smp (Vol. 13).

[18] Maljaars, P.J. and Dekker, J.A., 2014. Hydro-elastic analysis of flexible marine propellers. In Maritime Technology and Engineering-Edited by Guedes Soares and Santos, pp.705-715.

[19] Maljaars, P., Grasso, N., Kaminski, M. and Lafeber, W., 2017, June. Validation of a steady BEM-FEM coupled simulation with experiments on flexible small scale propellers. In Proceedings of the Fifth International Symposium on Marine Propulsors, Espoo, Finland (pp. 12-15).

[20] Guen-Geffroy, L., Le Gac, P.Y., Diakhate, M., Habert, B. and Davies, P., 2018, January. Long-term durability of CFRP under fatigue loading for marine applications. In MATEC web of conferences (Vol. 165). EDP Sciences.

[21] Tual, N., Carrere, N., Davies, P., Bonnemains, T. and Lolive, E., 2015. Characterization of sea water ageing effects on mechanical properties of carbon/epoxy composites for tidal turbine blades. Composites Part A: Applied Science and Manufacturing, 78, pp.380-389.

[22] Boisseau, A., Davies, P. and Thiebaud, F., 2012. Sea water ageing of composites for ocean energy conversion systems: influence of glass fibre type on static behaviour. Applied Composite Materials, 19(3-4), pp.459-473.

[23] Boisseau, A., Davies, P. and Thiebaud, F., 2013. Fatigue behaviour of glass fibre reinforced composites for ocean energy conversion systems. Applied Composite Materials, 20(2), pp.145-155.

[24] Visco, A.M., Calabrese, L. and Cianciafara, P., 2008. Modification of polyester resin based composites induced by seawater absorption. Composites part A: applied science and manufacturing, 39(5), pp.805-814.

[25] Cavasin, M., Sangermano, M., Thomson, B. and Giannis, S., 2019. Exposure of glass fiber reinforced polymer composites in seawater and the effect on their physical performance. Materials, 12(5), p.807.

[26] Boisseau, A. and Peyrac, C., 2015. Long term durability of composites in marine environment: comparative study of fatigue behavior. Procedia Engineering, 133, pp.535-544.

[27] Poodts, E., Minak, G. and Zucchelli, A., 2013. Impact of sea-water on the quasi static and fatigue flexural properties of GFRP. Composite Structures, 97, pp.222-230.

[28] Wei, B., Cao, H. and Song, S., 2011. Degradation of basalt fibre and glass fibre/epoxy resin composites in seawater. Corrosion Science, 53(1), pp.426-431.

[29] Gu, H., 2009. Behaviours of glass fibre/unsaturated polyester composites under seawater environment. Materials & Design, 30(4), pp.1337-1340.

[30] Kotsikos, G., Evans, J.T., Gibson, A.G. and Hale, J.M., 2000. Environmentally enhanced fatigue damage in glass fibre reinforced composites characterised by acoustic emission. Composites Part A: Applied Science and Manufacturing, 31(9), pp.969-977.

[31] Nguyen, T., Tang, H., Chuang, T.J., Chin, J., Wu, F. and Lesko, J., 2000. A fatigue model for fiber-reinforced polymeric composites for offshore applications. NIST Technical Note.

[32] Liao, K., Schultheisz, C.R. and Hunston, D.L., 1999. Effects of environmental aging on the properties of pultruded GFRP. Composites Part B: Engineering, 30(5), pp.485-493.

[33] Nunemaker, J.D., Voth, M.M., Miller, D.A., Samborsky, D.D., Murdy, P. and Cairns, D.S., 2018. Effects of moisture absorption on damage progression and strength of unidirectional and cross-ply fiberglass–epoxy composites. Wind Energy Science, 3(1), p.427.

[34] Shan, Y. and Liao, K., 2002. Environmental fatigue behavior and life prediction of unidirectional glass–carbon/epoxy hybrid composites. International Journal of Fatigue, 24(8), pp.847-859.

[35] Krauklis, A.E., Gagani, A.I., Vegere, K., Kalnina, I., Klavins, M. and Echtermeyer, A.T., 2019. Dissolution Kinetics of R-Glass Fibres: Influence of Water Acidity, Temperature, and Stress Corrosion. Fibers, 7(3), p.22.

[36] Qiu, Q. and Kumosa, M., 1997. Corrosion of E-glass fibers in acidic environments. Composites Science and Technology, 57(5), pp.497-507.

[37] Schmitz, G.K. and Metcalfe, A.G., 1966. Stress corrosion of E-glass fibers. Industrial & Engineering Chemistry Product Research and Development, 5(1), pp.1-8.

[38] American Society for Testing and Materials (Filadelfia, Pennsylvania), 2014. ASTM D3039-14: Standard Test Method for Tensile Properties of Polymer Matrix Composite Materials. ASTM.

[39] Kaw, A.K., 2005. Mechanics of composite materials. CRC press.

[40] HEXCEL® (2020) *Product Data Sheet* [Online]. Available at: https://www.hexcel.com/user_area/content_media/raw/HexPly_8552_eu_DataSheet.pdf (Accessed: 29 September 2020).

[41] American Society for Testing and Materials (Filadelfia, Pennsylvania), 2015. ASTM D3171-15: Standard Test Method for Constituent Content of Composite Materials. ASTM.

[42] Vassilopoulos, A.P. and Keller, T., 2011. Fatigue of fiber-reinforced composites. Springer Science & Business Media.

[43] Chawla, N., Tur, Y.K., Holmes, J.W., Barber, J.R. and Szweda, A., 1998. High-frequency fatigue behavior of woven-fiber-fabric-reinforced polymer-derived ceramic-matrix composites. Journal of the American Ceramic Society, 81(5), pp.1221-1230.

[44] Chawla, N., Holmes, J.W. and Lowden, R.A., 1996. HIGH FREQUENCY FATIGUE BEHAVIOR OF. Scripta materialia, 35(12), pp.1411-1416.

[45] Apinis, R., 2004. Accceleration of fatigue tests of polymer composite materials by using high-frequency loadings. Mechanics of Composite Materials, 40(2), pp.107-118.

[46] Saff, C.R., 1983. Effect of load frequency and lay-up on fatigue life of composites. In Long-term behavior of composites. ASTM International.

[47] Kaynak, C. and Mat, O., 2001. Uniaxial fatigue behavior of filament-wound glass-fiber/epoxy composite tubes. Composites Science and Technology, 61(13), pp.1833-1840.

[48] Eftekhari, M. and Fatemi, A., 2016. On the strengthening effect of increasing cycling frequency on fatigue behavior of some polymers and their composites: Experiments and modeling. International Journal of Fatigue, 87, pp.153-166.

[49] Mandell, J.F., 1991. Fatigue behavior of short fiber composite materials. In Composite materials series (Vol. 4, pp. 231-337). Elsevier.

[50] Montgomery, D.C. and Runger, G.C., 2010. Applied statistics and probability for engineers. John Wiley & Sons.

[51] B. Burt Gerstman (2016) StatPrimer (Version 7.0) [Online]. Available at: https://www.sjsu.edu/faculty/gerstman/StatPrimer/t-table.pdf (Accessed: 29 September 2020).

[52] Shen, C.H. and Springer, G.S., 1976. Moisture absorption and desorption of composite materials. Journal of composite materials, 10(1), pp.2-20.

APPENDIX

A.3.1: Stress and moment resultants of the hot-spot element (No. 1421) under each load case.

Load case (p)	N_1^p [MPa·mm]	N_2^p [MPa·mm]	N_{12}^p [MPa·mm]	M_1^p [MPa·mm²]	M_2^p [MPa·mm²]	M_{12}^p [MPa·mm²]
1	20.8	34.5	-2.4	3.3	-1.4	-1.0
2	19.8	33.0	-2.3	3.1	-1.4	-1.0
3	19.2	32.0	-2.2	3.0	-1.3	-0.9
4	19.0	31.6	-2.2	3.0	-1.3	-0.9
5	19.1	31.8	-2.2	3.0	-1.3	-0.9
6	19.6	32.7	-2.3	3.1	-1.4	-1.0
7	19.9	33.1	-2.3	3.2	-1.4	-1.0
8	19.8	32.9	-2.3	3.1	-1.4	-1.0
9	19.7	32.8	-2.3	3.1	-1.4	-1.0
10	19.6	32.7	-2.3	3.1	-1.4	-1.0
11	19.5	32.4	-2.3	3.1	-1.3	-1.0
12	19.4	32.3	-2.3	3.1	-1.3	-1.0
13	19.8	33.0	-2.3	3.1	-1.4	-1.0
14	20.0	33.3	-2.3	3.2	-1.4	-1.0
15	20.1	33.4	-2.3	3.2	-1.4	-1.0
16	20.2	33.6	-2.4	3.2	-1.4	-1.0
17	20.3	33.8	-2.4	3.2	-1.4	-1.0
18	20.4	33.9	-2.4	3.2	-1.4	-1.0
19	20.4	33.9	-2.4	3.2	-1.4	-1.0
20	20.5	34.0	-2.4	3.2	-1.4	-1.0
21	20.5	34.0	-2.4	3.2	-1.4	-1.0
22	20.4	33.9	-2.4	3.2	-1.4	-1.0
23	20.4	33.9	-2.4	3.2	-1.4	-1.0
24	20.4	33.8	-2.4	3.2	-1.4	-1.0
25	20.3	33.7	-2.4	3.2	-1.4	-1.0
26	20.2	33.6	-2.3	3.2	-1.4	-1.0
27	20.1	33.4	-2.3	3.2	-1.4	-1.0
28	20.0	33.2	-2.3	3.2	-1.4	-1.0
29	19.9	33.0	-2.3	3.2	-1.4	-1.0
30	19.7	32.8	-2.3	3.1	-1.4	-1.0
31	19.6	32.5	-2.3	3.1	-1.4	-1.0
32	19.4	32.2	-2.3	3.1	-1.3	-1.0
33	19.3	32.0	-2.2	3.1	-1.3	-0.9
34	19.1	31.7	-2.2	3.0	-1.3	-0.9
35	18.9	31.4	-2.2	3.0	-1.3	-0.9
36	18.7	31.1	-2.2	3.0	-1.3	-0.9

37	18.5	30.8	-2.2	2.9	-1.3	-0.9
38	18.3	30.5	-2.1	2.9	-1.3	-0.9
39	18.2	30.2	-2.1	2.9	-1.3	-0.9
40	18.0	29.8	-2.1	2.8	-1.2	-0.9
41	17.8	29.5	-2.1	2.8	-1.2	-0.9
42	17.6	29.2	-2.0	2.8	-1.2	-0.9
43	17.4	28.9	-2.0	2.8	-1.2	-0.9
44	17.3	28.7	-2.0	2.7	-1.2	-0.8
45	17.2	28.5	-2.0	2.7	-1.2	-0.8
46	17.1	28.4	-2.0	2.7	-1.2	-0.8
47	17.0	28.3	-2.0	2.7	-1.2	-0.8
48	17.0	28.2	-2.0	2.7	-1.2	-0.8
49	17.0	28.3	-2.0	2.7	-1.2	-0.8
50	17.1	28.4	-2.0	2.7	-1.2	-0.8
51	17.2	28.6	-2.0	2.7	-1.2	-0.8
52	17.2	28.7	-2.0	2.7	-1.2	-0.8
53	17.3	28.8	-2.0	2.7	-1.2	-0.8
54	17.6	29.4	-2.0	2.8	-1.2	-0.9
55	18.5	30.8	-2.1	2.9	-1.3	-0.9
56	19.7	32.8	-2.3	3.1	-1.3	-1.0
57	21.0	35.0	-2.4	3.3	-1.4	-1.0
58	22.0	36.7	-2.6	3.5	-1.5	-1.1
59	22.5	37.5	-2.6	3.6	-1.6	-1.1
60	21.9	36.4	-2.5	3.5	-1.5	-1.1

A.3.2: Designing uniaxial force for each load case.

Load case (p)	Loading direction (θ) [°]	Uniaxial load (N_x) [MPa·mm]
1	38	55.3
2	38	52.8
3	38	51.2
4	38	50.5
5	38	50.9
6	38	52.3
7	38	53.0
8	38	52.7
9	38	52.5
10	38	52.3
11	38	51.9
12	38	51.8
13	38	52.8
14	38	53.4
15	38	53.5
16	38	53.8
17	38	54.1
18	38	54.2
19	38	54.3
20	38	54.4
21	38	54.4
22	38	54.4
23	38	54.3
24	38	54.2
25	38	54.0
26	38	53.8
27	38	53.5
28	38	53.2
29	38	52.9
30	38	52.5
31	38	52.1
32	38	51.7
33	38	51.2
34	38	50.8
35	38	50.3
36	38	49.8
37	38	49.3
38	38	48.8

39	38	48.3
40	38	47.8
41	38	47.3
42	38	46.8
43	38	46.4
44	38	46.0
45	38	45.7
46	38	45.4
47	38	45.3
48	38	45.2
49	38	45.3
50	38	45.5
51	38	45.8
52	38	45.9
53	38	46.0
54	38	47.0
55	38	49.2
56	38	52.4
57	38	56.0
58	38	58.7
59	38	60.0
60	38	58.3

A.3.3: The schematic explanation of composing UD CFRP material patches.
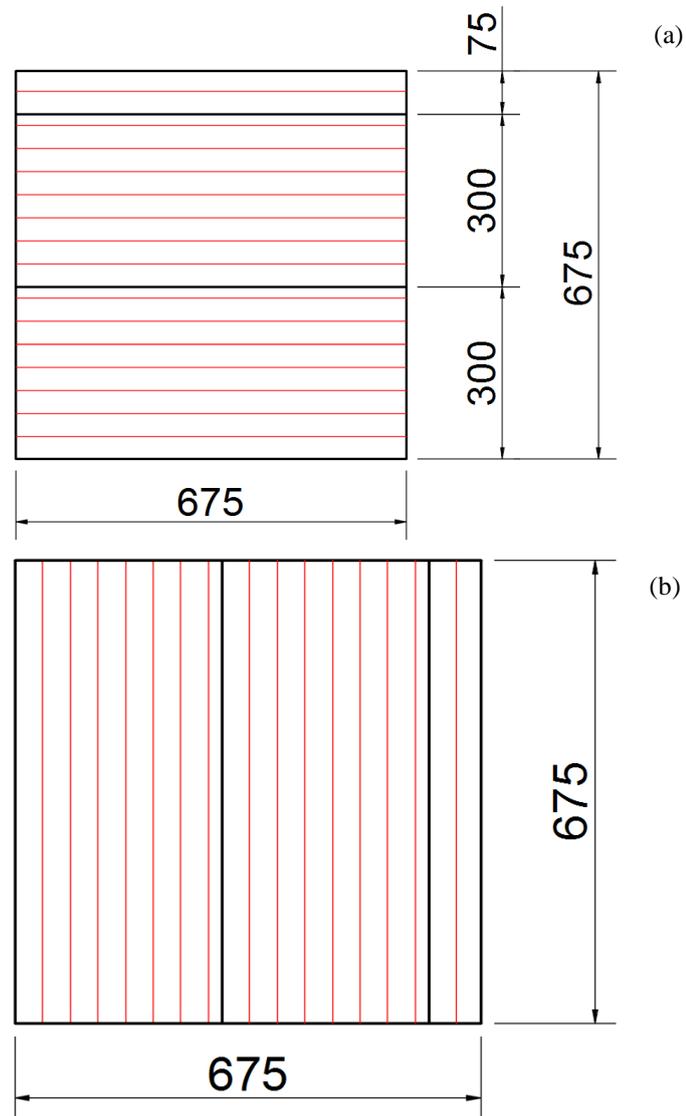
Fig. 3.35: Composing patches to make 0º (a) and -90º (b) laminae [mm].

(a)

(b)

(c)

(d)
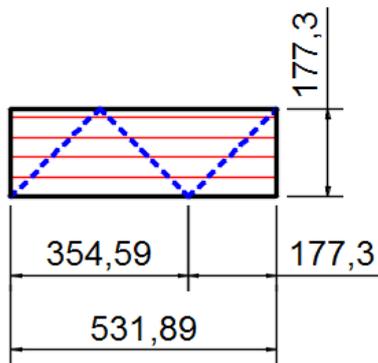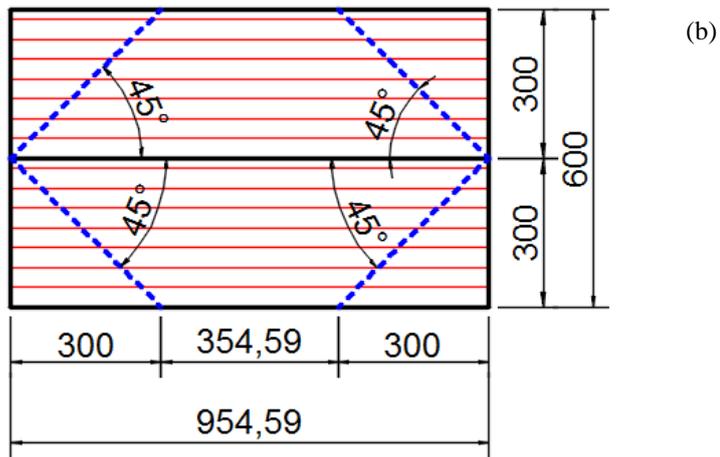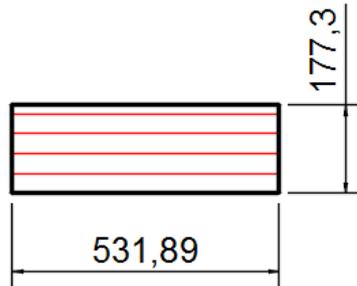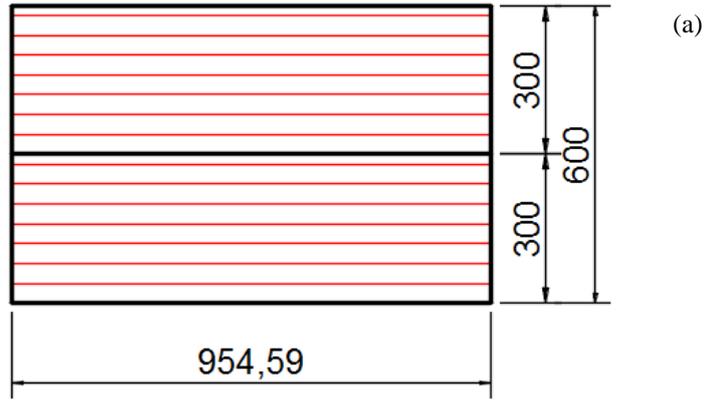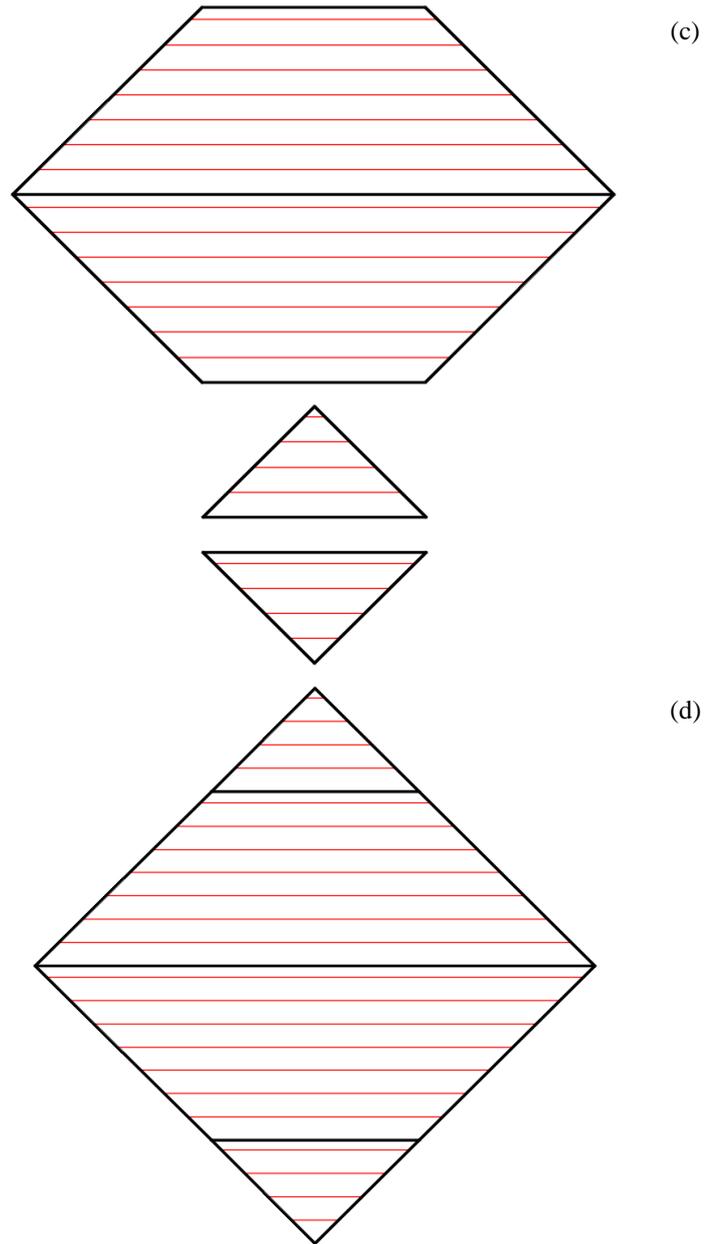
Fig. 3.36: Composing patches to make -45° lamina [mm].

A.3.4: The schematic explanation of cutting the laminated composite plate to specimens.
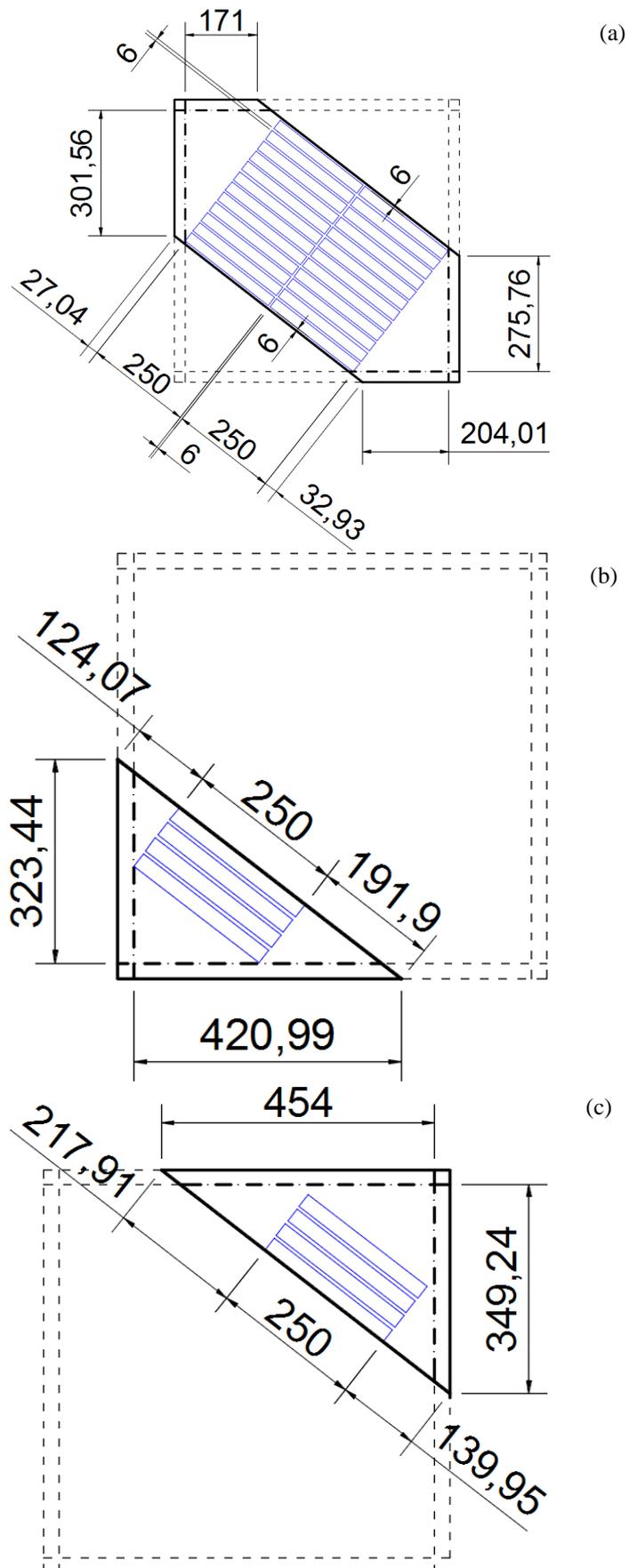
Fig. 3.37: Cutting plan of CFRP laminated plate.

A.3.5: The moisture diffusion coefficient.

Considering the specimen thickness is relatively very small compared to the in-plane dimensions of length and width, the diffusion via the specimen edges is reasonably overlooked. Therefore, the diffusivity in the thickness direction (D_h) is calculated by [52]:

$$D_h = \pi \left(\frac{h}{4 \cdot \Delta m_{max}}\right)^2 \left(\frac{\Delta m_2 - \Delta m_1}{\sqrt{t_2} - \sqrt{t_1}}\right)^2,$$ (3.36)

where h is the specimen thickness, Δm_{max} is the maximum mass gain from water uptaking. The specimen mass increment (Δm) is plotted as a function of time ($\sqrt{t}$) in Fig. 3.37. In the linear region of mass increment curve, Δm_1 and Δm_2 are the two levels of mass gain at $\sqrt{t_1}$ and $\sqrt{t_2}$, respectively. When $\sqrt{t_1}$ and $\sqrt{t_2}$ are taken as 0 and 882 s$^{1/2}$, the calculation of D_h turns out to be 4×10^{-8} mm^2/s.
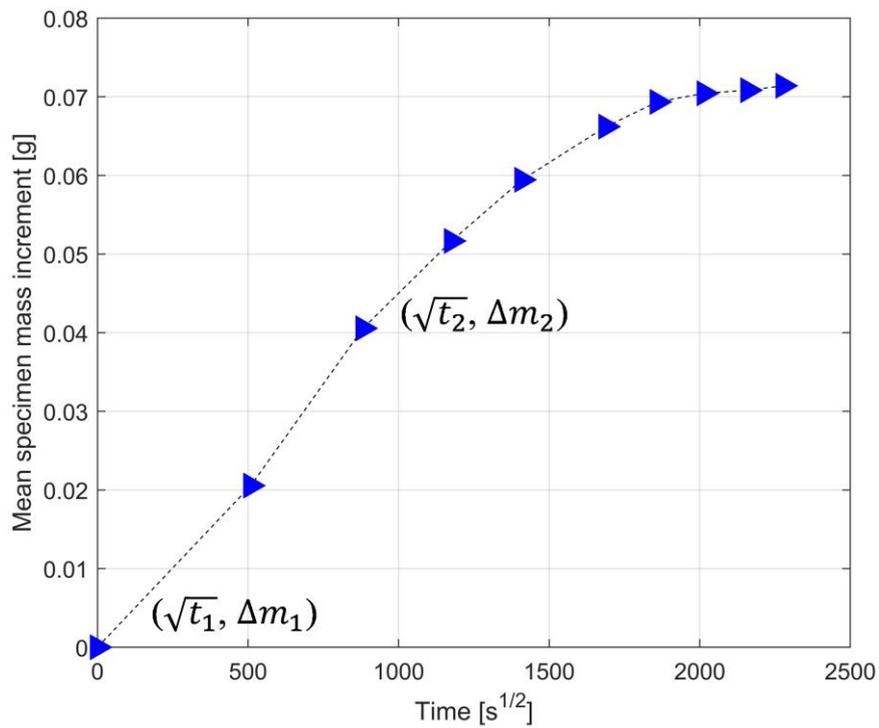
Fig. 3.38: The mean mass increment during aging procedure.

A.3.6: The mass loss of specimens during 10^6 cyclic loading.

Specimen No.	Specimen mass [g]		Mass loss ratio [%]
	Before fatigue test	After fatigue test	
10	7.6745	7.5963	-1.02
11	7.6976	7.5853	-1.46
12	7.7175	7.6655	-0.67
13	7.6618	7.5891	-0.95
14	7.6268	7.5435	-1.09
15	7.6143	7.5472	-0.88
16	7.7659	7.7173	-0.63
17	7.6530	7.6137	-0.51
18	7.7213	7.6670	-0.70
Mean:			-0.88

A.3.7: Width and thickness of wet specimens.

Before each stiffness test, the specimen width (b) and thickness (h) were measured at three different locations in the gauge area. Generally, the width was measured using a digital calliper with the resolution of 0.01 mm, and the thickness was measured using a digital micrometer with the resolution of 0.001 mm.

Table 3.25: Intact specimens (No. 5 to 18).

Specimen No.	Width (b) [mm]	Thickness (h) [mm]
	25.07	0.634
5	25.07	0.636
	25.08	0.635
	25.08	0.642
6	25.07	0.643
	25.07	0.641
	25.08	0.636
7	25.09	0.640
	25.09	0.638
	25.10	0.634
8	25.10	0.637
	25.10	0.635
	25.07	0.636
9	25.06	0.646
	25.07	0.646
	25.13	0.638
10	25.11	0.649
	25.10	0.639
	25.02	0.637
11	25.01	0.636
	25.02	0.631
	25.06	0.633
12	25.06	0.643
	25.08	0.643
	25.06	0.644
13	25.05	0.643
	25.04	0.648
	25.06	0.640
14	25.07	0.643
	25.05	0.635
15	25.01	0.645

	25.01	0.648
	25.01	0.645
	25.08	0.650
16	25.11	0.643
	25.08	0.641
	25.05	0.638
17	25.06	0.638
	25.04	0.638
	25.03	0.645
18	25.04	0.644
	25.03	0.654

Table 3.26: The specimens (No. 10 to 18) after applying 10^4 cycles of fatigue loads.

Specimen No.	Width (b) [mm]	Thickness (h) [mm]
	25.09	0.642
10	25.12	0.648
	25.12	0.640
	25.02	0.629
11	25.03	0.636
	25.04	0.640
	25.03	0.633
12	25.06	0.636
	25.03	0.638
	25.02	0.643
13	25.00	0.642
	25.04	0.642
	25.03	0.639
14	25.03	0.639
	25.03	0.634
	25.02	0.637
15	25.00	0.642
	25.02	0.641
	25.06	0.641
16	25.07	0.636
	25.08	0.646
	25.05	0.635
17	25.07	0.639
	25.07	0.640
18	25.03	0.643

| | 25.04 | 0.644 |
| | 25.06 | 0.655 |

Table 3.27: The specimens (No. 14 to 18) after applying 10^6 cycles of fatigue loads.

Specimen No.	Width (b) [mm]	Thickness* (h) [mm]
14	25.14	0.64
	25.12	0.64
	25.14	0.64
15	25.13	0.64
	25.12	0.64
	25.12	0.64
16	25.14	0.65
	25.14	0.63
	25.14	0.65
17	25.11	0.64
	25.14	0.65
	25.12	0.64
18	25.12	0.65
	25.14	0.64
	25.11	0.65

* A non-digital micrometer with the resolution of 0.01 mm was used to measure the thickness.

4

Mechanical Behaviour of Composite Laminates Embedded with Piezoelectric Wafer Sensors

4.1. INTRODUCTION

Recent advancements of measurement hardware and data management systems and infrastructure are rapidly unlocking the potentials of self-monitoring composites with embedded sensors. Composite materials, because of their layered structure, make it possible to embed certain sensors internally.

Typically, optical fibres with fibre Bragg gratings (FBGs) or thin piezoelectric (PZT) wafers are embedded, as described by Frieden et al. [1] and Seaver et al. [2] regarding FBGs, and Lin and Chang [3] using PZT sensors. FBGs can be manufactured in small size. Therefore, the properly embedded FBGs have negligible impact on structural integrity [4], [5]. Compared to FBGs, PZT wafers allow measurements over a wider range of frequencies [6]. Besides, PZT sensors are expected to be less vulnerable and challenging to handle than optical fibres during the manufacturing and embedding process [7]. These motivate a great potential for PZT sensors for various types of measurements, including dynamic pressure, acceleration, ultrasonic waves, and possible simultaneous combinations. A limitation of applying PZT sensors is the measurement in static and very low frequency conditions, in which the solutions based on optical fibres would be more appropriate.

Generally, PZT sensors can be embedded inside a composite laminate in two ways. One is to place a sensor in between two neighbouring plies [6]-[15]. The other way is to cut a space into one or more plies to house the sensor [3], [9], [10] and [16]. Moreover, if the base materials are electrically conductive, e.g., CFRP material, PZT sensors must be electrically insulated from their surroundings. This has been achieved through a polyimide layer [1], [9]-[11], [13], [17] and [18], a layer of GFRP material [1], [9] and [19], or a thermoplastic foil [20].

Before promoting self-monitoring composite materials in engineering applications, the influence of embedding sensors on the mechanical properties of host materials is a key subject to be investigated. The influence of an embedded PZT sensor on the tensile strength and fatigue property of CFRP specimens has been investigated by Mall [10]. In this research the sensors were embedded inside the cut-out or placed between two neighbouring plies. The results showed that the tensile strength deviated up to 5% from that of the pristine specimens (without embedded sensor), whereas no difference was observed in the fatigue performance. Paget and Levin did not observe decrease in tensile and compressive strengths when PZT sensors were embedded in the thin CFRP laminates [13]. When the glass plates were embedded in CFRP specimens (with different embedding configurations), however, a drop in the tensile strength was observed by Shukla and Vizzini [21]. In the work presented by Lin and Chang [17], a SMART layer (Stanford Multi-Actuator-Receiver Transduction Layer, including a pre-processed polyimide insulation layer) was embedded in CFRP specimens. In view of the shear, compression, and out-of-plane tensile properties, structural integrity of the CFRP specimens was not inherently sacrificed. In another research, Andreades et al. [1] investigated the CFRP specimens with embedded PZT sensors, which had different electrical insulation materials. Compared to pristine sensor-free specimens, they found that the specimens with GFRP electrical insulation generally had statistically

indistinguishable shear, compressive and flexural strengths. The polyimide electrical insulated specimens did show more prominent strength deviations in comparison to specimens without sensor.

In addition to experimental studies, the finite element (FE) analysis has also been applied to study the mechanical behaviour of composite specimens with embedded sensors. For example, Andreades et al. [1] used a continuous damage mechanics method in the FE analysis to minimise the structural degradation risk by embedding a PZT sensor in CFRP laminate. The optimised configuration was later employed in their manufactured specimens. Lampani et al. [16] performed a progressive failure analysis concerning four-point bending test of a GFRP specimen with embedded PZT sensor, involving large deformation. The force-displacement relationship of the FE analysis was congruent with the experimental records. Considering a CFRP rotor blade flexbeam with PZT sensors embedded in different locations [22], accumulative damage simulation, including out-of-plane normal and shear strength criteria, has been performed by Butler et al.

The progressive failure analysis (PFA) of laminated fibre-reinforced composites constitutes two parts: predicting the failure onset and defining the post-failure behaviour. Overviews of the composite failure criteria can be found in [23]-[28]. Failure occurring in a lamina does not necessarily signify the total loss of load-carrying capability because the stress is then redistributed in the laminate. Therefore, it is important to capture the behaviour of laminated composites beyond first ply failure [1], [16] and [29]-[31]. An overview of various post-failure theories of laminated composites is given in [32]. According to the Hahn-Tsai theory [33], for example, a failed lamina will keep bearing load until the total failure of laminate. The Petit-Waddoups theory [34] assumes that a failed lamina is unloaded gradually, while a sudden drop of the load carrying capacity in the failed lamina is assumed in the Chiu theory.

The reported partly inconsistent observations are believed to demand further research on the performance of composite laminates with embedded sensors. The objective here is to better understand how embedded sensors affect the strength but also the failure mode of composite laminates. This will help in the design of structural health monitoring systems through better selection of the location of the sensor and knowledge of when its localised effects trigger macroscopic changes in laminate strength or stiffness. In the current research laminated CFRP materials with and without embedded PZT sensors are experimentally and numerically analysed. The experiments include four-point bending failure tests. Each type of specimen is numerically simulated, and the PFA is carried out with the FE models of the specimens. By comparing the experimental records and the corresponding numerical analysis results, the dominant global stiffness degradation mechanism and the final failure mechanism are identified. The experiments using aged specimens with embedded sensors with consideration of fatigue loading effect have been planned for future research. This chapter is organised as follows: first the structural details of the CFRP specimens with and without embedded sensors are introduced in section 2. The section 3 focuses on the modelling and PFA methods. In section 4, the PFA is first performed with the FE model of the pristine specimen, and specimens with embedded small and large sensors. The

numerical analysis results are correlated with experimental records. In the end the effects of insulation materials (woven GFRP fabric and neat resin) on the global bending stiffness are studied.

4.2. EXPERIMENT

4.2.1.   MANUFACTURING SPECIMENS

Ten rectangular specimens were manufactured. The specimens were made of the unidirectional (UD) AS4/8552 CFRP prepreg material in the $[(0º, 90º)_7, 0º]$s symmetrical cross-ply lay-up configuration. Depending on the different designs, a small space was cut in five plies (from the 21st to the 25th ply, or from the 6th to the 10th ply) to accommodate the embedded sensor and the electrical insulation materials. Two types of PZT sensor made of PZ27 (Meggitt/Ferroperm [35]) have been employed, and the dimensions of the sensors are given in Table 4.1. The PZT sensor was electrically insulated from the CFRP laminate by means of the woven GFRP fabric (HexForce 00106/Araldite LY 5052), which was placed manually over the sensor surfaces. As shown in Fig. 4.1, the neat resin (HexPly 8552 epoxy resin) filled the gap between the laminate and the embedded materials. The PZT sensor was tied to the data acquisition system via the bifilar wiring (enamelled copper with diameter of 0.15 mm) and the SMC connector (insulated from the laminate by using Kapton tape). The wiring was embedded between two neighbouring plies (Fig. 4.2). Besides, the pristine specimens (without embedded sensor) were made of the same CFRP material and had the same layup. The laminated materials were cured conforming to the prepreg supplier cure cycle [36], which gave the final thickness of 5.4 mm ± 0.1 mm corresponding to a cured per-ply-thickness of 0.18 mm. Then the laminates were cut into specimens of 150 mm length and 26 mm width.

The specimens were subjected to four-point bending tests until failure. The number and the corresponding design of each type of the specimen, regarding the sensor type and the position of the embedded sensor, as well as the consequent loading condition for the sensor, are specified in Table 4.2.

Table 4.1: The dimensions of the embedded sensors.

Sensor type	Sensor diameter [mm]	Sensor thickness [mm]
Small	7	0.24
Large	20	0.29

Table 4.2: The specification of the experimental specimens.

Number of specimens	Type of the embedded PZT sensor	Position of the embedded PZT sensor	Loading condition of the embedded PZT sensor
4	No sensor	N/A	N/A
2	Small	Between 21st and 25th ply	Compression

| 2 | Small | Between 6th and 10th ply | Tension |
| 2 | Large | Between 21st and 25th ply | Compression |
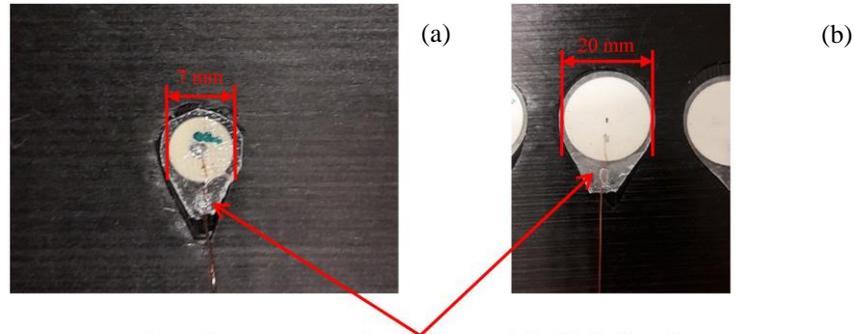
The gap between sensor and composite material is filled with resin.

Fig. 4.1: The cut-out and the embedded (a) small sensor, and (b) large sensor, with the insulation materials.
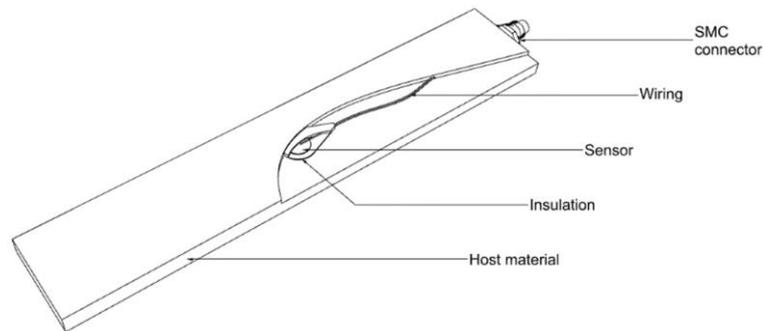
Fig. 4.2: Cutaway drawing of the specimen with embedded sensor, showing different components.

4.2.2. EXPERIMENTAL PROCEDURE

Four-point bending tests were performed in a Zwick/Roell 1455 universal testing machine. According to the ASTM D6272 standard [37], the loading and the support pins were placed 40 mm and 120 mm apart, respectively. The pins were made of steel and had a radius of 5 mm. To prevent premature failure of the specimen at the loading pins, the aluminium AL6082 tabs (with the dimensions of $15 \times 15 \times 3$ mm) were placed between the specimen and the pins (Fig. 4.3). The specimens were monotonically loaded with the constant crosshead velocity of 1 mm/min. The force acting on the crosshead and its displacement were recorded during the test. The loading procedure continued up to the level where the force sustained by the specimen decreased to half of the maximum recorded force. Besides, as can be seen in this figure, the acoustic emission sensors were also used in the tests, but the processing of acoustic data is beyond the scope of this thesis.
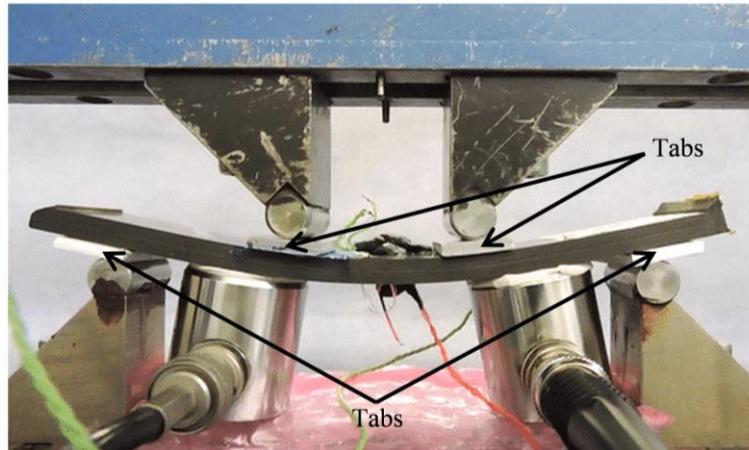
Fig. 4.3: A specimen with embedded small sensor on the compression side loaded towards failure.

4.3. PROGRESSIVE FAILURE ANALYSIS

4.3.1. FINITE ELEMENT MODELLING METHOD

The FE models of the different specimens were built in similar way. For example, the solid model of the composite laminate with embedded small sensor is presented in Fig. 4.4. A quarter of the laminate was modelled in view of symmetry. This model was discretised by the three-dimensional 20-node solid elements with three degrees of freedom per node (translations in the x, y and z directions) [38]. These elements have been applied to discretise all the models presented in this chapter. With reference to Fig. 4.4, the size of the elements along the x axis (from 0 to 75 mm) decreased from 1 mm to 0.35 mm, and along the z axis (from 0 to 13 mm) decreased from 0.5 mm to 0.35mm. Each ply was modelled by one element in the thickness direction, i.e., y-direction in the global coordinate system. The total number of elements was 28050. The symmetrical cross-ply stacking sequence of the CFRP laminate is shown in Fig. 4.5, where the different local coordinate systems defined for the 0º and 90º plies are presented as well. The fibre direction of the UD CFRP material is defined in line with the x-axis of the local coordinate system. The PZT sensor was implanted on the compression side of the laminate (at ply 23 from the bottom), and was enclosed by plain-weave GFRP fabric for the sake of electrical insulation. Moreover, the sensor and the woven GFRP fabric were encircled by the neat resin (Fig. 4.4(b)). As for the sensor and the insulation materials, the local coordinate system of the corresponding elements (Fig. 4.5(a)) is aligned the one for 0º plies. Perfect bonding was assumed between the PZT sensor, GFRP material, resin, and CFRP laminate. The ply interfaces were assumed to be perfectly bonded in the laminate. The commercial FE analysis software ANSYS has been used for the implementation of the models, and the element type SOLID186 was used in discretising the models.

(a)
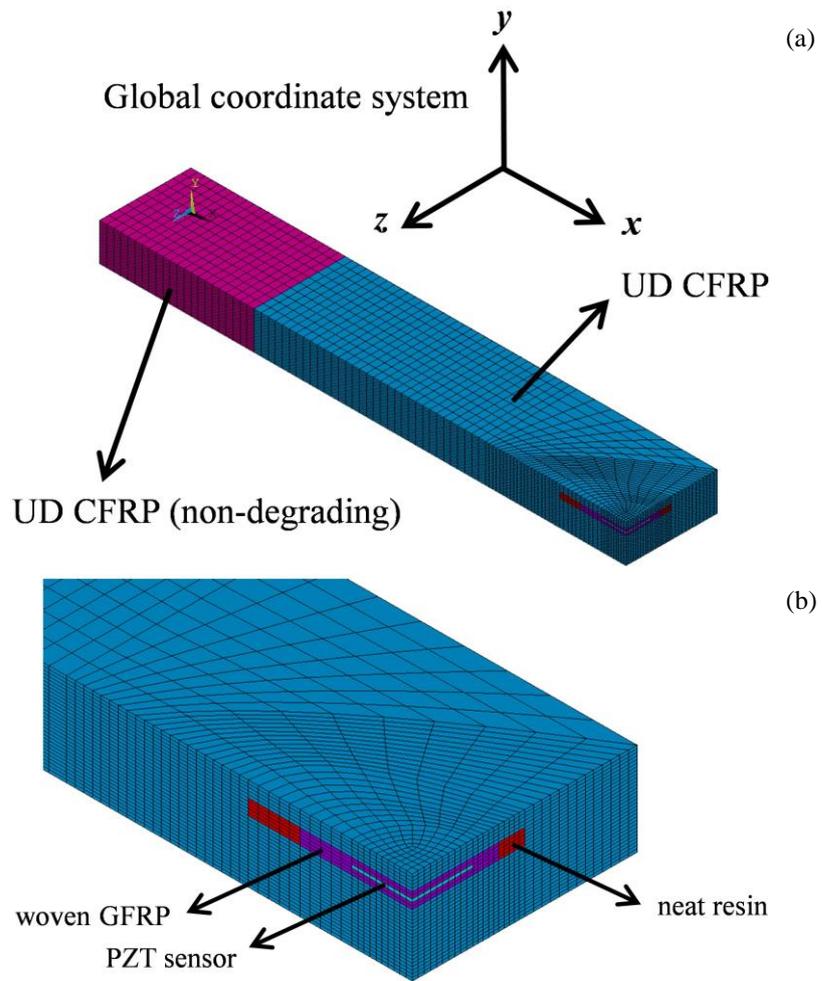
Fig. 4.4: The FE model of the composite laminate with embedded small sensor (on the compression side): (a) the overview of the FE model, and (b) the detail view of the PZT sensor (embedded at ply 23) and the insulation materials.

(b)

(a)
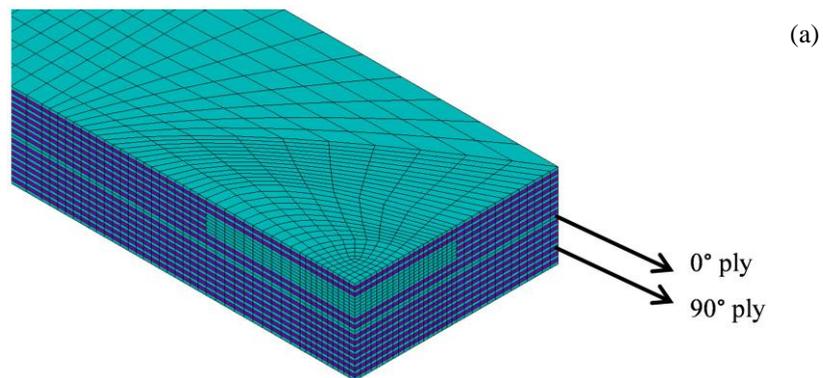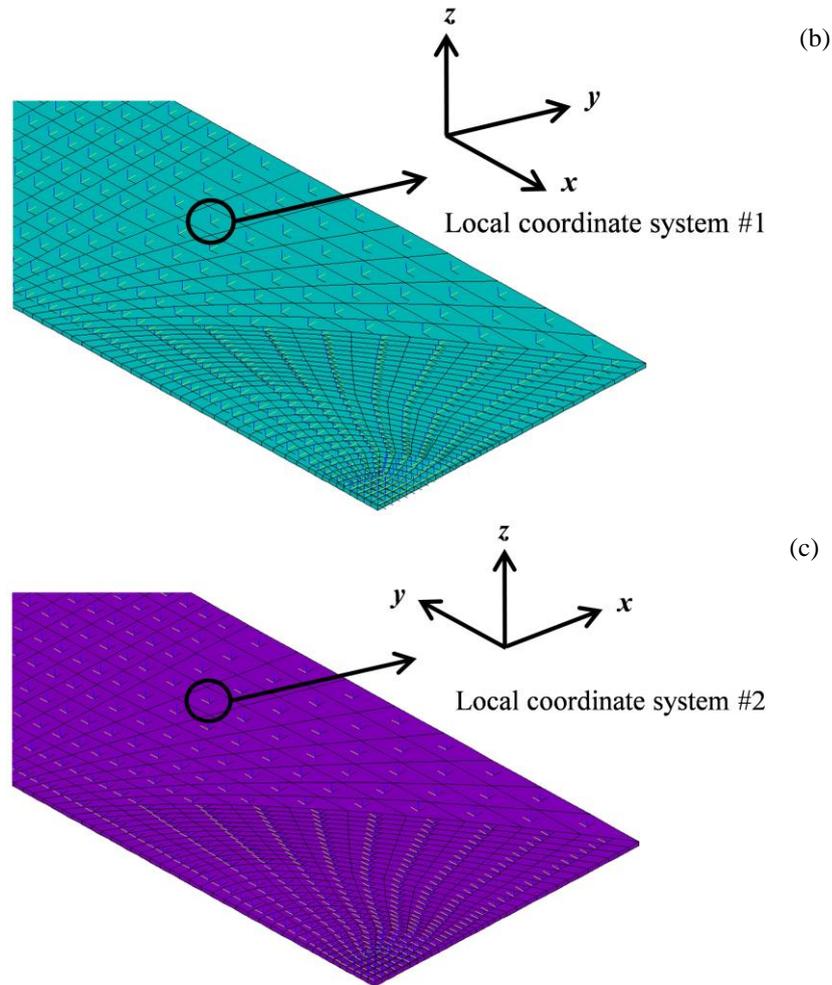
Fig. 4.5: The symmetrical cross-ply stacking sequence of the composite laminate: (a) 0° and 90° plies, (b) the local coordinate system defined for the 0º ply, and (c) the local coordinate system defined for the 90º ply.

The UD CFRP and the woven GFRP laminae as well as the PZT sensor were regarded as homogeneous and orthotropic, while the neat resin was considered as homogeneous and isotropic. The elastic properties of the different materials are listed in Table 4.3. The subscripts 1 and 2 of the elastic constants represent the longitudinal and transverse directions in the local coordinate system, respectively, and the subscript 3 denotes the through-thickness direction. The ultimate tensile (σ^t) and compressive (σ^c) strengths in each direction along with the shear strengths (S) are given in Table 4.4. All the materials were considered to deform within the elastic region.

Table 4.3: Material elastic properties.

Elastic properties	UD CFRP [36], [39]	woven GFRP [39], [40]	PZT sensor [35], [39]	neat resin [36], [39]
E_1, E_2, E_3 [GPa]	138.18, 9.8, 9.8	21, 21, 11.8	66, 66, 59	4.67
G_{12}, G_{23}, G_{13} [GPa]	4.12, 1.96, 4.12	3.5, 3.5, 3.5	41, 41, 41	1.73
$\nu_{12}, \nu_{23}, \nu_{13}$	0.35, 0.4, 0.35	0.07, 0.17, 0.17	0.389, 0.371, 0.371	0.35

Table 4.4: Material strength properties.

Strength properties	UD CFRP [36]	woven GFRP [36], [40]	PZT sensor [35]	neat resin [36]
$\sigma_1^t, \sigma_2^t, \sigma_3^t$ [MPa]	2207, 81, 81	440, 440, 121	75, 75, 75	121
$\sigma_1^c, \sigma_2^c, \sigma_3^c$ [MPa]	1531, 294, 294	440, 440, 121	700, 700, 700	294
S_{12}, S_{23}, S_{13} [MPa]	114, 114, 114	99, 99, 99	$10^6, 10^6, 10^6$*	99

* Because the shear strength properties of PZT sensor were not provided by the manufacturer, an assumed value was used in the simulation to avoid shear failure.

The symmetry constraints were assigned to the areas at the global coordinates of x = 75 mm and z = 13 mm (Fig. 4.6). At the bottom surface of the model (at the global coordinate of x = 15 mm, y = 0), the supports were considered as displacement constraint in y-direction ($u_y = 0$) (Fig. 4.6). The displacement-controlled loading applied via the crosshead was considered as the input of nodal displacement (w_{FE}). On the top surface of the model, w_{FE} was assigned to the nodes at the global coordinate of x = 55 mm, y = 0.54 mm (Fig. 4.6).
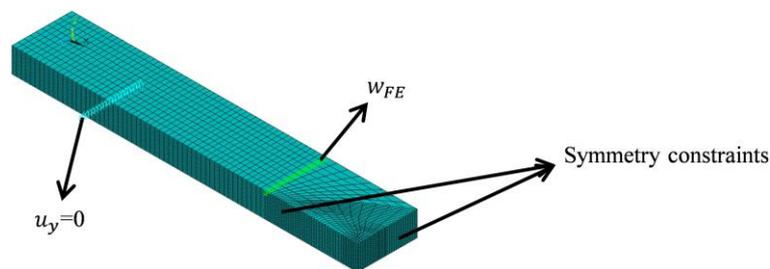
Fig. 4.6: The boundary conditions and nodal displacements.

As the first step, the mesh convergence study has been conducted for the FE model of composite laminate with embedded small sensor. Two meshing schemes A and B, with the total number of elements 16290 and 28050, respectively, are compared in terms of the local strains (ε_x, ε_y and ε_{xy}) of the sensor elements. The displacement-controlled loading (w_{FE}) of -0.25 mm was applied to the models, and the plots of local strain are given in Fig. 4.7. Besides, the same method has been applied to the mesh convergence study of the other FE models (Figs. 4.8, 4.12 and 4.13). The convergence studies show that the meshing schemes used in this research can provide accurate simulation results.

Fig. 4.7: The mesh convergence study of the FE model of composite laminate with embedded small sensor (on the compression side): (a) ε_x of sensor elements, (b) ε_y of sensor elements, and (c) ε_{xy} of sensor elements.

4.3.2. MATERIAL PROPERTY DEGRADATION METHOD

The failure of a fibre reinforced composite laminate is a gradual process. The material property degradation (MPDG) method has been used to model the progressive damage accumulation [41]. It consists of two parts: failure identification and stiffness degradation. Four failure modes (longitudinal tensile/compressive failure, and transverse tensile/compressive failure) are accounted for. According to Chiu theory [32], the stiffness of the damaged element immediately degrades once a particular failure mode is identified.

The maximum stress criteria were employed to detect the onset of damage and the specific damage mode. As given in Eqs. 4.1 to 4.4, the failure occurs if the stress magnitude in one direction exceeds the corresponding strength.

Longitudinal tensile failure ($\sigma_1 \geq 0$):

$$\frac{\sigma_1}{\sigma_1^t} \geq 1. \tag{4.1}$$

Longitudinal compressive failure ($\sigma_1 < 0$):

$$\frac{|\sigma_1|}{\sigma_1^c} \geq 1. \tag{4.2}$$

Transverse tensile failure ($\sigma_2 \geq 0$):

$$\frac{\sigma_2}{\sigma_2^t} \geq 1. \tag{4.3}$$

Transverse compressive failure ($\sigma_2 < 0$):

$$\frac{|\sigma_2|}{\sigma_2^c} \geq 1. \tag{4.4}$$

Upon reaching the onset of damage, the constitutive relation of the damaged element is applied [33]:

$$\varepsilon = C_d \sigma, \tag{4.5}$$

where C_d is the damaged compliance matrix. For the general orthotropic material, it is defined as:

$$C_d = \begin{bmatrix} \frac{1}{E_1} \cdot \frac{1}{1-d_1} & -\frac{v_{21}}{E_2} & -\frac{v_{31}}{E_3} & & & \\ -\frac{v_{12}}{E_1} & \frac{1}{E_2} \cdot \frac{1}{1-d_2} & -\frac{v_{32}}{E_3} & & 0 & \\ -\frac{v_{13}}{E_1} & -\frac{v_{23}}{E_2} & \frac{1}{E_3} \cdot \frac{1}{1-d_2} & & & \\ & & & \frac{1}{G_{12}} \cdot \frac{1}{1-d_{12}} & 0 & 0 \\ & 0 & & 0 & \frac{1}{G_{23}} \cdot \frac{1}{1-d_{12}} & 0 \\ & & & 0 & 0 & \frac{1}{G_{13}} \cdot \frac{1}{1-d_{12}} \end{bmatrix}, \tag{4.6}$$

where d_1, d_2 and d_{12} are the stiffness degradation coefficients, and

$$d_{12} = 1 - (1 - d_1)(1 - d_2). \tag{4.7}$$

The degradation coefficients were initially set as 0, and they were not triggered until a failure criterion is satisfied. At that point, the values defined in next section were used. Considering the different failure mechanisms and different damage effects resulted from tension and compression, d_1 and d_2 are separated into d_1^t, d_1^c, d_2^t and d_2^c.

Due to the perfect bonding assumption, delaminations are not captured by the model but a shear stress check was done in the vicinity of the sensors:

$$\frac{|\tau|}{S} \geq 1. \tag{4.8}$$

The shear stresses were investigated at the load of 8000 N (which is approximately equal to the final failure loads recorded in tests). For the FE model with embedded small sensor (Fig. 4.4), the ratio of out-of-plane shear stress (τ_{xy}) and corresponding strength (S_{13}) and the ratio of in-plane shear stress (τ_{xz}) and corresponding strength (S_{12}) are plotted as a function of the x-coordinate of selected nodes (Fig. 4.8). The ratios for selected nodes in the FE model with embedded large sensor (Fig. 4.15) are plotted in Fig. 4.9. Because the shear strength of PZT sensor is unknown, the ratio is not plotted in the range of $71.5 \leq x \leq 75$ mm (Figs. 4.8(a) and (b)) and $65 \leq x \leq 75$ mm (Figs. 4.9(a) and (b)) which are the ranges covered by the sensors. For the case of the smaller sensor, it can be seen that the magnitude of the out-of-plane shear stress does not exceed 35% of the transverse shear strength of the material (Fig. 4.8(a)). Therefore, the transverse shear failure, which could eventually lead to delamination, is not expected to occur during the load excursion. On the other hand, as can be seen from Fig. 4.9(a), the transverse shear stress is approximately 80% of the material shear strength for the case of the larger sensor, suggesting that delaminations are possible near the final failure load. Such delaminations were, indeed, observed during the tests. For both cases of the small and large sensor, the magnitude of the in-plane shear stress does not exceed 3% of the material shear strength (Figs. 4.8(b) and 4.9(b)). Therefore, the in-plane shear failure is unlikely to occur during the load excursion.

(b)

(c)

Global coordinate system

1) Global coordinates of the selected nodes at bottom of ply 23:
   x = 57-71.5 mm, y = 3.96 mm, z = 13 mm
2) Global coordinates of the selected nodes at top of ply 23:
   x = 57-71.5 mm, y = 4.14 mm, z = 13 mm
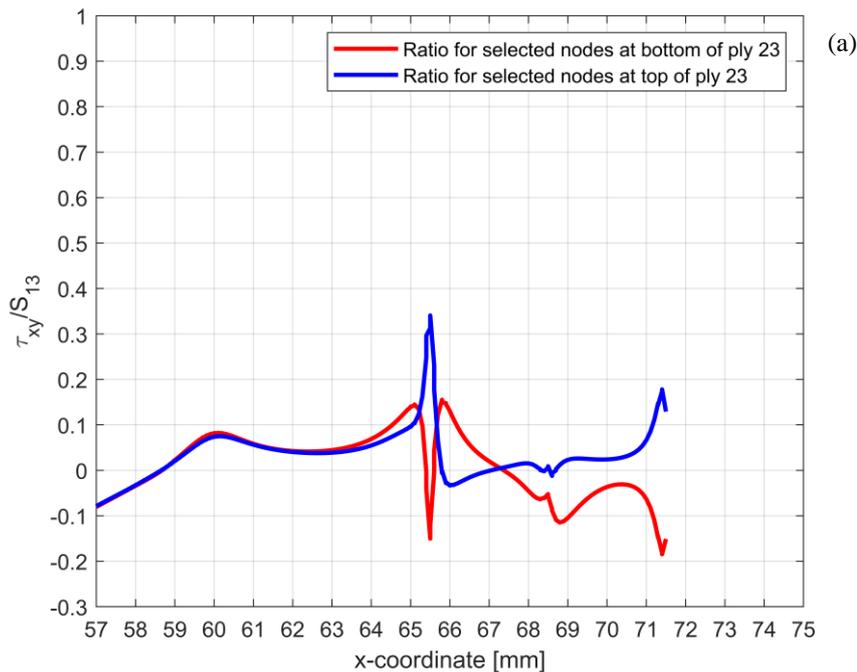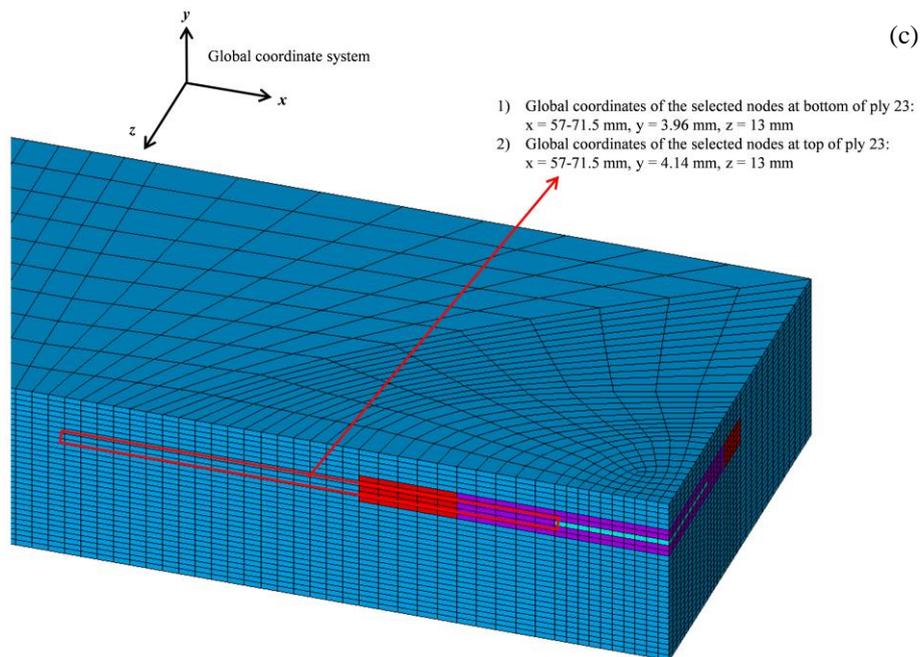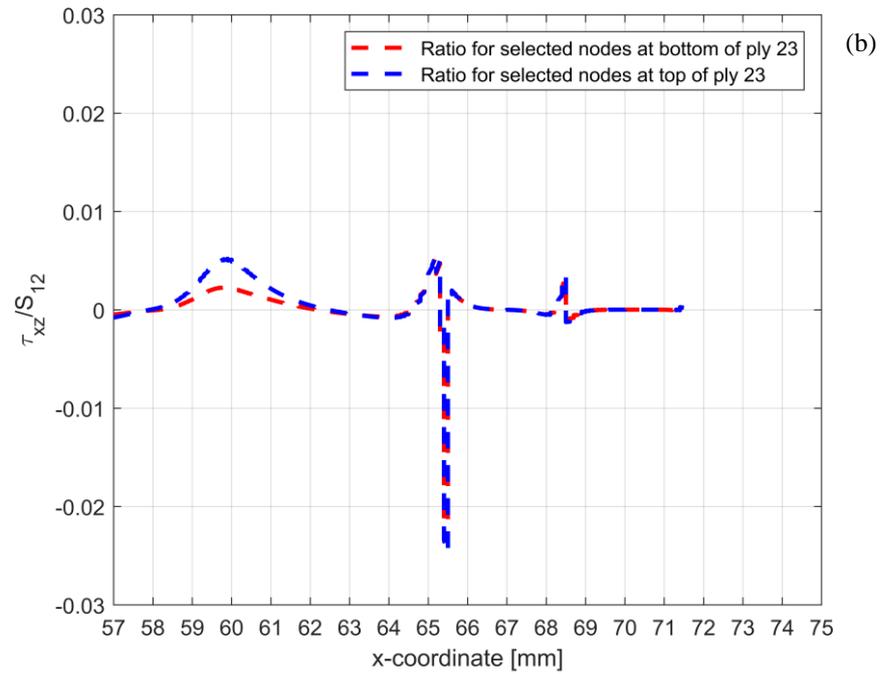
Fig. 4.8: (a) The ratio of nodal out-of-plane shear stress and corresponding strength, (b) the ratio of nodal in-plane shear stress and corresponding strength, and (c) the location of selected nodes in the FE model with embedded small sensor.

(a)

(b)
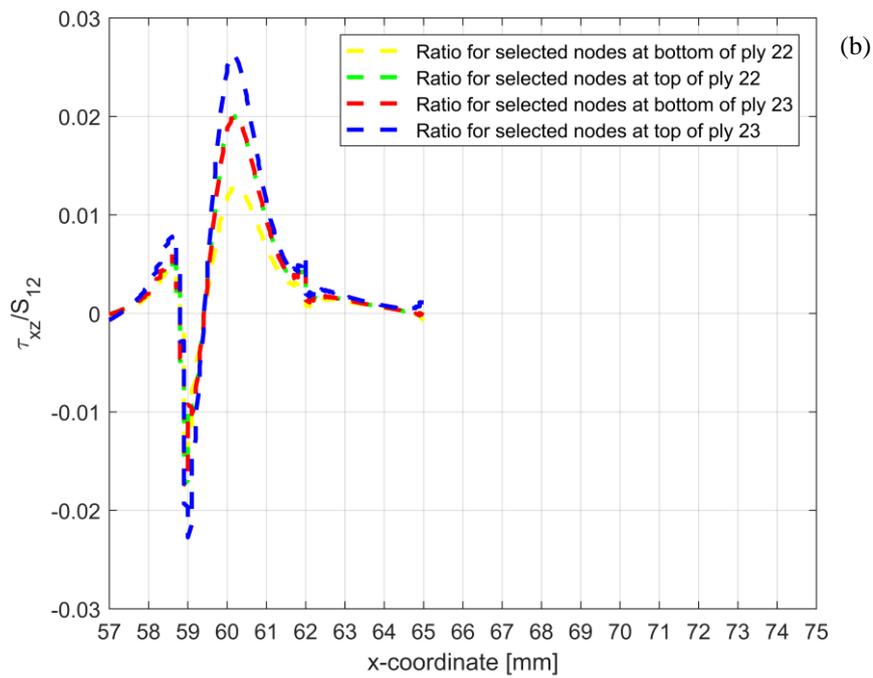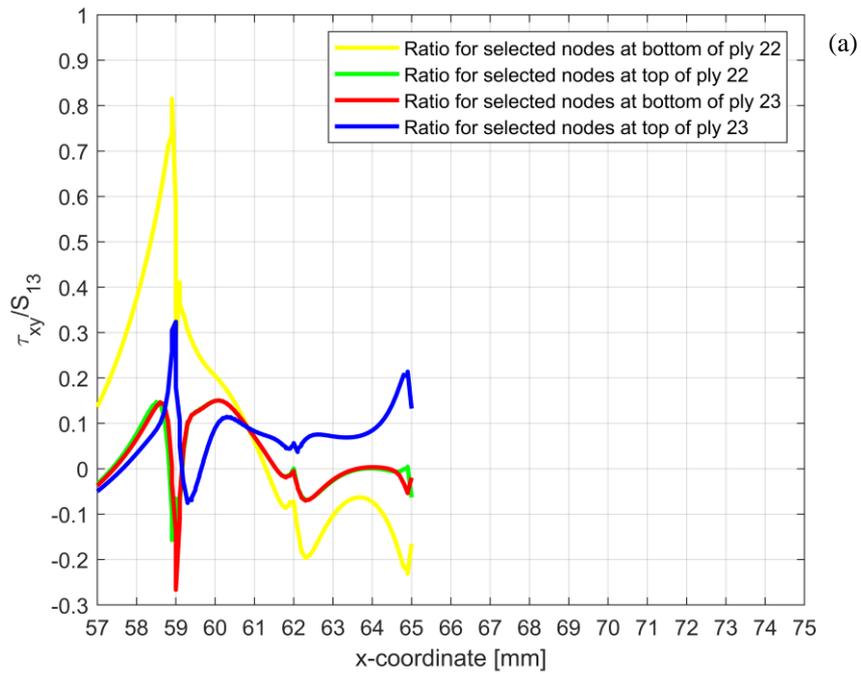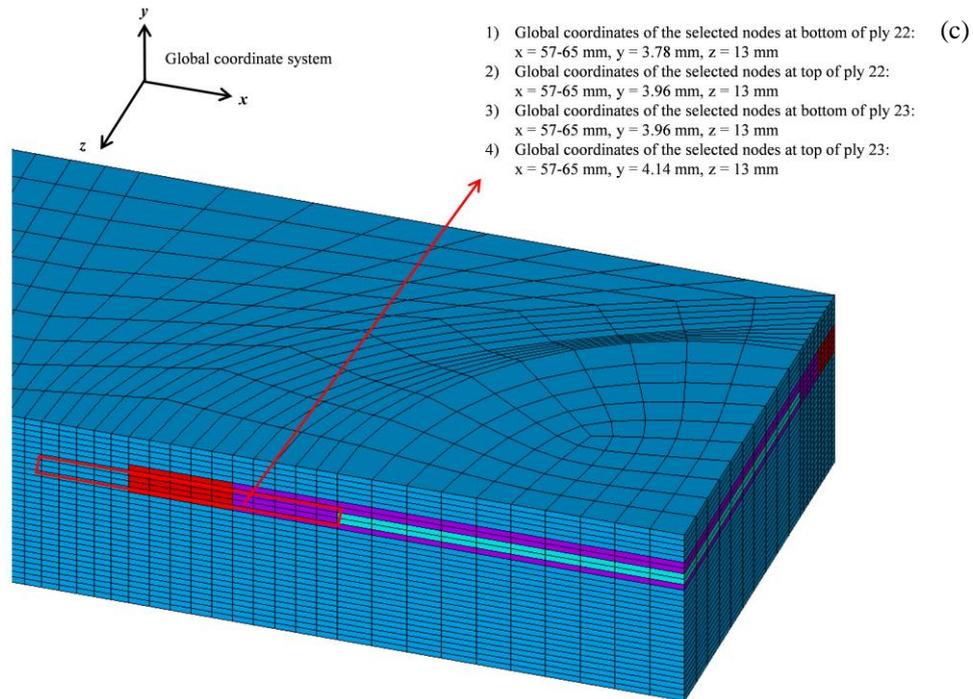
Fig. 4.9: (a) The ratio of nodal out-of-plane shear stress and corresponding strength, (b) the ratio of nodal in-plane shear stress and corresponding strength, and (c) the location of selected nodes in the FE model with embedded large sensor.

4.4. EXPERIMENTAL RESULTS AND DISCUSSION

4.4.1. STIFFNESS DEGRADATION MECHANISM

4.4.1.1. DETERMINING STIFFNESS DEGRADATION COEFFICIENTS

To validate the MPDG method and determine the appropriate degradation coefficients, first the progressive failure analysis (PFA) was carried out with the pristine laminate model (without embedded sensor), and compared with corresponding experimental records. As shown in Fig. 4.10(a), each ply was modelled by one element in the thickness direction. In the x-z plane, the short and long edges were equally divided into 13 and 75 elements, respectively. The total number of elements was therefore 29250. The perfect bonding assumption held for the model. For the 0º and 90º plies in the symmetrical lay-up configuration (Fig. 4.10(b)), the two different local coordinate systems were defined in the same way as in Fig. 4.5. In Fig. 4.10(c), the symmetry constraints and the nodal displacements ($u_y = 0$ applied to represent the displacement constraint, and w_{FE} applied to represent the displacement-controlled loading) were defined in the same way as in Fig. 4.6.
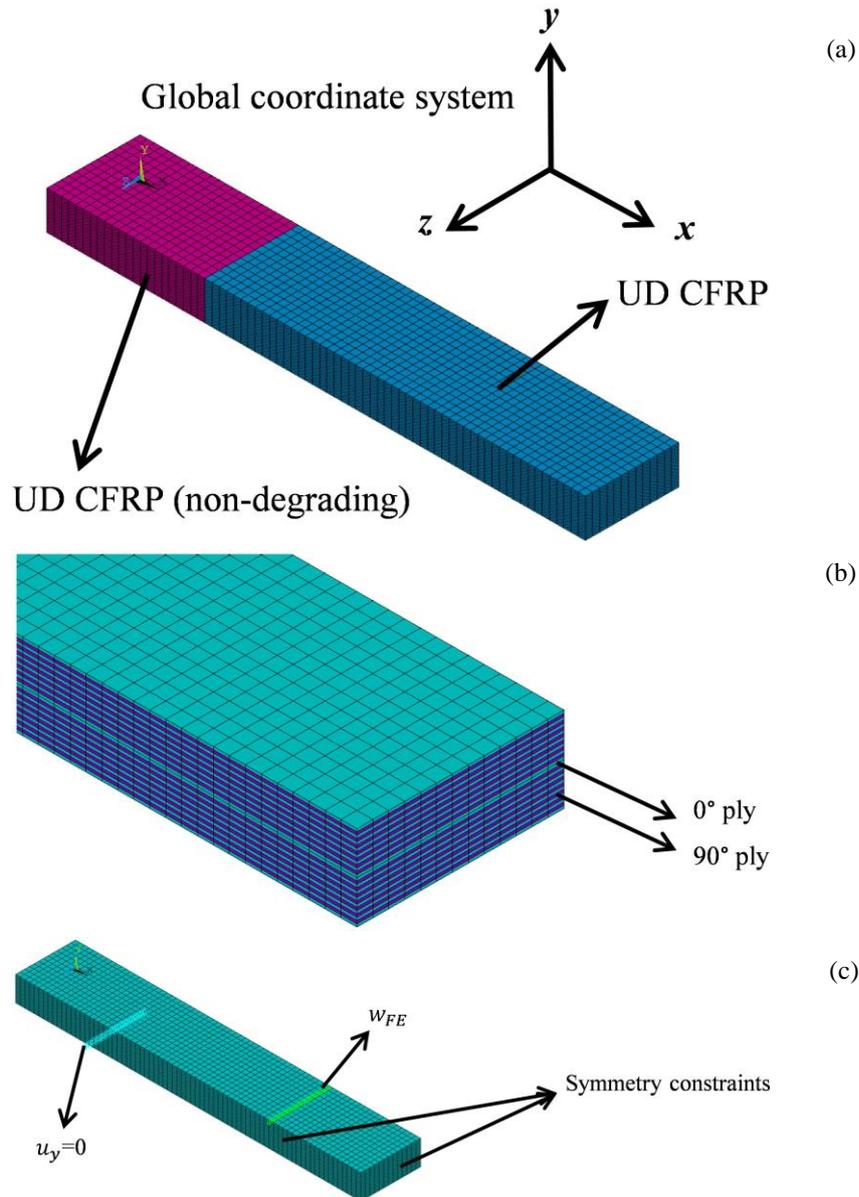
Fig. 4.10: The FE model of the pristine laminate: (a) the overview of the FE model, (b) the symmetrical lay-up configuration of the pristine laminate, and (c) the boundary conditions and nodal displacements.

The PFA was carried out by using the MPDG method with w_{FE} increasing from 0 to -10 mm in steps of -0.25 mm. As for the UD CFRP material, four damage modes, i.e., fibre tension, fibre compression, matrix tension and matrix compression, were identified by the maximum stress criteria (Eqs. 4.1 to 4.4). The failed element would suffer an instant stiffness reduction (Eqs. 4.5 to 4.7) once a failure criterion was satisfied. The damage resulted from different failure modes was represented by the magnitude of different degradation coefficients. For example, it has been considered that the tensile fibre or matrix failure would lead to the complete loss of tension resistance. Therefore, d_1^t and d_2^t have been (initially) taken as 0.9 (not taking as 1 to avoid the numerical instability resulting from Eq. 4.6). Because a ply in the bonded laminate has been considered to maintain the most of its capability to resist compression after the initiation of compressive failure, d_1^c and d_2^c have been (initially) taken as 0.1. The degradation coefficients would be updated based on the experimental results. The coefficient is applied

114

at the onset of the corresponding failure mode. Thereafter the degraded stiffness remains constant, representing irreversible failure process.

Because the support was considered as displacement constraints on nodes ($u_y = 0$ in Fig. 4.10(c)), it would result in stress concentration. To alleviate this stress concentration effect, the degradation coefficients have been taken as 0 (Set 1 in Table 4.5) for all the elements between $0 \leq x \leq 22$ mm (the non-degrading elements in Fig. 4.10(a)). This has been consistently applied to all models presented in this research (Figs. 4.4(a), 4.14(a) and 4.15(a)).

Table 4.5: Stiffness degradation coefficients.

Set	d_1^t	d_1^c	d_2^t	d_2^c
1	0	0	0	0
2	0.9	10^{-4}	10^{-4}	10^{-4}

At each load step, the failure state of each ply has been plotted to record the failure development. The resulting failure history is presented in Fig. 4.11 according to the records. Each ply in the symmetrical lay-up configuration is numbered from bottom to top. The red bar and the blue bar represent the failure initiated and developed in the 0º ply and the 90º ply, respectively. For example, the failure onset was captured at ply 30 (0° ply), ply 2 (90° ply), ply 29 (90° ply) and ply 1 (0° ply) for the first time when w_{FE} is -4.5 mm, -5 mm, -6.75 mm, and -8.25 mm, respectively.

During the loading process, the top plies of the laminate are under compression. Compared to the longitudinal elastic modulus (fibre-dominated) of the UD CFRP material, the transverse elastic modulus (matrix-dominated) is much smaller (Table 4.3), i.e., the compressive stress in the 90º ply is generally much lower than the neighbouring 0º ply. Therefore, it can be observed that most of the 90º plies at the top of the laminate do not fail under compression, but the 0º plies experience longitudinal compressive failure. At the bottom of the laminate, the tensile stress in the 90º ply is in principle much lower than the neighbouring 0º ply as well. However, it is observed that many 90º plies fail much earlier. This is owing to the much smaller tensile strength in the transverse direction (Table 4.4).

The four experimental records of the four-point bending tests with the pristine laminate specimens are shown in Fig. 4.12, where the x-axis is the displacement of the crosshead (w_m), and the y-axis is the total amount of force applied via the crosshead (F_{LC}). It can be observed that F_{LC} increases approximately linearly when w_m is small, and the load drops happen when w_m approaches 8 mm. Considering the failure history at each ply of the pristine laminate model (Fig. 4.11), therefore, it can be concluded that the fibre compressive failure (e.g. at ply 30), matrix tensile failure (e.g. at ply 2), and matrix compressive failure (e.g. at ply 29) have very limited effect on the degradation of the specimen bending stiffness, while the fibre tensile failure (e.g. at ply 1) plays an important role. Accordingly, the degradation coefficients d_1^c, d_2^t and d_2^c have been updated to 10^{-4}, while d_1^t has been remained as 0.9 (Set 2 in Table 4.5).
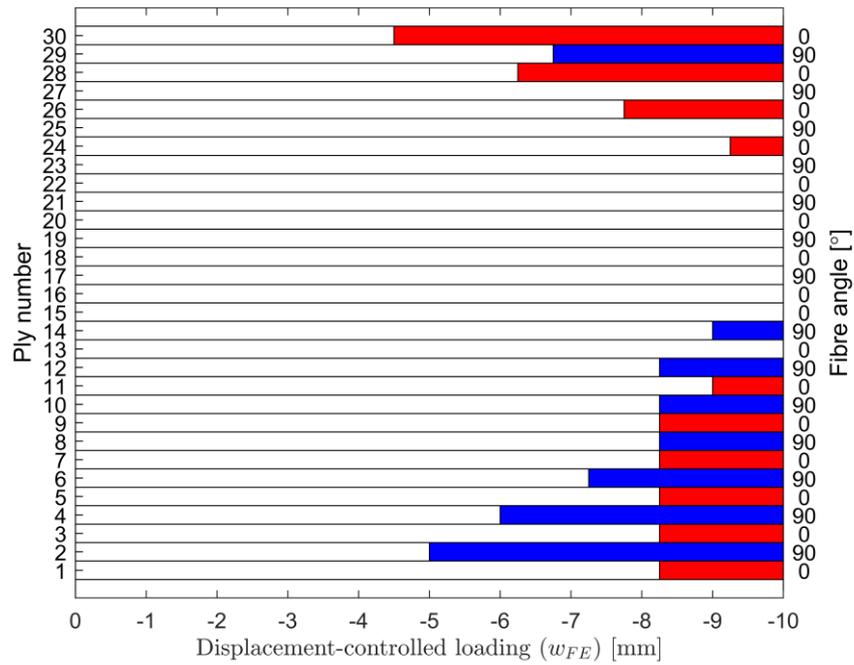
Fig. 4.11: The failure history at each ply of the pristine laminate model.
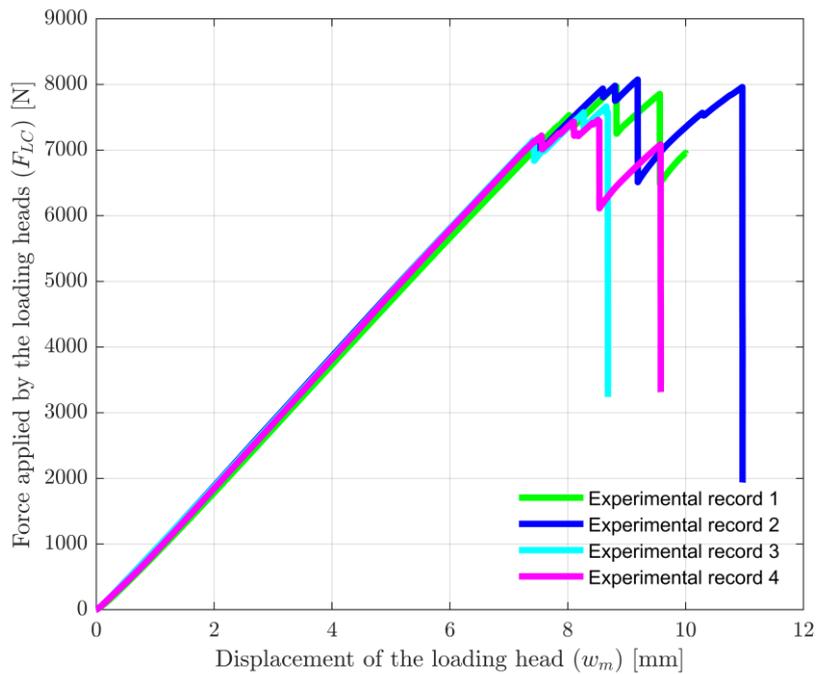
Fig. 4.12: Experimental records of the four-point bending test of pristine laminate specimens.

4.4.1.2. PFA OF PRISTINE LAMINATE MODEL

The PFA has been carried out with the pristine laminate model by using the degradation coefficients in Table 4.5. For all the loaded nodes, the sum of the reaction forces in global y-direction (R_y) were calculated at each load step. Because a quarter of the laminate was modelled, the total applied load becomes: $F_{FE} = -2R_y$. F_{FE} is plotted as a function of the displacement-controlled loading (w_{FE}) in Fig.

116

4.13(a). It can be seen that the load increases approximately linearly when the displacement increases from 0 to 8 mm, which means that the global bending stiffness of the FE model is not significantly disrupted by the failure accumulation yet. A load drop is observed when the displacement exceeds 8 mm, and the load continues to grow with increasing displacement. The four experimental records are included in the figure as well, so the FE analysis result fits well with the records in the range of displacement between 0 and 8 mm. Also, the first significant load drop predicted by the FE analysis correlates very well with the experimentally observed first load drop. When the crosshead displacement was higher, delaminations occurred during the tests which accelerated final failure. However, these were not captured by the FE model because of the perfect bonding assumption. Therefore, the load resulted from numerical simulation after first damage increased to higher values than experimentally observed.

The slope of the curves in Fig. 4.13(a) represents the bending stiffness. Before the first load drop happens, i.e., $w_{FE} < 8$ mm, the slope of the force-displacement curve of the PFA results was calculated at each data point. For each experimental record, the slope was calculated at the interval of 100 data points. In the beginning of the loading process, the pristine laminate model turns out to be stiffer than the experimental specimens because of larger slope value (Fig. 4.13(b)). This can be owing to the way the displacement-controlled loading applied to the model (Fig. 4.10(c)), where the nodal loads are applied in a line. But there is a good correlation between the bending stiffness of the FE model and that of the experimental specimens with increasing displacement, and the slope is about 970 N/mm.
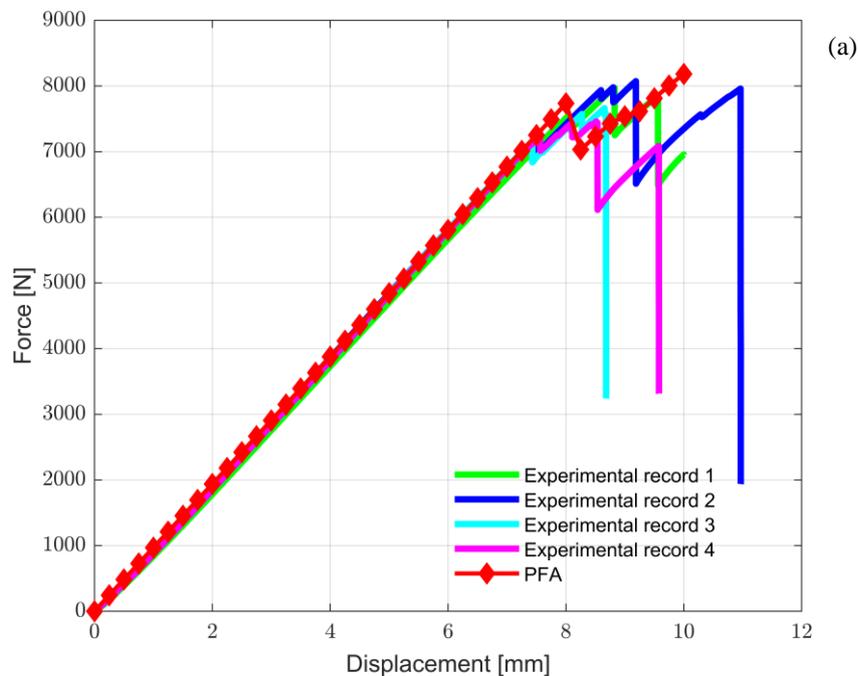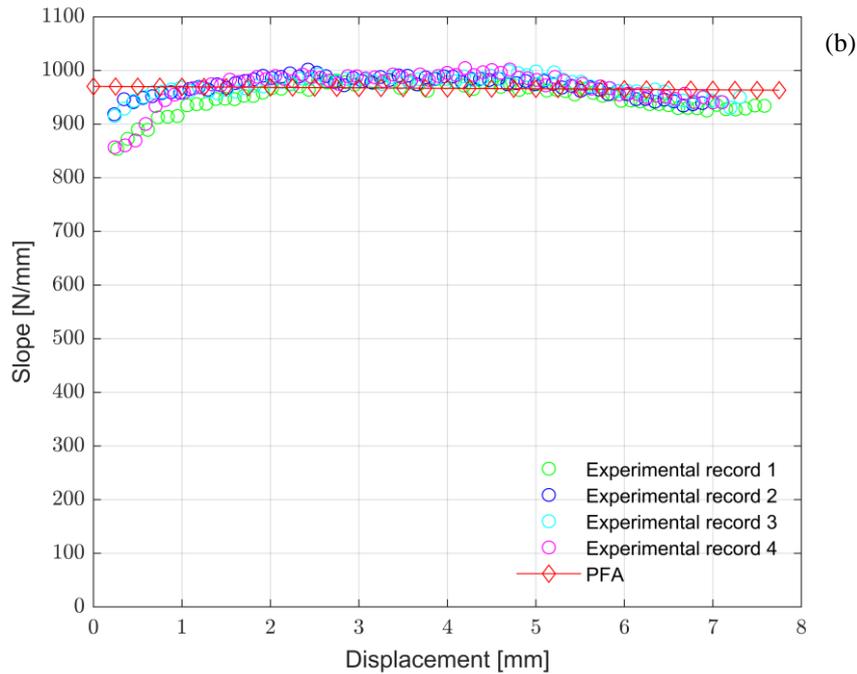
Fig. 4.13: Comparing the PFA of pristine laminate model and the experimental records: (a) force-displacement relations, and (b) the slopes.

4.4.1.3. PFA OF COMPOSITE LAMINATE MODELS WITH EMBEDDED SENSORS

The FE modelling method has also been employed to build the composite laminate models with embedded small sensor on the tension side (Fig. 4.14), and with large sensor (only) on the compression side (Fig. 4.15). The mesh density in Fig. 4.14(a) is the same as in Fig. 4.4(a), with the addition that the PZT sensor is implanted at ply 8 (Fig. 4.14(b)). In Fig. 4.15(a), the smallest element size is 0.5 mm and 0.3 mm in x and z directions, respectively. Each ply was modelled by one element in the thickness direction. Therefore, the total number of elements was 24150. As shown in Fig. 4.15(b), the large sensor is implanted between ply 22 and 23.
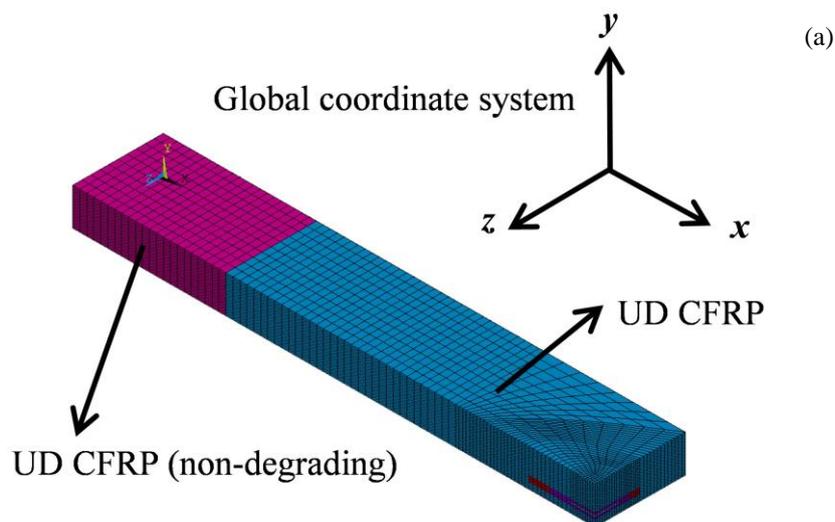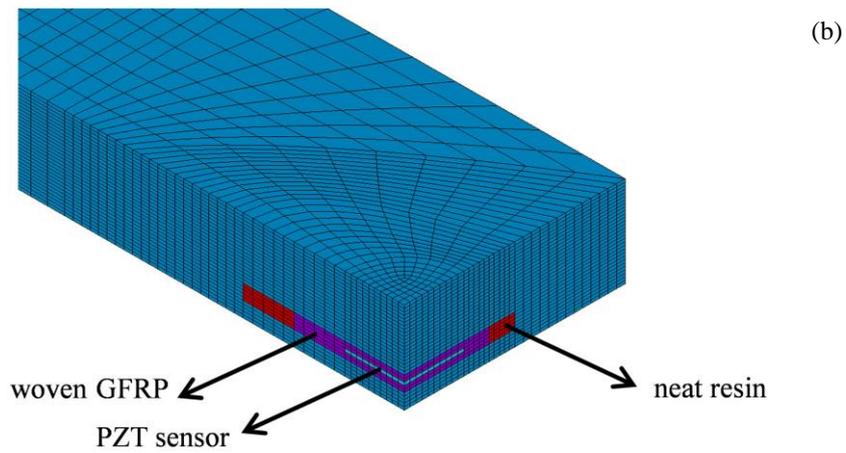
Fig. 4.14: The FE model of the composite laminate with embedded small sensor (on the tension side): (a) the overview of the FE model, and (b) the detail view of the PZT sensor (embedded at ply 8) and the insulation materials.
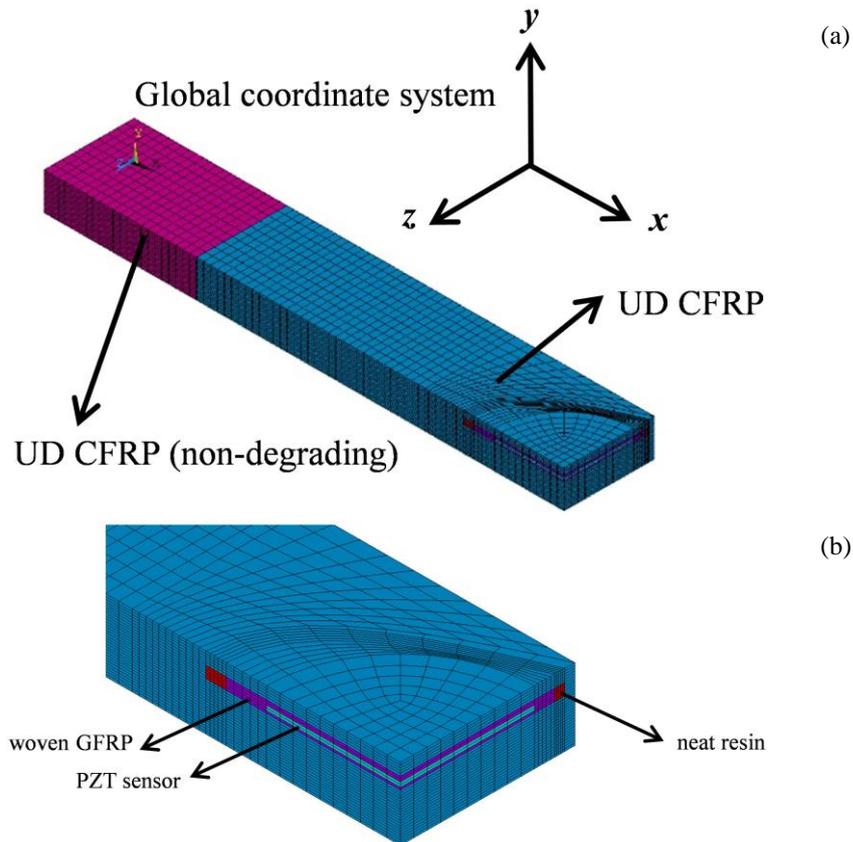
Fig. 4.15: The FE model of the composite laminate with embedded large sensor (on the compression side): (a) the overview of the FE model, and (b) the detail view of the PZT sensor (embedded at ply 22 and 23) and the insulation materials.

The MPDG method have next been applied in the PFA of the three composite laminate models with embedded sensors. Together with the corresponding experimental records, the force is plotted as a function of the displacement-controlled loading in Figs. 4.16(a), 4.17(a) and 4.18(a). Within the monotonically increasing range of the force, the slopes of the curves are calculated in the same way as in Fig. 4.13(b), and are presented in Figs. 4.16(b), 4.17(b) and 4.18(b), respectively.

For the FE model of the composite laminate with embedded small sensor on the compression side, there is a good correlation between the flexural stiffness of the model and that of the specimens. This claim is supported by the comparable value of the slopes (about 960 N/mm) in Fig. 4.16(b). In the beginning of the loading process, the experimental specimens turn to be softer than the numerical model because of the smaller slope value. It has been observed also in Fig. 4.13(b), and the reason behind that is given in last section. The first load drop in FE prediction, due to fibre tensile failure, is very close to the experimental failure loads. Therefore, the first significant failure is well captured by FE analysis. The final failure of the specimen was not captured in the FE analysis (Fig. 4.13(a)) because delaminations were not accounted for.
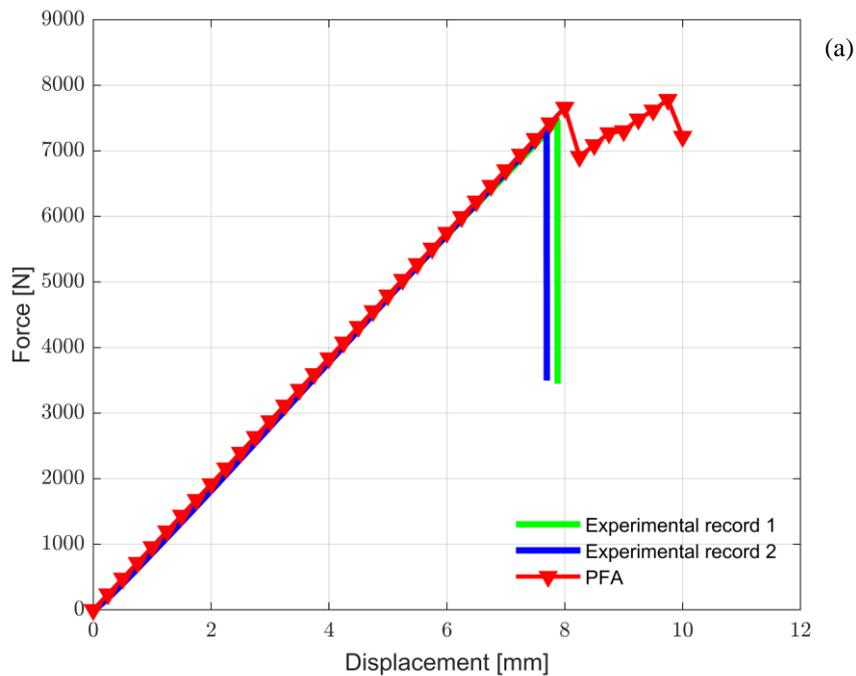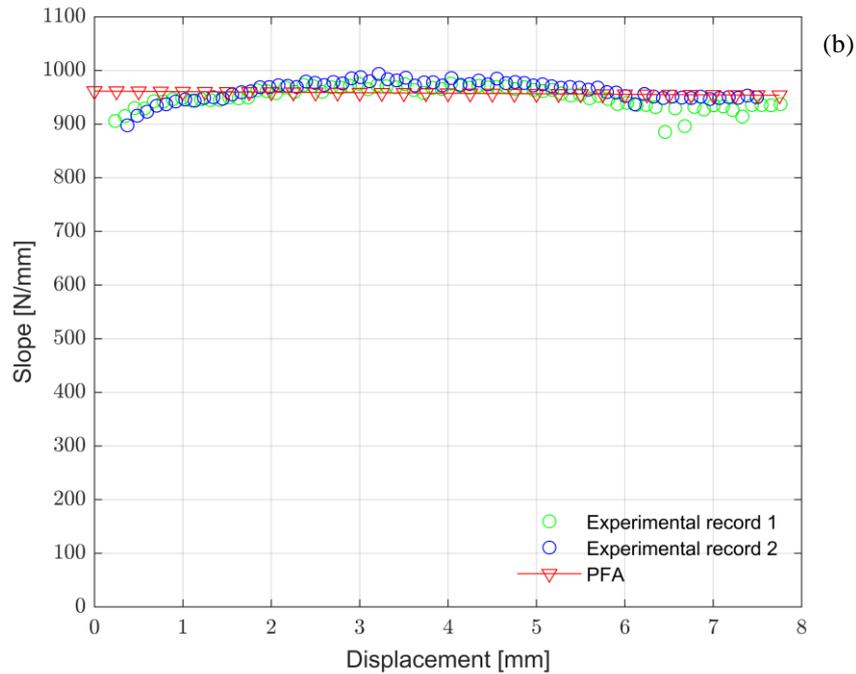
Fig. 4.16: Comparing the PFA of composite laminate model with embedded small sensor (on the compression side) and the experimental records: (a) force-displacement relations, and (b) the slopes.

In contrast to the experimental record 2 in Fig. 4.17(a), the experimental record 1 does not show apparent load drop before final failure. This exceptional record suggests that there was no significant fibre tensile failure during the loading process. However, the first load drop in FE prediction correlates well with the first load drop in experimental record 2. The comparable value of slopes in Fig. 4.17 (b) is about 960 N/mm.

121
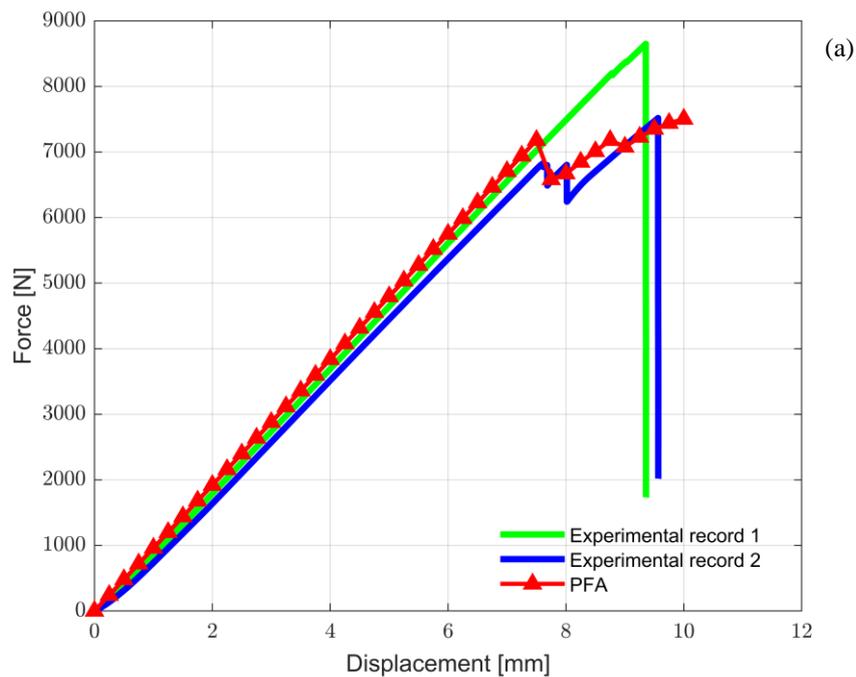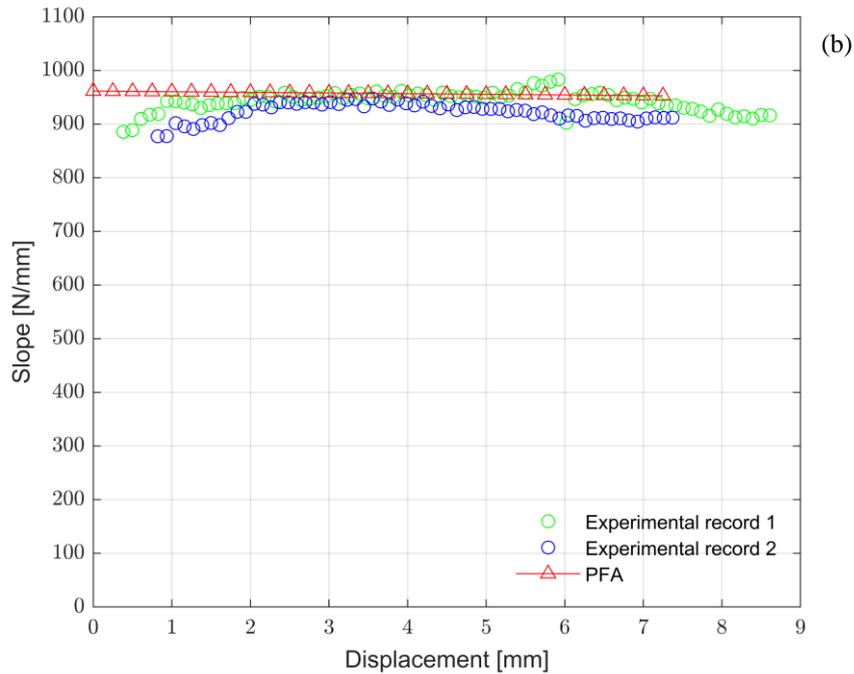
Fig. 4.17: Comparing the PFA of composite laminate model with embedded small sensor (on the tension side) and the experimental records: (a) force-displacement relations, and (b) the slopes.

The FE model of the composite laminate with embedded large sensor turns out to be stiffer than the experimental specimens. As shown in Fig. 4.18(b), the slope of the force-displacement curve of the PFA results is about 3-8% higher than that of the experimental records. It means the specimen stiffness has been overestimated by the FE model. It is suspected that the specimen width and thickness defined at FE model are slightly larger than the actual size, contributing to over-estimation of specimen bending stiffness. Because only two specimens with embedded large sensor have been tested, more experimental data are required before drawing conclusion.
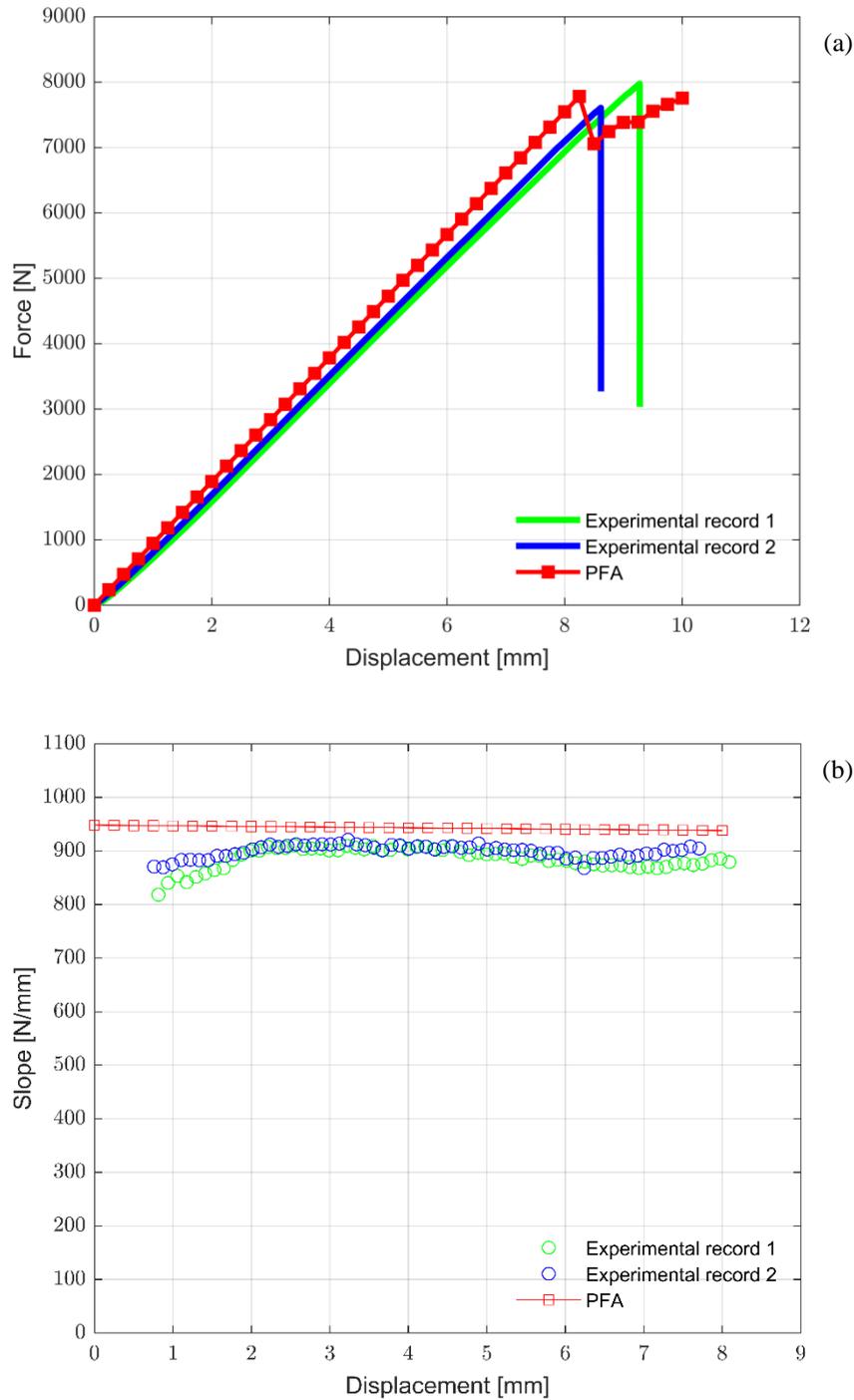
Fig. 4.18: Comparing the PFA of composite laminate model with embedded large sensor (on the compression side) and the experimental records: (a) force-displacement relations, and (b) the slopes.

4.4.2.   FINAL FAILURE MECHANISM

Comparing the experimental records of the composite laminate with embedded small sensor on the compression side and on the tension side, it can be found that the two types of specimen have similar stiffness (Figs. 4.16(b) and 4.17(b)), while the specimens with embedded small sensor on the compression side have failed earlier. As shown in Fig. 4.16(a), the specimen failures were recorded at

123

the crosshead displacement of about 8 mm. In contrast to the assumption of perfect bonding in the FE models, in fact, the embedded sensor, the insulation and bonding materials, and the bifilar cable could introduce defects in the specimens during manufacturing procedure. When the sensor was embedded on the compression side, the defects propagated more quickly during loading process, which resulted in delaminations (Fig. 4.19(a)) and adversely affected the specimen integrity. When the small sensor was embedded on the tension side, the specimen failure was recorded at the crosshead displacement of about 9.5 mm (Fig. 4.17(a)). In this case the crack propagation and the consequent delaminations were initially arrested, but the final failure was again driven by the delaminations (Fig. 4.19(b)).

Considering the position of the large sensor, the composite specimens with embedded large sensor have behaved similarly to the specimens with embedded small sensor on the compression side. While the pristine laminates have behaved in the similar way as the laminates with embedded small sensor on the tension side, because they failed at larger crosshead displacements (Fig. 4.18(a)). The delaminations in the failed specimens are presented in Figs. 4.19 (c) and (d), respectively.
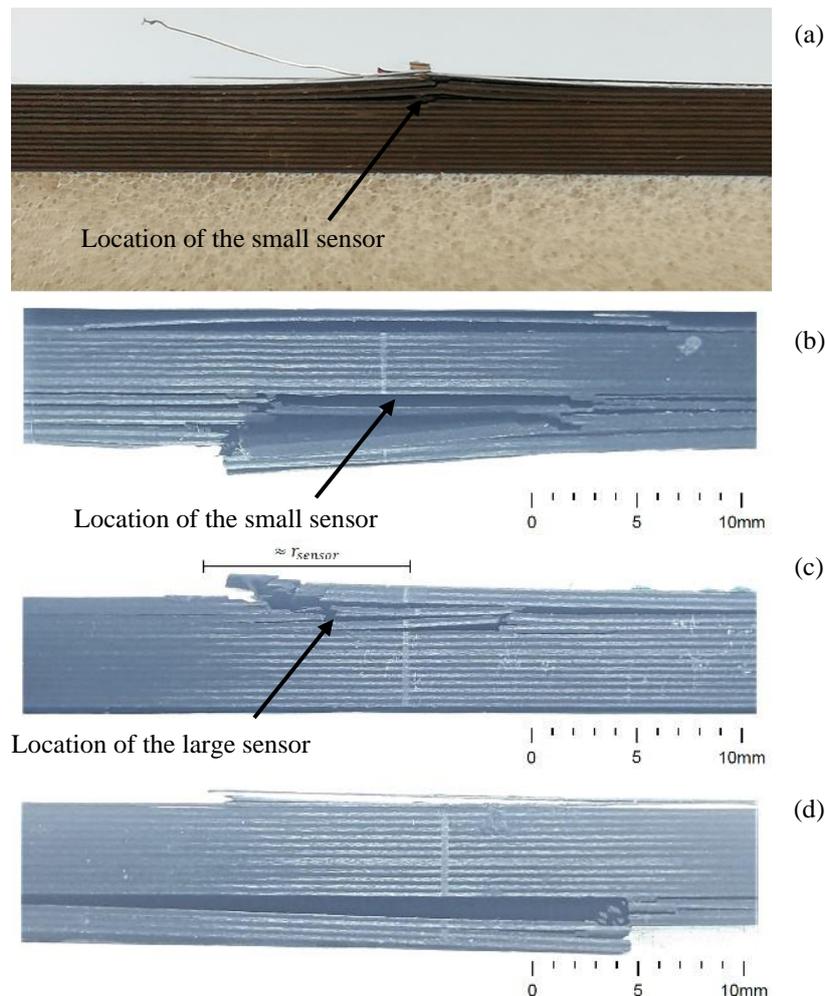
Fig. 4.19: Delaminations occurred in (a) the composite laminate with embedded small sensor (on the compression side), (b) the composite laminate with embedded small sensor (on the tension side), (c) the composite laminate with embedded large sensor (on the compression side), and (d) the pristine laminate.

4.4.3. THE EFFECT OF GFRP AND RESIN ON THE BENDING STIFFNESS

For the FE model of the composite laminate with embedded small or large sensor (on the compression side), the dimensions of the insulation materials (in x-z plane of the global coordinate system) are shown in Figs. 4.20 and 4.21, respectively. The dimensions of woven GFRP fabric in x- and z-directions are denoted as l_{G1} and l_{G2}, respectively. The dimensions of neat resin in x- and z-directions are denoted as l_{R1} and l_{R2}, respectively. The effect of in-plane dimensions of insulation materials on the global bending stiffness has been investigated, for example, considering the composite model with embedded small sensor, and decreasing the in-plane dimensions of GFRP material by 1/3 (Fig. 4.22). The load-controlled displacement of 1 mm has been applied to the new model. Because no failure has been recorded when the displacement is 1 mm (Fig. 4.11), the linear static analysis (rather than PFA) has been performed with the new model. The slope of the displacement-force relation line, going through the origin, was subsequently calculated. The slope variations due to tuning the in-plane dimensions of insulation materials were studied in the same way and are shown in Table 4.6. It can be observed that the material dimensions have negligible effect on the bending stiffness of the FE models. The effect of stiffness properties (E, ν) of insulation materials on the global bending stiffness has been investigated as well. The material stiffness decreased by 5%, 10%, 15% and 20%, and the slope of the resulted displacement-force relation curves were studied in same way and are given in Table 4.7. Apparently, the bending stiffness of the models are not affected. Because of the relatively limited use of insulation materials, they have little effect on the global bending stiffness.
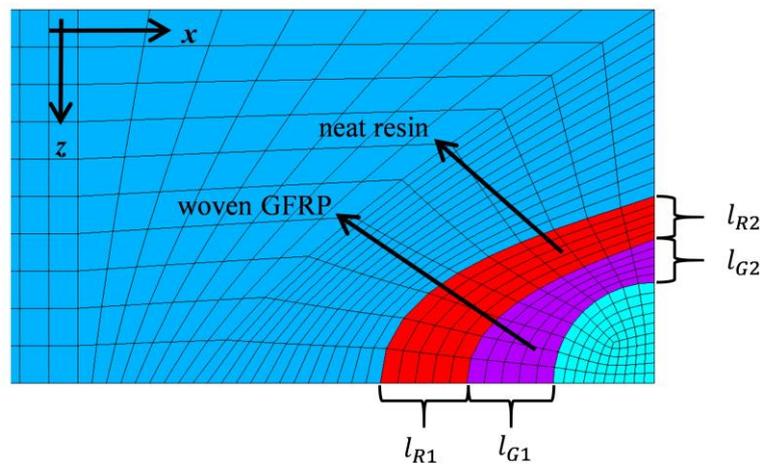
Fig. 4.20: In-plane dimensions of GFRP and resin in the composite laminate model with embedded small sensor.
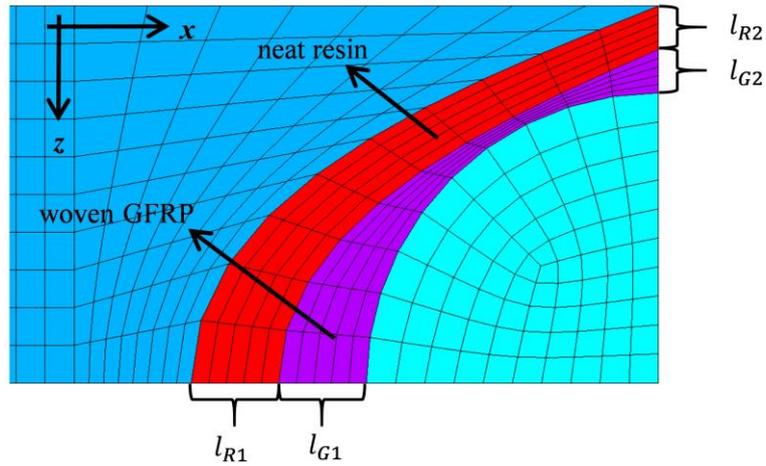
Fig. 4.21: In-plane dimensions of GFRP and resin in the composite laminate model with embedded large sensor.
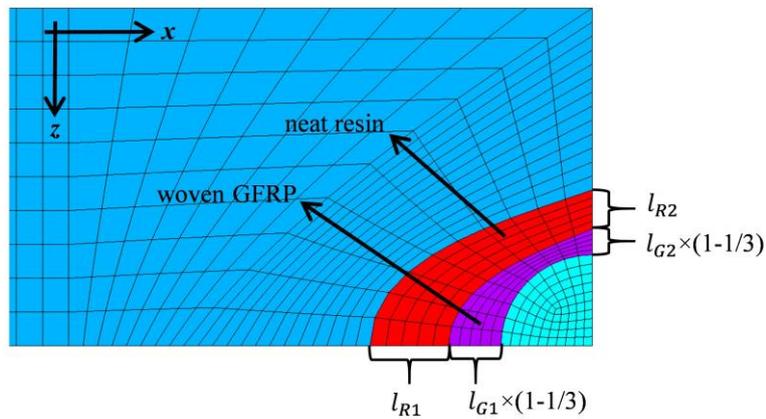
Fig. 4.22: Tuning the in-plane dimensions of GFRP material for the composite laminate model with embedded small sensor: l_{G1} and l_{G2} decrease by 1/3.

Table 4.6: The effect of in-plane dimensions of GFRP and resin on the bending stiffness.

Sensor type in the FE model	Tuning in-plane dimensions of GFRP or resin		Slope [N/mm]
Small	l_{G1}, l_{G2}	$\times 1$	960
		$\times (1\text{-}1/3)$	961
		$\times (1\text{+}1/3)$	958
Small	l_{R1}, l_{R2}	$\times 1$	960
		$\times (1\text{-}1/3)$	962
		$\times (1\text{+}1/3)$	958
Large	l_{R1}, l_{R2}	$\times 1$	946
		$\times (1\text{-}1/3)$	949
		$\times (1\text{-}1/2)$	951

126

Table 4.7 The effect of stiffness properties of GFRP and resin on the bending stiffness.

Tuning stiffness properties (E, ν) of GFRP or resin		Slope [N/mm]	
		The FE model with embedded small sensor	The FE model with embedded large sensor
GFRP	$\times\,100\%$	960	946
	$\times\,95\%$	960	945
	$\times\,90\%$	960	945
	$\times\,85\%$	960	945
	$\times\,80\%$	959	945
resin	$\times\,100\%$	960	946
	$\times\,95\%$	960	946
	$\times\,90\%$	960	946
	$\times\,85\%$	960	945
	$\times\,80\%$	960	945

4.5. CONCLUSION

Benefiting from the layered internal structure, the composite material can be self-monitored with a network of embedded sensors. In this research, the flexural stiffness degradation and final failure mechanisms of the CFRP specimens with and without embedded piezoelectric wafer sensors have been investigated experimentally and numerically. The following conclusions are made from the simulations and experiments of four-point bending on different specimens:

- In view of structural stiffness and strength, it seems feasible to embed thin piezoelectric sensors inside composite laminate, and therefore to monitor the response of composite propellers with negligible effect on the global mechanical properties.

- For cross-ply laminates, the fibre tensile failure exhibited a dominant role in the flexural stiffness loss of the composite specimens, which is supported by the load drop observed in the force-displacement curve. Meanwhile the fibre compressive failure, the matrix tensile failure and the matrix compressive failure did not show much contribution in this result.

- The ultimate failure of the composite specimen seemed to be determined by delaminations, which is the consequence of implanting the sensor in the cut-out inside the host-ply. As a result, voids and micro-cracks were introduced during the manufacturing process. In the end of the loading process, the defects propagated quickly and resulted in delaminations. Besides, the position of cut-out and the embedded sensor was shown to have an influence on the propagation and ultimately on the failure load.

- Relatively limited use of the insulation materials (woven GFRP fabric and neat resin) leads to negligible effect on specimen stiffness.

- Delamination was not included in the progressive failure analysis and as a result, the delamination induced final failure was not captured in the numerical simulation. For the future research, cohesive zone modelling could be used to capture delamination and better simulate the flexural failure.

- More experiments should be performed to further support the conclusions of this work.

- It is concluded that the mechanical properties at the hot-spot zone will not deteriorate notably up to 10^6 cycles of fatigue loads. Therefore, it seems safe to use sensors to monitor the propeller performance at certain location. However, further assessment at higher number of fatigue load cycles is required to confirm this expectation.

REFERENCES

[1] Andreades C, Mahmoodi P and Ciampa F. Characterisation of smart CFRP composites with embedded PZT transducers for nonlinear ultrasonic applications. *Composite Structures*. 2018; 206: 456-466.

[2] Seaver M, Trickey ST and Nichols JM. Strain measurements from FBGs embedded in rotating composite propeller blades. In: *Optical Fiber Sensors*, 2006 Oct 23, p. ThD2. Optical Society of America.

[3] Chilles JS, Croxford A and Bond IP. Design of an embedded sensor, for improved structural performance. *Smart Materials and Structures*. 2015; 24(11): 115014.

[4] Carrión JG, Frövel M, Cabrerizo F, et al. Extensive characterisation of the intrusiveness of Fibre Bragg Grating Sensors embedded in a carbon fibre reinforced polymer. In: *Proc. EWSHM08*, Krakow, Poland, 2008, pp.810-817.

[5] Mall S, Dosedel SB and Holl MW. The performance of graphite-epoxy composite with embedded optical fibers under compression. *Smart materials and structures*. 1996; 5(2): 209-215.

[6] Tang HY, Winkelmann C, Lestari W, et al. Composite structural health monitoring through use of embedded PZT sensors. *Journal of Intelligent Material Systems and Structures*. 2011; 22(8): 739-755.

[7] Yang B, Xuan FZ, Jin P, et al. Damage Localization in Composite Laminates by Building in PZT Wafer Transducers: A Comparative Study with Surface-Bonded PZT Strategy. *Advanced Engineering Materials*. 2019; 21(3): 1801040.

[8] Dziendzikowski M, Kurnyta A, Dragan K, et al. In situ Barely Visible Impact Damage detection and localization for composite structures using surface mounted and embedded PZT transducers: A comparative study. *Mechanical Systems and Signal Processing*. 2016; 78:91-106.

[9] Ghasemi-Nejhad MN, Russ R and Pourjalali S. Manufacturing and testing of active composite panels with embedded piezoelectric sensors and actuators. *Journal of Intelligent Material Systems and Structures*. 2005; 16(4): 319-333.

[10] Mall S. Integrity of graphite/epoxy laminate embedded with piezoelectric sensor/actuator under monotonic and fatigue loads. *Smart Materials and Structures*. 2002; 11(4): 527-533.

[11] Mall S and Coleman JM. Monotonic and fatigue loading behavior of quasi-isotropic graphite/epoxy laminate embedded with piezoelectric sensor. *Smart Materials and Structures*. 1998; 7(6): 822-832.

[12] Masmoudi S, El Mahi A and Turki S. Fatigue behaviour and structural health monitoring by acoustic emission of E-glass/epoxy laminates with piezoelectric implant. *Applied Acoustics*. 2016; 100(108): 50-58.

[13] Paget CA and Levin K. Structural integrity of composites with embedded piezoelectric ceramic transducers. In: *Smart Structures and Materials 1999: Smart Structures and Integrated Systems*, 1999 Jun 9, Vol. 3668, pp.306-313. International Society for Optics and Photonics.

[14] Qing XP, Beard SJ, Kumar A, et al. Built-in sensor network for structural health monitoring of composite structure. *Journal of Intelligent Material Systems and Structures*. 2007; 18(1): 39-49.

[15] Schulze R, Streit P, Fischer T, et al. Fiber-reinforced composite structures with embedded piezoelectric sensors. In: *SENSORS, 2014 IEEE*, 2014 Nov 2, pp.1563-1566. IEEE.

[16] Lampani L, Sarasini F, Tirillò J, et al. Analysis of damage in composite laminates with embedded piezoelectric patches subjected to bending action. *Composite Structures*. 2018; 202: 935-942.

[17] Lin M and Chang FK. The manufacture of composite structures with a built-in network of piezoceramics. *Composites Science and Technology*. 2002; 62(7-8): 919-939.

[18] Osmont DL, Dupont M, Gouyon R, et al. Piezoelectric transducer network for dual-mode (active/passive) detection, localization, and evaluation of impact damages in carbon/epoxy composite plates. In: *Fifth European Conference on Smart Structures and Materials*, 2000 Aug 24, Vol. 4073, pp.130-137. International Society for Optics and Photonics.

[19] Sala G, Olivier M, Bettini P, et al. Embedded piezoelectric sensors and actuators for control of active composite structures. In: *6th Cranfield Conference on Dynamics and Control of Systems and Structures in Space*, 2004, pp.437-446. Mechanical and Thermal Engineering Department, Carlo Gavazzi Space ESTEC, European Space Agency.

[20] Liew, CK and Veidt, M. Review of integrated piezoceramic transducers in smart materials and structures. In: Nelson WG *Piezoelectric materials: Structure, properties and applications*. New York, U.S.A.: Nova Science Publishers, 2010, pp.109-132.

[21] Shukla DR and Vizzini AJ. Interlacing for improved performance of laminates with embedded devices. *Smart materials and structures*. 1996; 5(2): 225-229.

[22] Butler S, Gurvich M, Ghoshal A, et al. Effect of embedded sensors on interlaminar damage in composite structures. *Journal of intelligent material systems and structures*. 2011; 22(16): 1857-1868.

[23] Echaabi J, Trochu F and Gauvin R. Review of failure criteria of fibrous composite materials. *Polymer composites*. 1996; 17(6): 786-798.

[24] París F. A Study of Failure Criteria of Fibrous Composite Materials. Report. George Washington University, U.S.A., March 2001.

[25] Davila CG, Camanho PP and Rose CA. Failure criteria for FRP laminates. *Journal of Composite materials*. 2005; 39(4): 323-345.

[26] Icardi U, Locatto S and Longo A. Assessment of Recent Theories for Predicting Failure of Composite Laminates. *Applied Mechanics Reviews*. 2007; 60(2): 76-86.

[27] Rajanish M, Nanjundaradhya NV and Ramesh SS. A Review of Failure of Composite Materials. *International Journal of Enginnering Research and Applications*. 2012; 3: 122-124.

[28] De Luca A adn Caputo F. A review on analytical failure criteria for composite materials. *AIMS Materials Science*. 2017; 4(5): 1165-1185.

[29] Barbero EJ and Shahbazi M. Determination of material properties for ANSYS progressive damage analysis of laminated composites. *Composite Structures*. 2017; 176: 768-779.

[30] Tserpes KI, Papanikos P and Kermanidis TH. A three-dimensional progressive damage model for bolted joints in composite laminates subjected to tensile loading. *Fatigue & Fracture of Engineering Materials & Structures*. 2001; 24(10): 663-675.

[31] Yang J, Peng C, Xiao J, et al. Structural investigation of composite wind turbine blade considering structural collapse in full-scale static tests. *Composite Structures*. 2013; 97: 15-29.

[32] Nahas MN. Survey of failure and post-failure theories of laminated fiber-renforced composites. *Journal of Composites, Technology and Research*. 1986; 8(4): 138-153.

[33] Hahn HT and Tsai SW. On the behavior of composite laminates after initial failures. *Journal of Composite Materials*. 1974; 8(3): 288-305.

[34] Petit PH and Waddoups ME. A method of predicting the nonlinear behavior of laminated composites. *Journal of Composite Materials*. 1969; 3(1): 2-19.

[35] MEGGITT. Data for modelling, https://www.meggittferroperm.com/resources/data-for-modelling/ (2017, accessed 26 December 2020).

[36] Hexcel corporation. HexPly® 8552 Epoxy matrix (180ºC/356º F curing matrix), https://www.hexcel.com/user_area/content_media/raw/HexPly_8552_eu_DataSheet.pdf (2016, accessed 26 December 2020).

[37] ASTM. D6272-17 Standard Test Method for Flexural Properties of Unreinforced and Reinforced Plastics and Electrical Insulating Materials by Four-Point Bending https://compass.astm.org/download/D6272.22166.pdf (2017, accessed 26 December 2020).

[38] ANSYS, Inc. ANSYS Mechanical APDL Element Reference, https://www.mm.bme.hu/~gyebro/files/vem/ansys_14_element_reference.pdf (2011, accessed 26 December 2020).

[39] Andreades C, Mahmoodi P and Ciampa F. Characterisation of smart CFRP composites with embedded PZT transducers for nonlinear ultrasonic applications. *Composite Structures*. 2018; 206: 456-466.

[40] Huntsman. Araldite® LY 5052/Aradur® 5052 COLD CURING EPOXY SYSTEMS, https://samaro.fr/pdf/FT/Araldite_FT_LY_5052_Aradur_5052_EN.pdf (2012, accessed 26 December 2020)

[41] ANSYS, Inc. ANSYS Mechanical APDL Material Reference, https://www.yumpu.com/en/document/read/7801539/mechanical-apdl-material-reference-ansys (2011, accessed 26 December 2020).

[42] Chen, X., Zhao, W., Zhao, X.L. and Xu, J.Z., 2014. Failure test and finite element simulation of a large wind turbine composite blade under static loading. *Energies*, *7*(4), pp.2274-2297.

[43] Nagesh, 2003. Finite-element analysis of composite pressure vessels with progressive degradation. *Defence Science Journal*, *53*(1), pp.75-86.

[44] Gul Apalak, Z., Kemal Apalak, M. and Serdar Genc, M., 2007. Progressive damage modeling of an adhesively bonded composite single lap joint under flexural loads at the mesoscale level. *Journal of reinforced plastics and composites*, *26*(9), pp.903-953.

[45] Tserpes, K.I., Papanikos, P. and Kermanidis, T.H., 2001. A three-dimensional progressive damage model for bolted joints in composite laminates subjected to tensile loading. *Fatigue & Fracture of Engineering Materials & Structures*, *24*(10), pp.663-675.

5

Review

5.1. CONCLUSIONS

In the first part of this research, the short-term fatigue performance of a CFRP marine propeller subjected to non-uniform wakefield was studied. The investigation has been carried out in two steps: finite element analysis of hot-spots of a composite blade model, and experimental investigation on fatigue performance of composite specimens on the basis of the hot-spot analysis. The numerical investigation approach comprised:

- Modelling the composite blade using solid elements, and the boundary condition and 60 load cases for a full revolution.
- Analysing Tsai-Wu failure index for each load case at blade face elements.
- Identifying hot-spot elements according to the attributes of the four largest maximum failure indices at each load case.
- Calculating critical stress and moment resultants for the hot-spot elements.
- Deciding the one most critical hot-spot by comparing the critical resultants of all hot-spots.
- Calculating the stress and moment resultants for the most critical hot-spot at each load case.

The composite specimens and fatigue cyclic loading were designed in view of the lay-up configuration and stress and moment resultants of the most critical hot-spot element. The experimental studies comprised the following steps:

- Making CFRP laminate by hand lay-up method.
- Cutting laminated composite plate into specimens, and evaluating specimens qualities.
- Measuring stiffness properties of the UD CFRP material by experiments.
- Fatigue testing of each 18 non-aged (dry) and aged (wet) specimens. The (residual) tensile stiffness and strength properties were tested for intact specimens and for specimens after undergoing 10^4 and 10^6 cycles of fatigue loads.

The tests using dry specimens suggest that:

- Tensile strength of the dry specimens were not affected by the designed cyclic loading. Because the tensile strength is dominated by fibres, the current fatigue loads have marginal damaging effect on the carbon fibres.
- The tensile failure mode of fibre rupture was observed in the -45° ply, and the matrix cracking existed in the 0 and -90° plies. Besides, the fibre-matrix de-adhesion was observed at crack surfaces.
- The strains calculated from displacements of loading head led to serious underestimations of specimen stiffness, and had to be corrected for the stiffness of the testing machine.
- The equivalent stiffness of intact specimens turned out to be larger than the stiffness predicted by the classical laminate theory. The reason behind it could partly be the underestimated stiffness of testing machine.
- The mean equivalent stiffness of the dry specimens decreased by 17% after applying 10^4 cycles of fatigue loads. Afterwards, the stiffness did not vary notably when the fatigue load cycles increased to 10^6.

The tests using wet specimens suggest that:

- The mass records of specimens immersed in 5% salt water showed classical water uptaking procedure. The specimen mass increased quickly in the beginning, and reached a plateau, i.e., saturation state, after 60 days.

- Tensile strength of the wet specimens were not affected by the designed cyclic loading. Compared to corresponding (residual) strength of the dry specimens, the difference was very limited. Therefore, the aging procedure had little effect on the carbon fibres.

- The same tensile failure modes were observed in the wet specimens as in the dry specimens.

- The extensometer was used in each stiffness test of wet specimens. The calculation results of equivalent stiffness of intact wet specimens turned out to be close to the stiffness predicted by the classical laminate theory. Therefore, the extensometer worked well in measuring strain at the gauge area.

- The mean equivalent tensile stiffness of wet specimens did not decline notably after applying 10^4 cycles of fatigue loads, but decreased by 7% when the fatigue load cycles increased to 10^6.

- During fatigue tests, the mass loss resulted from moisture evaporation accounted for approximately half of the mass gain by water uptaking. Therefore, a new method for maintaining wet specimens is required in the future research.

In the second part of this research, the influence of embedding piezoelectric sensors on the flexural behaviour of CFRP specimens was studied. Four types of specimens were used in the research: the benchmark specimens without embedded sensor, the specimens with embedded small sensor at tension or compression side, and the specimens with embedded large sensor at compression side. The progressive failure analysis was performed with finite element model of each specimen. The simulation outputs of load-displacement relation were compared with corresponding test records. The comparisons suggest that:

- The fibre tensile failure determined the degradation of flexural stiffness, while the influence of fibre compressive failure, and the matrix tensile and compressive failures was marginal.

- The ultimate failure was dominated by delamination, which have been observed in the four-point bending tests. Voids and micro cracks were introduced by embedding sensors. The defects propagated during loading process, and eventually destroyed the specimen integrity. Because of the perfect bonding assumption, however, the delamination was not simulated. Therefore, the ultimate failure was not captured in the present models.

- The effects of insulation materials (GFRP material and resin) around the sensors were studied. Possibly due to the limited volume of insulation materials used, the variation of dimensions and stiffness properties of insulation materials did not notably affect the global flexural stiffness.

- Because the performance at the hot-spot zone will not deteriorate up to 10^6 cycles of fatigue loads, within this specific lifetime, it seems safe and feasible to use thin piezoelectric sensors inside composite laminate to monitor the propeller properties at certain location. Meanwhile, it still requires further assessment at higher number of fatigue load cycles to validate this expectation.

5.2. RECOMMENDATIONS FOR FUTURE WORK

The prospects of applying composite marine propellers show multiple benefits, which have motivated a series of research including the one presented in this dissertation. This research aimed to expand the understandings on the mechanical behaviour of composite marine propellers. Next to the presented conclusions, the following recommendations are proposed for future work:

- Studying development of the tensile stiffness and strength properties of the CFRP specimens subjected to higher fatigue cycles. In current research the specimens were tested with the maximum of 10^6 cycles of fatigue loads. The effect of increasing fatigue loads on residual stiffness and strength properties should be investigated experimentally.

- Designing new setup for fatigue tests. The current method of wrapping aged specimens with wet papers and plastic foils did not work desirably in maintaining the absorbed water during fatigue tests. A new setup should be designed where the specimens are immersed in salt water and subjected to fatigue loads simultaneously. The fatigue loads would create defects inside specimens, meanwhile more water molecules could be absorbed.

- Investigating fatigue performance of the other hot-spots. The hot-spots which have compressive stress states should be concerned. Because the compressive cyclic loading is then designed for the corresponding specimens, and the specimens are susceptible to compressive loads, it can be anticipated that the compressive stiffness and strength properties would decrease by larger extents.

- Studying other loading conditions. In current research the CFRP propeller is considered to work in a non-uniform wakefield, which generated from the straight path sailing of the considered vessel in calm water at constant speed of 10.4 knots. The other manoeuvres and sailing conditions would result in more complex loads that can influence the fatigue lifetime of the composite propeller.

- Performing full-scale tests. The current experimental investigations have shown that the tensile stiffness of wet specimens decreased by 7% after applying 10^6 cycles fatigue loads, which would affect the structural response of the composite blade. Adapted structural response would inversely affect the stress states and ultimately the fatigue performance of the hot-spots. This synergistic effect should be investigated in full-scale tests.

- Optimising lay-up configuration of the face laminates for extending fatigue lifetime. The properties could be improved by optimising the stacking sequence of CFRP laminates.

- Improving modelling and progressive failure analysis methods. Other post-failure theories, e.g., gradual degradation of stiffness, could be applied for progressive failure analysis, and compared with experimental results. Besides, delaminations should be included in the model to capture the ultimate failure.

- Introducing more variables to study the influence of embedding sensor on the mechanical properties of composite laminates. Different solutions of implanting sensor into the laminates should also be investigated and compared. More static and fatigue tests should be performed. Composite laminates with embedded sensors should also be tested in water environment to investigate the combined effects of water uptaking and sensor embedding.

6

Acknowledgements

"The credit belongs to the man who is actually in the arena, whose face is marred by dust and sweat and blood; who strives valiantly; who errs, who comes short again and again, because there is no effort without error and shortcoming; but who does actually strive to do the deeds; who knows great enthusiasms, the great devotions; who spends himself in a worthy cause; who at the best knows in the end the triumph of high achievement, and who at the worst, if he fails, at least fails while daring greatly".

Theodore Roosevelt

After five years of working, it finally brings to the closure of my doctoral research. Looking backward, it was a tough experience, more challenging (or dreadful) than I have anticipated before it started. It is not shameful to admit that I cried many times during the past years, much more than I have ever done for the failures in love. With my greatest appreciations, I hereby list the names of the persons who have pulled me out of muds.

First I would like to thank Menno van der Horst who has encouraged me to apply for the doctoral position at the team of Ship and Offshore Structures. It is the very beginning of all stories. I thank my promoter Professor Mirek Kaminski very much for approving my application. Thereafter I have chance to join this great team and meet new colleagues and friends. My special thanks to Henk den Besten who has supervised my research in the first two years. Your critical mind promoted the transition of my role from a student to a researcher.

As explained in the earlier chapters, my research has been carried out both numerically and experimentally. I have received important help from Pieter Maljaars in modelling the composite marine propeller blade. It laid down the foundation for analysing the fatigue performance of composite propeller. I met Arno Huijer when he just started the master thesis project. It is a great pleasure to witness your success at graduation, and work together afterwards when you continued as a doctoral candidate as well. Thank you very much for helping me to make the experimental specimens, cooperating at tests, and all discussions/chats in and after work. Also I am thankful to Victor Horbowiec, Dave Ruijtenbeek and Durga Mainali working at Delft Aerospace Structures and Materials Laboratory. The tests would not be performed successfully and efficiently without your supports in manufacturing specimens, scheduling experiment and setting up test machines, and aging specimens. I get to know Marco ten Eikelder since the first day I came to our office. During the whole time I have received consistent encouragement and sometimes even push from you. I appreciate all your support, and I am impressed by your progresses achieved from your doctoral research.

The names of my supervisors, Pooria Pahlavan and Professor Christos Kassapoglou, come late, because it is really beyond my language capability to express my gratitude to you. I cannot imagine what would happen without your supports, and I am already scared by thinking of that. But not graduating before the postponed deadline for sure. Honestly, Pooria, I would not have gone forward without your trust. You have saved me from the rock bottom, and inspired me with your enthusiasm, initiative and creativity at work. Because of your sincere personality and open mind, I was free to express myself at ups and particularly at downs. My greatest respect to Christos for your patience, guidance, suggestions and feedbacks. Benefited from your broad and profound knowledge of composite

materials and structures, I have learnt new EVERY time from our meeting. You see both the forest and trees, and even leaves. You remind me of an intellectual giant in the ancient history of your motherland, Aristotle. One of the important lessons I have learnt from you is that, as a science researcher, being critical with number and making a statement based on solid support of number.

I have always enjoyed the time of coffee and tea breaks and lunches with my colleagues and some master students at the group of Ship Hydromechanics and Structures. Though I did not join much due to my pressure and depression.

I have also enjoyed some personal contacts after work. Marco, thank you very much for inviting me for dinners in working days and weekends (and paid the food for many times). I had a lot of happy time because of our easy chatting. Hugo, thank you very much for introducing Utrecht when I moved and started a new life here, walking around in the ancient city centre and enjoying coffee and ice cream is a great experience. Our gentlemen's discussion over politics broadens my view, and what helps us to better understand each other is not what we agree on but what we disagree about. I thank Niles for the beers, alcohols, and music we enjoyed together, and cheers to the drinking games and our houseplants. My special thanks to Mamy and Tanja and your children Zavy and Nori. I am honoured to be invited to visit your family, and I have enjoyed the time of chats and dinners. Being friends with any one of you is an honour and privilege, I could not believe that I even possess that much luck to know you all.

In the end I would like to express my gratitude to my family. Like any other lucky persons, I have been growing up in a family which has a lot of love. My parents did not go to a university, but they understand the importance of education. Though they do not have much money, my parents and grandparents have done all their bests to support me to fulfill dreams. My sister Xiaolan and brother-in-law Leilei and my adorable nephew, and my brother Xiaofeng have also supported me in their own way. In China's culture we are not used to expressing affections for family, be that as it may, love is my word to you all.

Curriculum Vitae

EDUCATION BACKGROUND

2016-2020 PhD Candidate
Delft University of Technology, Delft, The Netherlands

2010-2012 MSc in Mechanical Engineering
Program: Engineering Mechanics (Solid Mechanics track)
Kungliga Tekniska högskolan, Stockholm, Sweden

2006-2010 BSc in Engineering Mechanics
Wuhan University, Wuhan, China

WORKING EXPERIENCE

2020-now Civil/Structural Engineer
R&G Engineering B.V., Culemborg, The Netherlands

2012-2014 Structural Engineer
WISDRI Engineering & Research Incorporation Limited, Shanghai, China

LIST OF PUBLICATIONS

Zhang, X., Kassapoglou, C., Maljaars, P.J., Kaminski, M.L. and Pahlavan, L., 2021. Stiffness and strength reduction in early fatigue stages of composite marine propellers. Manuscript under review.

Zhang, X., Huijer, A., Kassapoglou, C. and Pahlavan, L., 2021. Mechanical Behaviour of composite laminates embedded with PZT wafer sensors. Manuscript under review.

Huijer, A., Zhang, X., Kassapoglou, C. and Pahlavan, L., 2021. Feasibility Evaluation for Development of Self-monitoring Composite Propellers. Conditionally accepted, manuscript under revision.